MAX-PLANCK-INSTITUT
FÜR METEOROLOGIE

IMPRS-ESM

International Max Planck Research School on Earth System Modelling

A different view on the AMOC and the timing of climate change

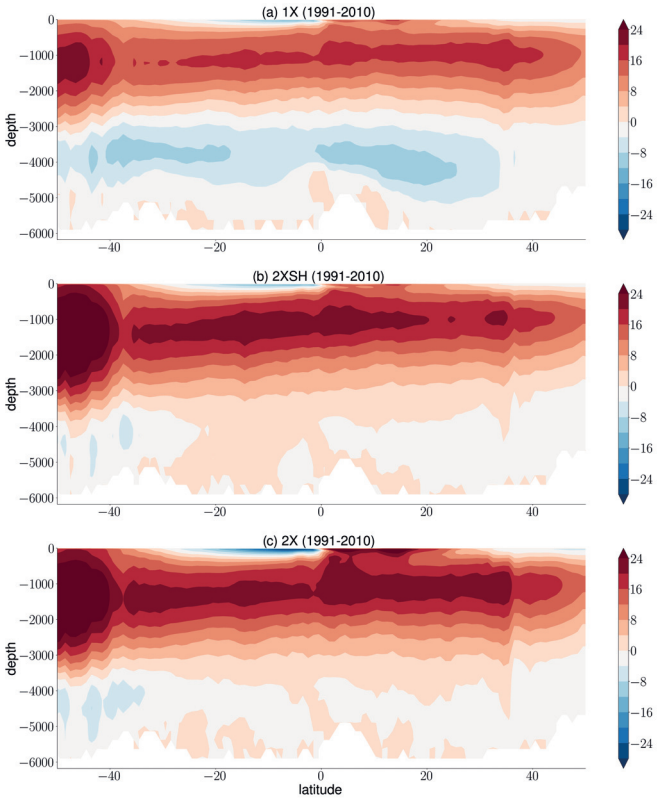

Tim Rohrschneider

Hamburg 2022

Berichte zur Erdsystemforschung
Reports on Earth System Science

255
2022

Hinweis

Die Berichte zur Erdsystemforschung werden vom Max-Planck-Institut für Meteorologie in Hamburg in unregelmäßiger Abfolge herausgegeben.

Sie enthalten wissenschaftliche und technische Beiträge, inklusive Dissertationen.

Die Beiträge geben nicht notwendigerweise die Auffassung des Instituts wieder.

Die "Berichte zur Erdsystemforschung" führen die vorherigen Reihen "Reports" und "Examensarbeiten" weiter.

Anschrift / Address

Max-Planck-Institut für Meteorologie
Bundesstrasse 53
20146 Hamburg
Deutschland

Tel./Phone: +49 (0)40 4 11 73 - 0
Fax: +49 (0)40 4 11 73 - 298

name.surname@mpimet.mpg.de
www.mpimet.mpg.de

Notice

The Reports on Earth System Science are published by the Max Planck Institute for Meteorology in Hamburg. They appear in irregular intervals.

They contain scientific and technical contributions, including Ph. D. theses.

The Reports do not necessarily reflect the opinion of the Institute.

The "Reports on Earth System Science" continue the former "Reports" and "Examensarbeiten" of the Max Planck Institute.

Layout

Bettina Diallo and Norbert P. Noreiks
Communication

Copyright

A different view on the AMOC and the timing of climate change

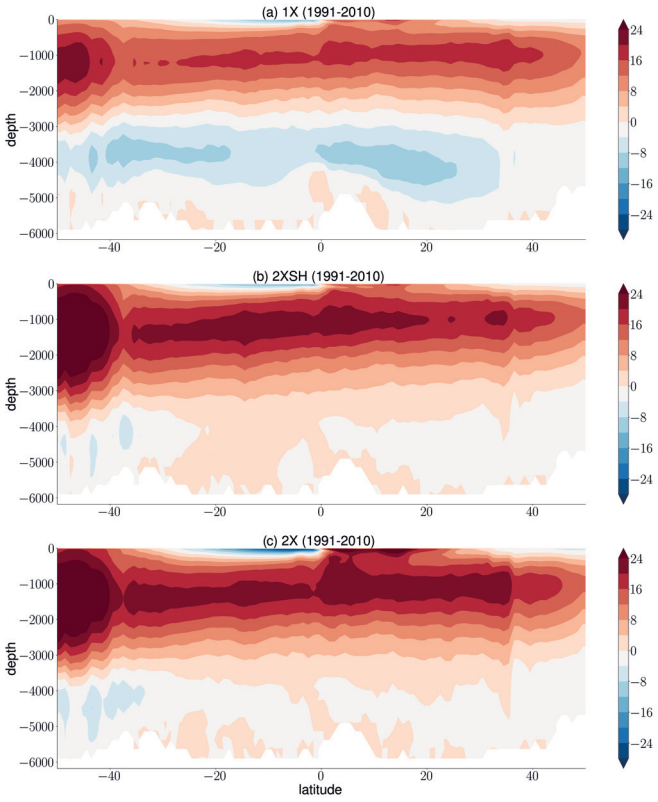

Tim Rohrschneider

Hamburg 2022

Tim Rohrschneider

Max-Planck-Institut für Meteorologie
The International Max Planck Research School on Earth System Modelling
(IMPRS-ESM)
Bundesstrasse 53
20146 Hamburg

Universität Hamburg
Geowissenschaften
Institut fuer Meereskunde
Bundesstr. 55
20146 Hamburg

Tag der Disputation: 12. Juli 2022

Folgende Gutachter empfehlen die Annahme der Dissertation:
Prof. Johanna Baehr
Prof. Jochem Marotzke

Vorsitzender des Promotionsausschusses:
Prof. Dr. Hermann Held

Dekan der MIN-Fakultät:
Prof. Dr. Heinrich Graener

ISSN 1614-1199 - doi:10.17617/2.3396792

Thesis Summary

From an overarching perspective, in this thesis I analyze the particular role of Ekman pumping and the Atlantic circumpolar current (ACC) for ocean and climate dynamics. It is about the wind sensitivity of the Atlantic Meridional Overturning Circulation (AMOC) considering ocean dynamics as well as the temporal adjustment of the climate response to forcing on a centennial timescale considering climate dynamics. I find that the AMOC depends on local northern hemisphere Ekman pumping besides nonlocal Southern hemisphere Ekman pumping. Ekman pumping is associated with the rotation of the surface wind stress vector. The changes in overturning are reflected by the level of no motion which is the depth of maximum overturning. Wind-driven Ekman compensation is baroclinic and occurs above the level of no motion, and the internal vertical velocity shear that is not influenced by the external Ekman cells stays approximately constant. Focusing on a second paper, Ekman pumping and the ACC as well as the AMOC force ocean heat uptake and its redistribution. That is, they influence the climate dynamics of the Earth system. In this connection, the amplitude and timing of the surface air temperature adjustment on a centennial timescale depends on the ocean component. I question whether long-term climate change is described by a single e-folding mode with a constant timescale which is commonly assumed to be independent of temperature or forcing and the evolution of time. I find that feedback temperature dependence strongly influences the equilibrium temperature response and adjustment timescale of the slow mode which describes long-term climate change. However, the timescale is additionally influenced by the thermal inertia of the ocean in the sense that the latter is inconstant from a global perspective. There is timescale pattern that depends on dynamic components such as Ekman pumping and the AMOC, and the ocean circulation can change over time.

Zusammenfassung

In dieser Dissertation analysiere ich übergreifend die wichtige Rolle des vertikalen Ekman-Transports (Ekman pumping) und des Antarktischen Zirkumpolarstrom für die Ozeandynamik und Klimadynamik. Die Dissertation handelt von der Windsensitivität der Atlantischen Meridionalen Umwälzbewegung in Bezug auf die Ozeandynamik und von der zeitlichen Anpassung der Klimareaktion zu verändertem Klimaantrieb auf hundertjähriger Zeitskala in Bezug auf die Klimadynamik. Es zeigt sich, dass die Atlantische Meridionale Umwälzbewegung von lokalen Winden in der nördlichen Hemisphäre abhängt, neben nonlokalen Windeffekten die vom Südlichen Ozean ausgehen. Spezifischer, die Atlantische Meridionale Umwälzbewegung hängt von lokalen und nonlokalen vertikalen Ekman-Transport ab, der von der Rotation des Windvektors berechnet wird. Die windabhängigen Änderungen in der Umwälzbewegung spiegeln sich in der Tiefe der stärksten Umwälzbewegung wider. Die windgetriebene Ekmankompensation is baroklin and findet über der Tiefe der stärksten Umwälzbewegung statt. Die interne vertikale Scherung der Geschwindigkeit, die nicht von den Ekmanzellen beeinflusst wird, bleibt trotz veränderten Windantrieb konstant. Die zweite Publikation einleitend, der vertikale Ekman-Transport und der Antarktische Zirkumpolarstrom sowie die Atlantische Meridionale Umwälzbewegung forcieren die ozeanische Wärmeaufnahme und deren geographische Verteilung. Dementsprechend beeinflussen sie die Klimadynamik des Erdsystems. In dieser Verbindung hängt die Amplitude und zeitliche Anpassung der Oberflächenlufttemperatur des Erdsystems auf hundertjähriger Zeitskala vom Ozean ab. Ich hinterfrage ob der langzeitige Klimawandel durch eine einzelne e-folding Mode mit einer konstanten Zeitskala abhängt. Diese Zeitskala wird üblicher Weise als unabhängig von Temperatur und Zeit angesehen. Es zeigt sich, dass die Temperaturabhängigkeit der Klimarückkopplung sehr stark die neue Gleichgewichtstemperatur und die zeitliche Anpassung der langsamen Mode beeinflusst, die den langzeitigen Klimawandel beschreibt. Jedoch hängt die Zeitskala zusätzlich von der thermischen Trägheit des Ozeans ab, die inkonstant ist von einer globalen Perspektive. Es gibt eine geographische Zeitskalen-

verteilung, die von dynamischen Komponenten wie dem vertikalen Ekman-Transport und der Atlantischen Meridionalen Umwälzbewegung abhängt, und die Ozeanzirkulation kann sich mit der Zeit verändern.

Acknowledgement

This work was funded by the Max Planck Society (MPG) and the International Max Planck Research School on Earth System Modelling (IMPRS ESM). I further thank Deutsches Klima Rechenzentrum (DKRZ) for providing the computational resources.

.....

Author's signature

Contents

Chapter 1

General introduction and overview

This chapter of the thesis is an overarching introduction to the first and second paper of the cumulative dissertation. I give the inexperienced reader the resource to understand this dissertation and embed it scientifically.

1.1 Approach

The present dissertation is based on Earth System science. I make use of numerical modeling approaches to analyze the underlying ocean dynamics and climate dynamics of the Earth system. More precisely, the first paper of the dissertation is about ocean dynamics and the second paper is about climate dynamics. Ocean dynamics as a field studies the oceanic physical motions without considering geobiochemical processes. Climate dynamics as a field is more broadly defined and studies the evolution of the Earth's climate and the processes that control Earth's climate. Numerical ocean and atmosphere models are used to analyze the ocean dynamics and climate dynamics of the Earth system. Their common name is general circulation model (GCM), and physical ocean general circulation models (OGCMs) and atmosphere general circulation models (AGCMs) of the planetary ocean and atmosphere are based on the Navier-Stokes equation on a rotating sphere.

Thermodynamic terms are included to simulate energy sources and fluxes such as radiation and latent heat. In technical terms, the prognostic equations of these models are discretized and integrated forward in time. That is to say, these models depend on initial conditions as well as boundary conditions, which set up the numerical domain. Comprehensive Earth System models (ESMs) additionally include geobiochemical processes to e.g. simulate the carbon cycle. Different components such as OGCMs and AGCMs and dynamic vegetation models form ESMs. I focus on the physical processes of the ocean and atmosphere only. I use the outcome of a high resolution OGCM to analyze the underlying ocean dynamics in terms of the Atlantic meridional overturning circulation (AMOC) in a first paper, and I use the outcome of multiple low-resolution coupled atmosphere-ocean general circulation models (AOGCMs) as ESM components to analyze the underlying climate dynamics of the Earth system in terms of the temperature response in a second paper. The climate of the Earth system is strongly influenced by Earth's ocean and surface wind, which forms the overarching topic of this dissertation. In the first paper I analyze the wind forcing dependence of the AMOC. It is well known and accepted that the redistribution of heat by the AMOC is important for Earth's climate, and changes in the strength of the AMOC cause climate changes. In the second paper I analyze the temperature evolution in response to CO_2 forcing and focus on the temperature adjustment on a centennial timescale, which is about thermal inertia. With these two papers and subsequent discussions I implicitly demonstrate the particular role of Ekman pumping and the Antarctic circumpolar current (ACC) for Earth's ocean and climate. They strongly influence Earth's ocean and climate dynamics.

Ekman pumping is the oceanic vertical motion directly caused by the wind stress at the surface of the ocean. It is computed by the rotation of the surface wind stress vector. Ekman pumping W_E is thus given by $W_\mathrm{E} = \nabla \times \tau/(f\rho_0)$ where τ is the surface wind stress, f is the Coriolis parameter, and ρ_0 is the reference density under Boussinesq approximation as done in many OGCMs. It is well known that Ekman pumping is strongest in the Southern Ocean

north of the ACC and in the subtropical gyres of the different basins. The ACC is a wind-driven, eddy-rich current that is associated with the zonal periodicity of the flow at the latitudes of the Drake passage. It is connected to the southern hemisphere meridional Ekman cell and the global meridional overturning circulation. Ekman transport is the transport directly forced by the surface wind and perpendicular to the wind stress vector. However, it is independent of the rotation of the surface wind stress vector in the sense that Ekman pumping does not necessarily influence Ekman transport or the Ekman cells. The ACC is related with strong Ekman pumping north of it in the Southern Ocean due to the strong rotation in the surface wind stress field. Synthesizing, the ACC influences the inter-hemispheric AMOC remotely. In general, the Southern Ocean absorbs the major part of the heat excess by recent global warming. In turn, the major part of ocean heat uptake in the Southern Ocean is transported by the meridional Ekman flux and the AMOC.

As we learn during the course of the dissertation, the forcing imposed by the wind stress curl at the surface strongly influences the AMOC, which is shown in the first paper. Furthermore, ocean heat uptake forced by Ekman pumping and the ACC, and redistributed by the ocean circulation, also modify Earth's surface temperature adjustment in the sense that the surface air temperature adjustment is prolonged or shortened. The second paper of the dissertation considers the slow surface air temperature adjustment on a centennial timescale which is strongly influenced by the degree to which the ocean takes up heat.

1.2 First paper under Ocean dynamics

As physical atmosphere dynamics, ocean dynamics are governed by the Navier-Stokes equations. These equations are fundamental for any physical modeling approach using complex models and given by the zonal, meridional and vertical momentum equations, the continuity equation, and thermodynamic equations for the change in temperature and salinity. They form the basis of an OGCM, which in turn forms the basis of the first paper of the dissertation.

In fact, ocean dynamics is a vast field with many different applications such as observational arrays, simplified models, and general circulation models of the planetary ocean. Major research areas are ocean circulation and currents, convection, turbulence and diffusion, waves and OGCM development itself. The methodologies depend on the applications at hand, and epistemic values may differ between these applications. The study of ocean dynamics commonly understands the ocean as a complex oceanic dynamic system. For instance, dynamic variations in the motion and temperature and salinity field of the ocean give rise to dynamic layers such as the surface mixed layer, the thermocline or pycnocline, and the deep ocean. In the first paper I focus on the dynamics in the mixed layer and the thermocline or pycnocline. The forcing imposed by the surface wind drives Ekman transport, Ekman pumping, and Ekman suction in the upper part of the ocean, which in turn may influence the geostrophic meridional transport at greater depths. Different components of the ocean circulation are themselves systems such as the AMOC under which different components interact. In this introduction I briefly focus on the use of OGCMs as well as the simulation of the AMOC in terms of major challenges.

In essence, the AMOC (e.g. Kuhlbrodt et al., 2007; Marshall and Speer, 2012; Johnson et al., 2019) describes the net northward meridional flow of thermocline or pycnocline waters and intermediate waters through the Atlantic basin. The flow in the upper kilometer of the Atlantic basin is compensated by a net southward flow of North Atlantic deep water formation (NADW) waters below the thermocline or pycnocline. Considering NADW, water sinks locally because of significant buoyancy loss. The transformation of the waters from the lower levels to the upper levels occurs partially due to wind driven diapycnal mixing and tidally-driven diapycnal mixing. Additionally, adiabatic wind-driven upwelling takes place in the mixed layer of the Southern Ocean. There was the belief that the AMOC is driven entirely by thermohaline forcing. Nowadays it is widely accepted that the AMOC is at least in part adiabatic in the sense that the flow follows isopycnals which are set by the wind forcing over the Southern Ocean. These isopycnals span

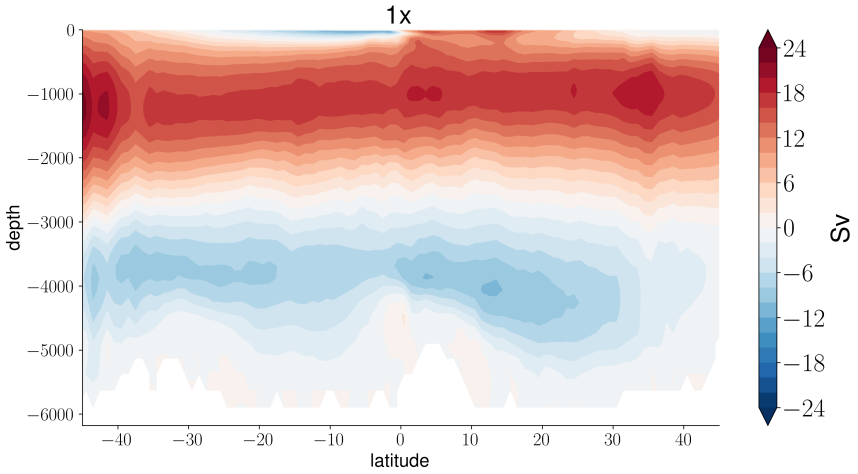

Figure 1.1: The time-mean (1991-2010) AMOC in the high-resolution OGCM which is called MPIOM TP6ML80 and used in the first study of the dissertation. The experiment mimics observed conditions. The OGCM is forced by NCEP reanalysis (Kalnay et al., 2018). The meridional velocity v is integrated zonally and cumulatively vertically.

the Atlantic basin meridionally. Below the upper cell of the AMOC which rotates clockwise, there is a lower cell which rotates anti-clockwise. Fig. 1.1 shows the Atlantic overturning streamfunctions in an experiment which mimics observed conditions, using the high-resolution OGCM which I did make use of in the first study. I focus on the upper cell only and thus on the Ekman cells and the geostrophic transport in the thermocline or pycnocline. More precisely, I analyze the vertical range from the surface to the depth of maximum overturning to investigate the wind forcing dependence that reflects the quasi-steady response of the AMOC to wind forcing. Major research questions developed during the last two decades which are well summarized in Johnson et al. (2019). As major research areas I identify the generation and propagation of AMOC variability, the role of extrinsic and intrinsic AMOC variability, the role of multiple basins, AMOC stability, Southern hemisphere processes, and the AMOC response to different forcings in order to obtain base solutions. It is still important to investigate the role of external forcing such as the influence of the surface winds on the AMOC

despite a wide range of modeling studies on Southern Ocean winds. Research is lacking in so far that the explicit role of Ekman pumping for the AMOC in the southern hemisphere as well as in the northern hemisphere has not been addressed hitherto. It is the subject of the first paper, which is thus a fundamental contribution to the base solutions of the AMOC.

At the same time, the AMOC research in this dissertation is conducted with a high-resolution OGCM to better simulate the ocean dynamics. In general, the important role of the ocean for Earth's heat uptake makes it necessary to accurately represent and reproduce the physical ocean processes and circulation systems such as the AMOC. Currently, the sensitivity of ocean heat uptake as well as the AMOC to the representation of mesoscale eddies is investigated by the scientific community (Fox-Kemper et al., 2019). Besides, the Southern Ocean plays a major role for ocean heat uptake and the AMOC, such that it has become a major research area for OGCM development during the last two decades. For instance, Ito and Marshall (2008) and Bishop et al. (2016) combine these research areas and analyze mesoscale eddy effects in terms of southern hemisphere processes. In general, the resolution or parameterization of mesoscale eddies to better simulate the ocean dynamics gives rise to a large body of literature of contemporary ocean dynamics. The representation of the AMOC reveals intermodel spread among OGCMs under CMIP6 (O'Neill et al., 2016) (not shown), and there is spread among OGCMs at different resolutions which have been recently developed at Max Planck Institute for Meteorology (not shown). It is widely accepted that mesoscale eddies affect meridional heat transport, ocean heat uptake and systems such as the AMOC. The Southern Ocean Meridional Overturning Circulation, for instance, depends on the treatment of eddy effects. In a wide range of OGCMs, eddy-induced advection and eddy-induced diffusion are parameterized. There exists a wide range of literature on the Gent and McWilliams parameterization (Gent et al., 1995). There exists also a wide range of literature on anisotropic diffusion introduced by Redi (1982). The high-resolution OGCM that I use switches off the Gent and McWilliams parameterization.

1.2.1 Driving processes of the AMOC

In the first paper I focus on the upper branch of the AMOC (e.g. Kuhlbrodt et al., 2007; Marshall and Speer, 2012; Johnson et al., 2019) which is the clockwise rotating overturning cell. It connects Southern Ocean Ekman transport which is the transport directly forced by the surface winds and North Atlantic deep water formation (NAWD) which arises from the buoyancy loss of the thermocline and intermediate waters at the northern margin of the basin. The inter-hemispheric northward flow of the AMOC occurs in the upper kilometer of the Atlantic ocean. In this connection, in the first paper I consider the wind forcing dependence of the AMOC in relation to large-scale wind patterns.

The AMOC was thought to be driven only by diapycnal mixing in the ocean interior that lightens deep water masses which subsequently upwell in the tropics. This dates back to Sandstroem's theorem (1916) from which the traditional view on the thermohaline circulation emerged: the NADW cell forms deep water at the northern margin of the basin which subsequently upwells at lower latitudes due to turbulent mixing. Internal gravity waves, generated by winds and tides, dissipate into small-scale motion which lead to turbulence (Munk and Wunsch, 1998). That is to say, the downward heat flux in the tropics is responsible for closing the meridional overturning circulation in the sense that the AMOC is fed by the conversion of dense waters to light waters which subsequently are reconverted to dense waters. In general, the rise of the potential energy of the deep water masses is sustained by small-scale mechanical energy input according to this branch of literature. Considering the regime of the thermohaline circulation, Marotzke (1997) analyzes the influence of the location of mixing and find that boundary mixing at the eastern and western margins drives meridional flow due to the thermal wind relation. The thermal wind relation equivalates zonal density gradients with the vertical velocity shear of the meridional velocity due to hydrostatic and geostrophic balance. The velocity shear is then integrated vertically in order to compute the meridional transport. Also referring to thermohaline

forcing, Marotzke and Klinger (2000) establish a theory for inter-hemispheric overturning that is solely based on how boundary densities unfold vertically.

However, large-scale energy input by winds as a primary driving force has become a major focus in the recent literature on the AMOC. It is found that increasing the wind stress over the Southern Ocean strengthens the NADW cell substantially. Since Toggweiler and Samuels (1995) this is mostly known as Drake passage effect which is associated with the Antarctic circumpolar current (ACC). The ACC makes it impossible to maintain a zonal pressure gradient due to the absence of continental boundaries, which in turn inhibits meridional geostrophic flow. There is no net geostrophic flow that counterbalances the northward surface Ekman flux which connects the Southern Ocean upwelling and NADW (e.g. Marshall and Speer, 2012). The strengthening of the NADW cell due to an increase in Southern Ocean wind stress has been confirmed by some numerical experiments with numerical ocean models (e.g. Klinger et al., 2003, 2004; Klinger and Cruz, 2009; Lüschow et al., 2021). Moreover, the forcing imposed by the wind stress curl over the Southern Ocean is thought to change density stratification throughout the Atlantic basin (e.g. Vallis, 2000; Allison et al., 2011; Nikurashin and Vallis, 2012), which in turn changes the force balance of the flow and may set the depth scales of the AMOC remotely. Commonly ignored are large-scale wind patterns away from the Southern Ocean. In the first paper I analyze the wind forcing dependence of the AMOC by incorporating the influence of northern hemisphere winds. These northern hemisphere winds were not thought to influence the AMOC in a substantial way.

1.2.2 Gnanadesikan's box model

First and foremost, Gnanadesikan (1999) included Southern Ocean wind stress as a forcing mechanism that deepens the pycnocline scale throughout the basin, which is related to stronger overturning. The pycnocline scale is a depth scale and a measure for vertical density stratification. It describes how density unfolds vertically. It is commonly used as vertical depth scale

to scale the geostrophic transport of the AMOC, since thermal wind balance provides a link between zonal pressure gradients and density stratification. Gnanadesikan (1999) proposed a simple box model in which the pycnocline scale is determined, which in turn scales the northward transport of the AMOC.

In general, there exist a hierachy of AMOC models, which ranges from simple box models to complex ocean general circulation models (OGCMs). Simple models provide useful scaling relationships to provide conceptual understanding and interpret the more complicated models as well as to analyze system properties and estimate the overturning strength. In the literature on the AMOC, the most popular box models are Stommel's (1961) box model on the stability of the thermohaline circulation and Gnanadesikan's (1999) box model itself. From an overarching perspective, these two box models represent the two paradigms of AMOC research. The former model is about buoyancy-forced dynamics with tropical upwelling or deep convection at northern high latitudes as driver of the AMOC. The latter model is about mechanical energy input to maintain northward overturning in the Atlantic, with Southern Ocean processes as a closure for the meridional circulation.

Inherently, Gnanadesikan's (1999) box model is about depth scaling that scales the overturning strength. In order to scale the strength of the AMOC, it uses theory on the global pycnocline which separates low-latitude surface waters and dense abyssal waters. The time-dependent form of the pycnocline model is given by

$$A\frac{\partial \eta}{\partial t} = \psi_{\mathrm{Ek}} - \psi_{\mathrm{Eddy}} + \psi_{\mathrm{U}} - \psi_{\mathrm{N}}, \tag{1.1}$$

with A the upwelling area and η the pycnocline scale (e.g. Johnson et al., 2007; Marshall and Zaana, 2014). The pycnocline scale is determined by the northward Ekman flux ψ_{Ek} in the Southern Ocean, the volume flux associated with mesoscale eddies in the Southern ocean ψ_{Eddy}, diapycnal upwelling in the interior ψ_{U}, and northern hemisphere sinking ψ_{N}. The strength of northward overturning is given by ψ_{N} which is the horizontally and verti-

cally integrated northward geostrophic transport above the pycnocline. This scaling is given by $\psi_{\mathrm{N}} = Cg'\eta^2/(\beta L_y^{\mathrm{N}})$ where C is a parameter for effects of geometry and boundary layer structure, g' is the reduced gravity with respect to meridional density gradients, β is the north-south gradient in the Coriolis parameter, and L_y^{N} is the north-south distance of the density gradient. It combines the assumption that the large-scale dynamics are in geostrophic balance using the thermal wind relation and classical boundary layer theory on frictional boundary layers. I would describe Gnanadesikan's (1999) pycnocline model as forcing-response framework, since it relates the pycnocline scale which is proportional to northward transport to positive and negative forcing mechanisms.

Gnanadesikan's (1999) model does account for the large-scale wind patterns over the Southern Ocean but does not account for large-scale wind patterns in the northern hemisphere. Furthermore, a recent study by DeBoer et al. (2010) suggests that the scaling in Gnanadesikan's (1999) model is only appropriate if the level of no motion is used rather than the pycnocline scale. The level of no motion is the depth of maximum overturning. I make use of this research gap and analyze the wind forcing dependence of the AMOC by understanding its depth scales; that is, I analyze both the pycnocline scale and the level of no motion. It is an experimental study because we use OGCM experiments rather than conceptual models.

1.2.3 AMOC decomposition

An outcome of my experimental study is that northward overturning is well approximated by the level of no motion which reflects the wind forcing dependence of the AMOC. I demonstrate that using the level of no motion, the flow can be subdivided into internal flow and external flow, because the external baroclinic Ekman cells that are directly forced by the surface winds cancel out by vertical integration.

In general, AMOC decomposition is key for our understanding on relative contributions of different processes as well as key for observational arrays to measure the strength of the AMOC. Observational arrays depend on the mathematical way how we decompose the AMOC, since they are based on different components such as the thermal wind relation to compute e.g. the geostrophic shear component (e.g. Baehr et al., 2004; Cunningham et al., 2007; Baehr et al., 2009; Frajka-Williams et al., 2019). Needless to say, our understanding on the force balance of the flow influences the way how we decompose the AMOC formally. For instance, dynamical AMOC decomposition as done by Hirschi and Marotzke (2007) or Moreno-Chamarro et al. (2016) depends on whether we assume a barotropic or baroclinic return flow of the surface Ekman flux. Commonly, the interior return flow of the surface Ekman flux is assumed to be barotropic, which is a wrong assumption on timescales longer than seasonal timescales as outlined in my thesis. Hirschi and Marotzke (2007) and Moreno-Chamarro et al. (2016) propose to decompose the AMOC into three components which are the Ekman transport ψ_{Ek}, the geostrophic shear component ψ_{sh}, and the external or barotropic mode ψ_{ex}. The horizontally and cumulatively vertically integrated transport at depth z is given by their sum

$$\psi(z) = \psi_{\mathrm{Ek}}(z) + \psi_{\mathrm{sh}}(z) + \psi_{\mathrm{ex}}(z). \tag{1.2}$$

The latter term, the external mode ψ_{ex}, describes barotropic flow in the presence of topography. Integrating twice in the vertical, the geostrophic shear component of the flow ψ_{sh} is based on the thermal wind relation. The mathematical integration of the thermal wind equation depends on the reference velocity which is a reference depth by its nature. The Ekman component ψ_{Ek} scales inversely with the zonal-wind stress at the surface. Commonly, it is assumed that the zonal-mean velocity associated with the Ekman component is subdivided into

$$v_{\mathrm{ek}} - \bar{v}_{\mathrm{ek}}. \tag{1.3}$$

Here, v_{ek} is the surface Ekman flux occuring in the surface layer that has a specific depth Δz and $\bar{v}_{\mathrm{ek}}$ is the barotropic compensation. That is to say, the

latter is the surface Ekman flux divided by the longitude-depth section A at depth z in order to have a depth-independent interior return flow.

Assuming that Ekman compensation is barotropic is itself based on the assumption that the basinwide density structure cannot adjust fast enough to changes in the wind field. The validity of the assumption depends thus on the relevant timescale. Assuming barotropic or baroclinic Ekman compensation influences the geostrophic shear component because the depth of the level of no motion or reference velocities such as bottom velocities change. My findings support baroclinic Ekman compensation which makes the level of no motion a proxy for northward overturning as we shall see.

1.3 Second paper under Climate dynamics

In general, climate dynamics analyzes the dynamics of Earth's climate using a system approach. It is beyond the physical description of its climate components. More precisely, it analyzes the physical processes that change the distribution of climate fields and climate as a property of the system. Contemporary climate dynamics is based on different epistemeological views (Parker, 2018). The so called actualist view defines climate by the actual conditions in the climate system such as the statistical distribution of those conditions. It is the systematic change in the long-term statistics of climate. For instance, internal variability is analyzed under the actualist approach. By its nature, this approach is more related to climatology rather than modern climate dynamics. The latter, by contrast, relies on a dynamical system perspective, and climate is associated with climate attractors. The second paper of the dissertation relates to dynamical system theory. In this paper, I analyze the response of the climate system to radiative perturbations which can be captured by an autonomous dynamical system.

The Earth's climate is forced by different types of forcing such as incoming solar radiation or the composition of Earth's atmosphere. A major branch of literature analyzes how perturbations force or change the Earth's energy

balance and temperature adjustment. The dynamical system approach uses the concept of radiative forcing which is often defined as the net radiative imbalance at the tropopause immediately caused by the radiative perturbation. Actually, there exist a range of definitions of the concept of radiative forcing, which rely on different mathematical representations. Major radiative forcings are greenhouse gases and aerosols, using incoming solar radiation as a background boundary condition. In the second paper of the thesis I consider the radiative forcing which arises from the forcing imposed by altered atmospheric CO_2. I then compute the equilibrium and transient response of the climate system in terms of the surface air temperature perturbation relative to preindustrial conditions. Physical feedbacks are considered from an integrative perspective using the change in the radiative imbalance and surface air temperature only.

Climate dynamics analyzes processes on all relevant timescales and uses paleoclimate reconstructions, observations and climate modeling. As previously mentioned, I make use of a climate modeling approach in which AOGCMs are needed because I focus on the long timescales of the surface air temperature adjustment to forcing. Actually, I combine AOGCM output and simple energy balance models that reproduce the AOGCM response under idealized forcing conditions. In these energy balance models, I use the surface air temperature as dependent variable in order to represent the surface air temperature adjustment as well as the top-of-the atmosphere (TOA) radiative flux. By their nature, the energy balance models used by the study rely on physical theory according to the dynamical system approach and understanding of the influence of the ocean on the evolution of the surface air temperature in response to forcing. The parameters of the energy balance models are estimated using AOGCM output in order to interpret the complex system response. I focus on the climate response on a centennial timescale to investigate the major influence of the Earth's ocean on the climate system adjustment timescales. That is, I focus on the inertia of the climate response on the relevant timescale, which strongly depends on the thermal inertia of the ocean. It is the first study that analyzes the adjustment

timescale(s) of long-term climate change based on physical understanding using the concept of feedback temperature dependence and effective ocean heat capacity. It is the first study that considers explicitly the possibility that the adjustment timescales may also vary with time due to the particular role of the ocean in setting the adjustment timescale(s) of long-term climate change. Besides forming a consistent theory on varying adjustment timescales, it demonstrates the need for AOGCM development because of intermodel spread among state-of-the-art climate models.

The ocean plays a fundamental role for the surface air temperature adjustment on a centennial timescale by storing and redistributing heat. In contrast to the land, it has a high thermal conductivity, and components such as Ekman pumping force the ocean to take up heat advectively, in addition to diffusive ocean heat uptake. At the same time, heat storage by the ocean does not compensate for the net radiative imbalance such that meridional heat transport takes place. In this connection, also the MOC and AMOC play a fundamental role in changing the climate response to forcing. In fact, heat storage by the ocean depends on the relevant timescale considered. Considering the thermal inertia on a decadal and centennial timescale over the last century, thermal heat storage in response to global warming mainly occurs in the upper kilometer of the ocean. Greater depths than the average depth are achieved in regions of Ekman pumping and deep water formation. On longer timescales such as paleoclimates, the full depth of the ocean must be considered.

At this point, I would like to explain the inexperienced reader the study subject of the second paper of the dissertation in a more explicit and tangible way. I focus on the evolution of the surface air temperature in response to various step forcing associated with atmospheric CO_2. I use the temperature perturbation relative to preindustrial conditions. I then differentiate between the fast temperature adjustment on a decadal timescale and the slow temperature adjustment on a centennial timescale by separating these modes at year 21 (Fig. 1.2). The fast mode T_{F} and the slow mode T_{S} separate well at year

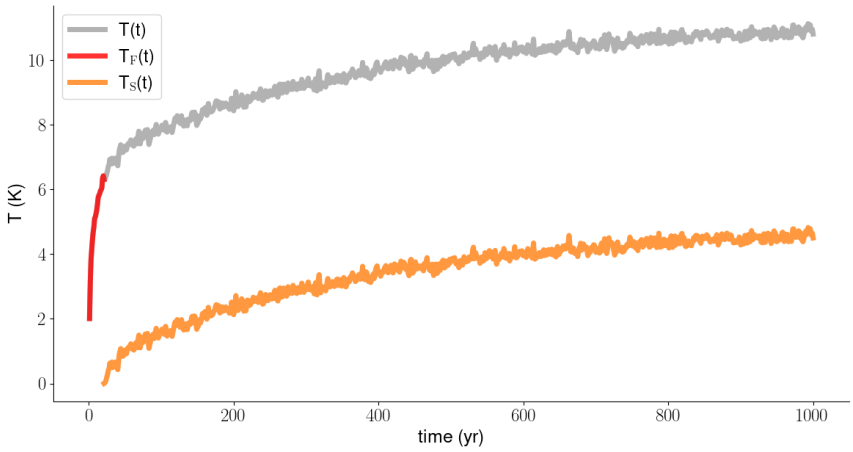

Figure 1.2: The surface air temperature adjustment $T(t)$ in the 8XCO2 experiment with the climate model MPIESM1.2L-R. Atmospheric CO_2 is eight times the preindustrial value. I show the fast mode T_F and the slow mode T_S.

21 in CMIP6 experiments (not shown), and a two-mode approximation is common procedure to describe the temperature response as we learn during the course of the study. The separation of the fast mode and the slow mode is set by the efficiency of ocean heat uptake. However, changing radiative feedbacks may change its temporal behavior. Furthermore, the timescale of the slow mode may vary with time or the slow mode may in fact be multiple modes due to its dependence on the ocean circulation.

1.3.1 Study framework

I put forward the idea that the adjustment timescale of long-term climate change depends on both the climate state and the evolution of time, with the surface air temperature being the state-variable. I use abrupt CO_2 experiments with atmosphere-ocean general circulation models (AOGCMs) to demonstrate the state- and time-dependence of the adjustment timescale on a centennial timescale. The climate response is interpreted by means of energy balance models. The timing of long-term climate change is strongly related

to the adjustment of the ocean component in the Earth system, since the slow processes of the climate response to forcing are related to the thermal inertia of the intermediate and deeper ocean (e.g. Dickinson and Schaudt, 1993)

A simple mixed-layer energy balance model for the global mean surface temperature response to forcing is given by

$$C\frac{\mathrm{d}T}{\mathrm{d}t} = F + \lambda T, \tag{1.4}$$

where C is the effective heat capacity of the ocean mixed-layer, T is the surface temperature perturbation relative to a reference state, F is the radiative forcing which is e.g. the forcing by atmospheric CO_2 or aerosols, and λ is the feedback parameter. In equilibrium, it is called the linear forcing-feedback framework. It is a first-order differential equation which analytical solution is given by $T(t) = \frac{F}{-\lambda}(1 - e^{-t/\tau})$. The equilibrium climate sensitivity is $T(\infty) = \frac{F}{-\lambda}$ and thus linear in forcing. The temporal adjustment is described by the e-folding timescale $\tau = \frac{C}{-\lambda}$ at which the single e-folding mode unfolds. That is to say, the response times of the temperature adjustment depend on C and λ. The stronger the feedback parameter or the smaller the effective heat capacity, the more rapidly the system adjusts to forcing. In fact, λ itself may depend on temperature which gives rise to temperature or forcing dependent adjustment timescales. At the same time, C may not be constant but time-dependent due to the changes in the ocean circulation and diffusive ocean heat uptake in response to global warming, or a spatial pattern of local heat capacities that prescribes the thermal inertia geographically. It is possible that long-term climate change may be described by multiple modes instead of a single mode. I essentially address these research questions in an experimental way by using abrupt CO_2 experiments.

1.3.2 Abrupt CO_2 experiments

Abrupt CO_2 experiments provide understanding on the underlying physical dynamics simulated by AOGCMs. Commonly, they provide different forcing levels by which results can be generalized. In general, understanding from step forcing experiments with AOGCMs is applicable to climate projections (e.g. Good et al., 2013; O'Neill et al., 2016) or different response theories such as linear response theory (e.g. Hasselmann et al., 1993). Under abrupt CO_2 experiments radiative feedbacks are quantified (e.g. Hansen et al., 1984; Soden and Held, 2006; Colman and McAvaney, 2009; Andrews et al., 2012; Mauritsen et al., 2018; Bloch-Johnson et al., 2020) and understanding on AOGCM behavior is gained (e.g. Armour et al., 2013; Geoffroy et al., 2013a,b; Rohrschneider et al., 2019). For instance, energy balance models fitted to abrupt CO_2 experiments can be used to predict future climate change cost-effectively (Good et al., 2013). These energy balance model can thus be used to predict the temporal behavior of the climate response under different scenarios and at different timescales. They can also be used to assess the importance of different modes of the climate response at different times in AOGCM projections. I use abrupt CO_2 experiments to demonstrate the state-dependence of the adjustment timescale of long-term climate change as well as to demonstrate a systematic time-dependent component of the adjustment timescale which is present at the different forcing levels.

1.3.3 Feedback temperature dependence

The radiative feedback of the climate system is actuated by the temperature perturbation of the climate system and determines its climate sensitivity. It is the change in radiation with the change in surface temperature. Assuming linearity, the radiative feedback of the climate system can be determined by $\lambda = \mathrm{d}N/\mathrm{d}T$ where N is the global mean energy budget or net top-of-the-atmosphere (TOA) imbalance and T is the global mean surface temperature perturbation relative to the control state or preindustrial conditions. Individual feedbacks are commonly known as the Charney-type feedbacks (Charney et al., 1979) which is the Planck feedback, the water vapor feedback, the

cloud feedback, the albedo feedback, and the lapse rate feedback. In a reference system such as the control state, all fields are fixed, whereas they vary in the case of the perturbation. First-order Taylor series with respect to the partial derivatives in temperature and climate constituents is commonly used to determine the climate feedback and relative contributions from temperature and climate constituents (e.g. Treneberth, 1992; Knutti and Rugenstein, 2015). Feedbacks, however, can be highly nonlinear (e.g. Budyko, 1969; Roe and Baker, 2007; Zaliapin and Ghil, 2010; Roe and Armour, 2011; Meraner et al., 2013; Bloch-Johnson et al., 2015, 2020). Second-order Taylor expansion with respect to the total derivative in temperature gives a nonlinear term which can be denoted as feedback temperature dependence. That is,

$$\mathrm{d}N = \frac{\mathrm{d}N}{\mathrm{d}T}\Delta T + \frac{1}{2}\frac{\mathrm{d}^2N}{\mathrm{d}T^2}\Delta T^2 + O(\Delta T^3), \tag{1.5}$$

where $a = \frac{1}{2}\frac{\mathrm{d}^2N}{\mathrm{d}T^2}$ is the coefficient for feedback temperature dependence.

A common assumption is that the radiative feedback that is actuated by the surface temperature change is independent of the degree of warming. That is to say, a common assumption in the climate community is that there is no feedback temperature dependence and the radiative feedback is thus constant with forcing (e.g. Gregory et al., 2004). The global feedback may depend on time because it is actuated by multiple modes which are associated with different radiative feedbacks (Senior and Mitchell, 2000; Winton et al., 2010; Armour et al., 2013; Geoffroy et al., 2013a,b; Rohrschneider et al., 2019). However, feedback temperature dependence changes the equilibrium temperature response in a nonlinear way (e.g. Bloch-Johnson et al., 2015, 2020) and likely influences the response times or timescale of the surface temperature adjustment. Mathematically, it introduces a timescale that depends on the degree of warming or forcing (Rohrschneider et al., 2019). By its nature, positive feedback temperature dependence becomes more important with higher warming and it is thus important for long-term climate change. We shall see whether the influence of feedback temperature dependence on the timing of long-term climate change is substantial.

1.3.4 Inertia

The adjustment timescale of long-term climate change can also be time-dependent in the sense that the effective heat capacity or thermal inertia is not constant in time. The ocean effective heat capacity C is commonly computed by $c_p \rho_\mathrm{r} D$, where c_p is the specific heat, ρ_r is the reference density, and D is the depth of the water column. Different components such as the atmosphere, the ocean mixed-layer, or the deep ocean have different heat capacities. Commonly, the atmosphere is assumed to be an instantaneous balance. The mixed-layers have heat capacites of O(10) and the deep ocean has a heat capacity of O(100), according to common assumptions of the components' depths which is not outlined here. That is, oceanic timescales determine the timescales of realized warming. These heat capacities such as the deep ocean capacity are commonly assumed to be constant. However, the circulation of the deep ocean may change (e.g. Knutti and Rugenstein, 2015) and diffusive ocean heat uptake progresses over time (Hansen et al., 1985; Wigley and Schlesinger, 1985), which can make the deep ocean effective heat capacity time-dependent. A time-dependent effective ocean heat capacity gives rises to a time-dependent adjustment timescale, which has not been explored yet in the current literature. Different components such as an ocean mixed-layer and the deep ocean component of the Earth system give rise to multiple modes of the climate response. At the same time, these modes of the climate response emerge from the coupling between the heat reservoirs such as the heat flux from the mixed-layer into the deep ocean, which may also excite a time-dependent timescale. Another approach is that there exist a geographic pattern of the adjustment timescale, which is associated with different geographic regions of thermal inertia and radiative feedbacks. In this chapter I demonstrate that the adjustment timescale of long-term climate change indeed depends on the evolution of time, which may be approximated by a multiple timescale structure, or vice versa.

The surface air temperature response is commonly described by a fast temperature mode on a decadal timescale and a slow temperature mode on

a centennial timescale (e.g. Geoffroy et al., 2013a,b; Rohrschneider et al., 2019). I analyze the slow mode of the climate response after the decadal temperature adjustment.

1.4 Connection between the studies

This section briefly reviews the connection between the first paper of the dissertation and the second paper of the dissertation from a conceptual point of view. The AMOC redistributes a significant amount of heat on a planetary scale. The spatial distribution of the surface air temperature is thus related to the AMOC. Hence, the climate state depends on the AMOC, and radiative feedbacks in turn depend on the climate state. Accordingly, accurate understanding of the AMOC is necessary to simulate appropriately ocean dynamics and thus climate dynamics in terms of ocean heat uptake and heat transport. Considering the response of the surface air temperature to CO_2 forcing, the efficiency of ocean heat uptake determines the amplitude and temporal behavior of the fast adjustment on a decadal timescale and the slow adjustment on a centennial timescale. Furthermore, there should be a geographic pattern of local effective ocean heat capacities which arise from the ocean circulation such as the AMOC and dynamic components such as Ekman pumping. Together with radiative feedbacks, the geographic pattern of effective ocean heat capacities gives rise to a geographic timescale pattern of climate change. This timescale pattern may additionally depend on time due to changes in the ocean circulation such as changes in the strength of the AMOC over time.

Part I

A different view on the AMOC

Chapter 2

Publication

Bibliographic Information

Rohrschneider T., Baehr, J., Lüschow, V., Putrasahan, D., and J. Marotzke (2021): The depth scales of the AMOC on a decadal timescale. Submitted to Ocean Science.

Author contribution

TR conducted the research and developed the coding scripts associated with the present study. TR developed the text of the present manuscript. JB, VL, DP, and JM reviewed the manuscript and checked the consistency of the research results.

Abstract

We use wind sensitivity experiments to understand the wind forcing dependencies of the level of no motion as the depth of maximum overturning and the e-folding pycnocline scale as well as their relationship to northward transport of the mid-depth Atlantic meridional overturning circulation (AMOC). In contrast to previous studies, we investigate the interplay of nonlocal and local wind effects on a decadal timescale. We use 30-year simulations with a

high-resolution ocean general circulation model (OGCM) which is an eddy-resolving version of the Max Planck Institute Ocean Model (MPIOM). Our findings deviate from the common perspective that the AMOC is a nonlocal phenomenon only, because northward transport and its depth scales depend on both nonlocal Southern Ocean wind effects and local wind effects in the northern hemisphere downwelling region where Ekman pumping takes place. Southern Ocean wind forcing predominantly determines the magnitude of the pycnocline scale throughout the basin, whereas northern hemisphere winds additionally influence the level of no motion locally. In that respect, the level of no motion is a better proxy for northward transport and mid-depth velocity profiles than the pycnocline scale, since the wind forcing dependencies of the level of no motion and maximum overturning are equal. The changes in maximum overturning with wind forcing are explained by the changes in the level of no motion only. This is because wind-driven Ekman compensation is baroclinic and occurs above the level of no motion, and the internal vertical velocity shear that is not influenced by the external Ekman cells stays approximately constant. The analysis of the wind experiments suggests a hemisphere-dependent scaling of the strength of AMOC. We put forward the idea that the ability of numerical models to capture the spatial and temporal variations of the level of no motion is crucial to reproduce the mid-depth cell in an appropriate way both quantitatively and dynamically.

Editing note

Equations and figures are labeled numerically by the indices $i.j$. Following the publication, I refer to these equations and figures by referring to the second index j. Sections are labeled numerically by the indices $i.j.k$. Following the publication, I refer to these sections by referring to the second and third indices $j.k$.

2.1 Introduction

To date and despite a wide range of theoretical and experimental studies, we do not fully understand inter-hemispheric overturning of the mid-depth cell in the Atlantic and the role of southern and northern hemisphere processes like the response to changes in the surface winds. Current understanding of the Atlantic meridional overturning circulation (AMOC) suggests an interplay between adiabatic pole-to-pole overturning (e.g. Toggweiler and Samuels, 1995; Wolfe and Cessi, 2011) and low-latitude diabatic forcing that establishes a balance between downwelling of heat and upwelling of deep waters (e.g. Munk and Wunsch, 1998; Marotzke, 1997). Especially in connection to Southern Ocean processes and the Antarctic circumpolar current (ACC), the effect of winds on the AMOC and basin-wide density stratification has gained considerable attention during the last two decades (e.g. Marshall and Speer, 2012; Johnson et al., 2019). Poorly understood, however, is the influence of winds on inter-hemispheric overturning in the Atlantic away from the surface Ekman layer. This paper presents an analysis of wind sensitivity experiments in order to provide insight into the wind forcing dependence of the inter-hemispheric circulation by understanding the behavior of the depth scale(s) of the AMOC. We focus on the response of the AMOC to wind forcing on a decadal timescale after the realization of major adjustments.

The research of the present study is inherently about depth scaling that reflects the wind forcing dependence of the AMOC. Oceanographers use theoretical scaling relationships to provide conceptual understanding and to estimate the strength of the AMOC in response to different forcings. Nowadays, the most common analytical model to describe meridional overturning of the upper branch of the AMOC is the pycnocline model (Gnanadesikan, 1999). According to this model, the vertically integrated northward transport in the northern hemisphere is proportional to the basin-averaged e-folding pycnocline scale. The pycnocline scale is a measure for density stratification and describes how density unfolds vertically. The deeper the pycnocline scale, the stronger the transport, with the assumption that zonal or meridional

density gradients are fixed. The depth scale itself is determined by Southern Ocean winds and eddies, diapycnal upwelling in the tropics, and North Atlantic deep water formation. In the same manner, a wide range of theoretical studies or scaling arguments rely on the assumption that the pycnocline scale translates a zonal or meridional density gradient into horizontal force that drives northward flow (e.g. Robinson and Stommel, 1959; Bryan, 1987; Marotzke, 1997; Marotzke and Klinger, 2000). The majority of the different scalings makes use of the thermal wind relation $\partial v/\partial z = -\Delta\rho_{\mathrm{x}} g/(\rho_0 f L_{\mathrm{x}})$ which is based on the geostrophic and hydrostatic approximations of the momentum equations. The left-hand side represents the vertical shear of the zonal-mean meridional velocity, $\Delta\rho_{\mathrm{x}}$ is the west-east density difference, g is the gravitational force, ρ_0 is a reference density, f is the Coriolis parameter, and L_{x} is the zonal extent. The thermal wind relation is also key for reconstructing the AMOC strength using observations which are boundary densities (Hirschi et al., 2003; Baehr et al., 2004; Hirschi and Marotzke, 2007; Baehr et al., 2009). In general, the theoretical and experimental studies have in common that they integrate vertical shear or zonal or meridional density gradients twice in the vertical, $\psi \propto \Delta\rho\ \eta^2$, where ψ is the strength of northward overturning, $\Delta\rho$ is the density gradient, and η is the depth scale. Different assumptions like advective-diffusive balance modify the simple scaling relationship considered here.

The nonequivalance of different depth scales of the AMOC has first been noted in Scott (2000), and recent studies put into question whether the pycnocline scale is the appropriate depth scale to estimate the AMOC strength. For instance, Levermann and Fuerst (2010) find that the pycnocline scale and meridional density gradients are mutually independent. Using a coarse-resolution model, Griesel and Maqueda (2006) show that the pycnocline scale does not scale northward transport in experiments in which density gradients are artificially modified. In this connection, DeBoer et al. (2010) find that the depth of maximum overturning (level of no motion) is a more appropriate parameter to scale maximum overturning. Shakespeare and Hogg (2012) use the depth scales of the overturning extrema to build an analytical model for

both the mid-depth cell and the abyssal ocean. Finally, Marshall and Johnson (2017) combine the depth of maximum overturning (level of no motion) and the e-folding pycnocline scale to express the relative strengh of the ACC and the AMOC. The present study adresses the wind forcing dependencies of the level of no motion, pycnocline scale and northward transport. Understanding the wind forcing dependence of the AMOC by understanding its depth scales makes the underlying research question twofold, in the sense that we discuss the wind forcing dependence of the AMOC using the depth scales and we discuss whether the depth scales are proxies for northward transport to understand the wind forcing dependence. We hypothesize that the level of no motion is a proxy for northward transport in the inter-hemispheric cell because the background velocity shear of the meridional velocity may stay constant under changing wind forcing. In this connection, the study is based on different ways or definitions which describe meridional flow in order to analyze how the changes in wind forcing are translated into the changes in the AMOC.

We focus on the inter-hemispheric region 30S-30N and analyze the interplay of nonlocal wind forcing over the Southern Ocean and local wind forcing in the northern hemisphere downwelling region where Ekman pumping takes place. The absence of continental barriers in the Southern Ocean and the strong input of momentum at the surface establishes a deep reaching Ekman overturning cell. The steepening of isopycnals, which is compensated by baroclinic instability that induces an eddy field, is thought to influence deep stratification and northward transport throughout the basin (e.g. Vallis, 2000; Klinger and Cruz, 2009; Allison et al., 2011). The zonal peridiocity of the ACC boosts the strength of the AMOC in response to an increase in Southern Ocean wind forcing (Klinger et al., 2003, 2004). By contrast, the local influence of northern hemisphere winds on the AMOC is less understood. Tsujino and Suginohara (1998) propose an enhancement of the thermohaline circulation due to a wind-driven buoyancy gain in the upwelling region of the northern hemisphere north of the inter-hemispheric region. Recently, Cessi (2018) finds that the inter-hemispheric cell weakens in response to increased

westerlies at the northern high latitudes. Considering the northern hemisphere downwelling region at low and mid-latitudes, the local influence of northern hemisphere wind forcing on the AMOC is commonly ignored in the scientific literature on the AMOC. A study by Cabanes et al. (2008) already indicates that wind stress curl variations may play a crucial role in setting the AMOC shear component which is altered by the surface forcing according to this study. The wind stress curl is computed by the rotation of the surface wind vector and establishes downwelling or upwelling regions. In this connection, vertical Ekman pumping emerges from the forcing imposed by the wind stress curl at the surface. We address the question how changes in both nonlocal and local wind forcing influence the AMOC. We hypothesize that the influence of northern hemisphere winds on the AMOC is substantial.

To answer the specific questions that are outlined above, we use 30-year wind experiments with a high-resolution ocean general circulation model (OGCM). We expect a robust response of the AMOC on a decadal timescale because major adjustments by basin-wide wave propagation are realized on this timescale. The basin-wide transmission of density signals by wave propagation occurs on a pentadal and decadal timescale. Limiting the analysis to the adjustment on a decadal timescale makes it possible to use presumably more realistic eddy-resolving wind experiments rather than fully equilibrated low-resolution model runs. In this way we avoid uncertainties introduced by eddy parameterization. High-resolution model output is needed because we analyze the relationships between depth scales as reference depths and meridional transport and its vertical velocity shear. These relationships depend sensitively on the vertical and horizontal model resolution as wave propagation of density signals does.

To the best of our knowledge and despite a wide range of theoretical and modeling studies on the Atlantic circulation, the research questions of this study have never been answered in an explicit way. That is to say, from an overarching perspective we analyze whether the depth scales are proxies for northward transport in the inter-hemisperic cell, and we ask whether

we should adopt a more nonlocal or local perspective with respect to inter-hemispheric overturning and hemispheric differences.

In the following section we briefly describe the different experiments and the experimental strategy. In section 3 we describe the differences in density stratification with the changes in wind forcing as well as the wind forcing dependencies of the level of no motion, the pycnocline scale and northward transport. In section 4 we analyze the relationship between velocity profiles or shear and the depth scales.

2.2 Experiments and methods

2.2.1 Numerical model and experiments

We use wind experiments conducted with a vertically and horizontally high-resolution, eddying configuration of the Max Planck Institute for Meteorology ocean model (MPIOM). The version is called TP6ML80 and has been developed within the German Consortium project STORM (von Storch et al., 2012). It is based on a tripolar grid with a horizontal resolution of 0.1 degrees and a vertical resolution of 80 unevenly spaced levels. Compared to low-resolution MPIOM versions, we assume better model physics in terms of the resolution of mesoscale eddies as well as wave propagation. (Gutjahr et al., 2019) already indicate that the high-resolution MPIOM configuration reveals the most realistic simulation compared to low-resolution MPIOM versions in terms of the mean state of the ocean. For instance, a cold bias in sea surface temperature over the Southern Ocean is strongly reduced, because the resolved eddies better influence the flattening and cropping of isopycnals compared to the Gent-McWilliams thickness diffusivity parameterization (Gent et al., 1995). We do not expect that the wind forcing dependence of the AMOC depth scales differs between high- and low-resolution model runs. However, the horizontal transmission of density signals is sensitive to the horizontal model grid and the accumulation of vertical shear is sensitive to the vertical model grid.

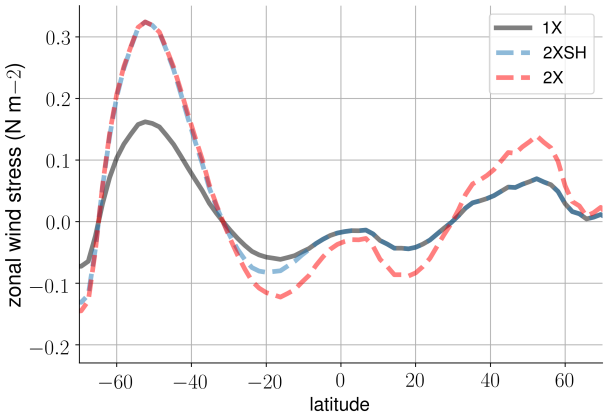

Figure 2.1: The zonal-mean zonal wind stress in the 1X experiment (black), 2XSH experiment (blue), and 2X experiment (red) (Lüschow et al., 2021).

We have available three different wind experiments with realistic geometry (Lüschow et al., 2021); Table 1. In the 1X experiment, the standard surface momentum and buoyancy fluxes from NCEP-NCAR reanalysis-1 (Kalnay et al., 2018) are applied. We are not interested in high-frequency variability and therefore change the monthly-mean climatalogy of the suface wind stress only. In the 2XSH experiment, the monthly climatology of the zonal and meridional surface wind stress is doubled only over the Southern Ocean. By applying a sine function which declines to zero towards the equator in the southern hemisphere, we obtain a smooth transition of the surface wind stress towards the original surface momentum fluxes. In the 2X experiment, we double the monthly climatology of the zonal and meridional surface wind stress in both the northern and southern hemispheres throughout the basin. Fig. 1 shows the climatology of the zonal surface wind stress of the different experiments. The wind experiments are initialized with the state of the 1X experiment, and the wind forcing is switched on at year 1980. Because the computational costs for an eddy-resolving simulation are still large, the simulation period is only until year 2010. Using monthly-mean output, we focus on the time-window 1991 to year 2010 after the realization of major adjustments to the changes in the surface wind stress in order to analyze

the AMOC response to forcing. That is, we allow for a decadal adjustment of the AMOC and density field towards stationarity before using the model time series. Analyzing the decadal response of the AMOC to Southern Ocean wind forcing, Klinger and Cruz (2009) show that the AMOC in the source region adjusts on an inter-annual timescale. Lüschow et al. (2021) discuss the adequacy of the wind experiments in terms of integration length.

2.2.2 Experimental strategy and quantities

The AMOC is described by the overturning streamfunction in the latitude-depth section, $\psi(t, z, y) = \int_z^D \int_{x_e}^{x_w} v(t, z, y, x)\, dx\, dz$, where v is the meridional velocity, z is the depth with D the depth at the bottom of the ocean column, and x_e and x_w are the eastern and western boundaries of the Atlantic basin.

We focus on the upper, northward flowing branch of the mid-depth cell which rotates clockwise, viewed from the east. Fig. 2a,b,c show the time-mean (1991-2010) overturning cells in the wind experiments. Analyzing the AMOC in the inter-hemispheric region 30S-30N south and north of the equator, we explore the nonlocal response to changes in Southern Ocean winds and local wind effects in the downwelling region of the northern hemisphere. In general, the mid-depth cell strengthens with higher wind forcing over the Southern Ocean. However, at this point, from Fig. 2 we cannot capture the details of the meridional velocities in terms of spatial variations that may influence the relationship between overturning and its depth. The northward flow seems to be continuous and contiguous throughout the basin, but regional dynamics may give rise to local wind forcing dependencies of the AMOC which can be hardly identified away from the surface Ekman layer. The surface Ekman flux, for instance, is compensated by an interior return flow which changes the meridional transport at different depths. Furthermore, the wind stress curl over the basin imposes a forcing that may change stratification and the meridional transport and its depth locally.

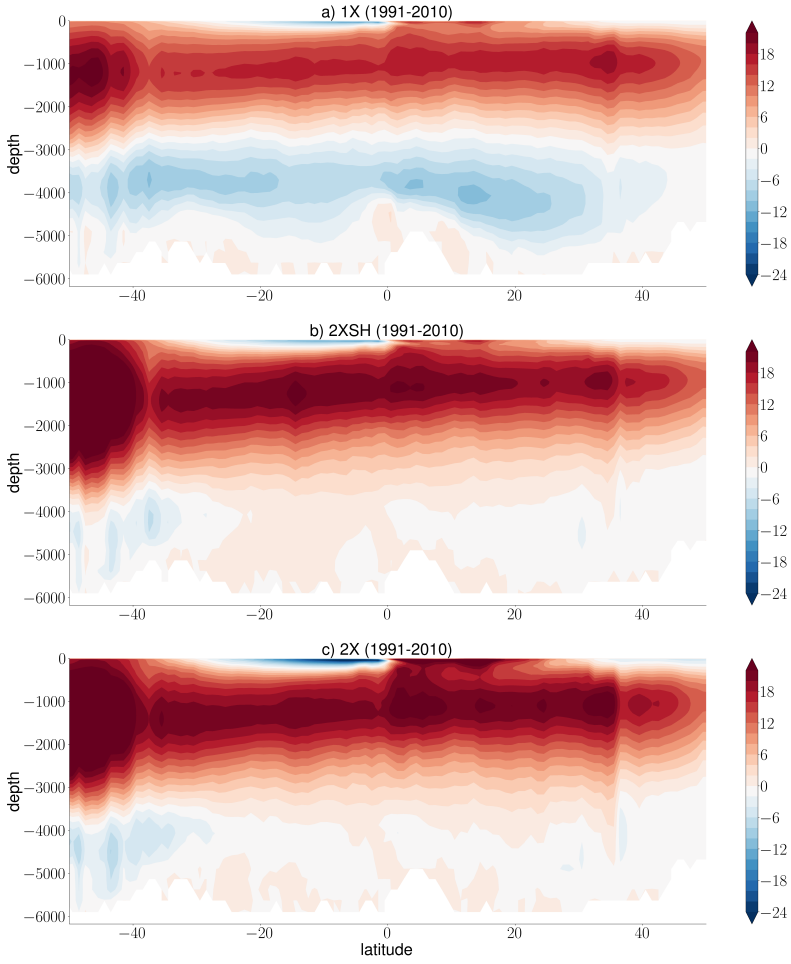

Figure 2.2: The time-mean AMOC streamfunctions (1991-2010) in the (a) 1X experiment, (b) 2XSH experiment, and (c) 2X experiment.

Table 2.1: Overview of the experimental strategy

1X (1991-2010)	The reference experiment which mimics observed conditions
2XSH (1991-2010)	We double the monthly climatology of the zonal and meridional surface wind stress over the Southern Ocean only in order to analyze the nonlocal effects of Southern Ocean winds
2X (1991-2010)	We double the monthly climatology of the zonal and meridional surface wind stress throughout the basin in order to analyze the interplay between nonlocal and local wind effects and extract local wind forcing dependencies

Table 2.2: Experimental quantities

ψ	AMOC streamfunction
ρ	Potential density
η_ψ	Level of no motion
η_ρ	Pycnocline scale
η_w	Advective depth scale
ψ_t	Total maximum overturning streamfunction
ψ_g	Geostrophic approximation of the maximum overturning streamfunction
$\frac{\partial \psi}{\partial z}$	Vertical derivative of the overturning streamfunction (velocities)
$\frac{\partial^2 \psi}{\partial z^2}$	Second vertical derivative of the overturning streamfunction (shear)
ψ^*	Maximum overturning streamfunction associated with the level of no motion

We limit our analysis of the different experiments to a set of quantities (Table 2). The level of no motion of the mid-depth cell is the depth of maximum overturning where zonally averaged velocities reverse in sign, $\eta_\psi = z_{\psi(\max)}$. We use the monthly-mean outcome of the related quantities and subsequently take the time-mean (1991-2010). In doing so, we describe in more detail the behavior of the level of no motion and its relationship to northward transport. The reader should notice that the level of no motion incorporates nonlinearities because it is an integrated quantity and related to the zonal-mean meridional velocity. The level of no motion is not a zonal-mean quantity that is averaged over the zonal extent. Further, we avoid that the algorithm selects a model level within the depth range of the surface Ekman layer or perturbations that emerge from equatorial upwelling.

The pycnocline scale is the single mode e-folding scale for vertical density stratification, and the profile of the latter is assumed to be exponential

and self-similar. We use the following fitting algorithm at each grid cell and subsequently take the zonal and temporal mean, $\eta_\rho = 2\frac{\int_{z_\mathrm{r}}^{0}(\rho-\rho_\mathrm{r})\ z\ dz}{\int_{z_\mathrm{r}}^{0}(\rho-\rho_\mathrm{r})\ dz}$ (Gnanadesikan, 1999; Gnanadesikan et al., 2007; DeBoer et al., 2010). The reference depth is $z_\mathrm{r} = -2500$ meters, and ρ_r is the potential density at the reference depth. Using this algorithm we take the e-folding scale twice. In this way, 80 to 90 percent of the vertical density change is scaled, which scales the upper branch of the mid-depth cell. In some regions, especially at the lateral margins of the basin, the profile for vertical density stratification may become more linear and deviate from an exponential profile. However, such deviations from a perfectly exponential profile do not restrict the ability of the pycnocline scale to interpret density stratification in different regions in the sense that it is an independent measure as long as density increases with depth.

We make use of a third depth scale and compute the advective depth η_w in order to provide the linkages between the differences in the wind stress curl, the differences in the density field ρ, and the depth scales. The advective depth scale gives the vertical depth range for local Ekman pumping and likewise emerges from the forcing imposed by the wind stress curl at the surface. It thereby scales the maximum change in density stratification associated with the rotation of the surface wind vector. Theory of wind driven changes in stratification can be traced back to the development of the planetary geostrophic equations (e.g. Welander, 1959; Bryan, 1987) and the related theory on the ventilated thermocline in the subtropical region (Luyten et al., 1983). Classical scaling of the thermocline equations suggests that the advective depth scale is directly proportional to the square-root of the local Ekman pumping velocity W_E (e.g. Vallis, 2000), $(\frac{W_\mathrm{E} f L^2}{g'})^{0.5}$, where f is the Coriolis parameter, L is the basin width, and g' is the reduced gravity. We compute the local Ekman pumping velocity W_E from the wind stress data of the wind experiments.

During the course of our study we analyze both the total maximum overturning streamfunction ψ_t and the geostrophic approximation of the maxi-

mum overturning streamfunction ψ_{g}; that is, the total streamfunction minus the surface Ekman flux. We compute both ψ_{t} and ψ_{g} because their wind forcing dependencies should be fundamentally different due to the interior, geostrophic return flow of the surface Ekman flux. In this way, we analyze the relationship between overturning and its depth using vertically integrated transport that may depend on the ageostrophic surface component by vertical integration.

We use the zonal surface wind stress τ_{x} to compute the strength of the surface meridional Ekman transport, $\int_{x_e}^{x_w} -\frac{\tau_{\mathrm{x}}(x,y,t)}{\rho_0 f} dx$, where ρ_0 is the reference density and f the Coriolis parameter. We do not substract the interior return flow of the surface Ekman flux. For the sake of simplicity a range of studies assumes that the interior return flow of the surface Ekman flux is barotropic even on longer than a monthly timescale (e.g. Hirschi and Marotzke, 2007; Moreno-Chamarro et al., 2016). Based on an idealized experiment with an OGCM, a recent study demonstrates that the return flow is baroclinic and has strong contributions at the upper levels of the ocean on the timescale considered here (Williams and Roussenov, 2014). On a monthly timescale, anomalies of the return flow are barotropic because the density field does not adjust (e.g. Jayne and Marotzke, 2001), but these anomalies are negligible in the set-up presented in this study and by their nature do not change the time-mean outcome. Later on, we support the perspective that the interior return flow of the surface Ekman flux is baroclinic. This finding has been demonstrated theoretically by McCreary and Lu (1994).

Finally, we analyze whether there are causal linkages between the changes in the depth scales and northward transport at different depths. Therefore, we compute the vertical derivative of the AMOC streamfunction $\frac{\partial \psi}{\partial z}$, which represents the zonal-mean meridional velocity scaled by the basin-width. We then compute the second derivative of the AMOC streamfunction $\frac{\partial^2 \psi}{\partial z^2}$, which represents the vertical velocity shear scaled by the basin-width. In this way, we analyze to which degree the changes in the northward transport of the mid-depth cell are directly related to the displacement of the level of no

motion. The computation of $\frac{\partial \psi}{\partial z}$ and $\frac{\partial^2 \psi}{\partial z^2}$ below the surface Ekman layer is independent of the way how we approximate the maximum overturning streamfunctions ψ_{t} and ψ_{g}. To finish our analysis, we compute the maximum overturning streamfunction ψ^* that is associated with the level of no motion only. We use the time-mean vertical velocity shear $\frac{\partial^2 \psi}{\partial z^2}$ of the 1X reference experiment and integrate vertically from the level of no motion in the 2XSH and 2X experiments to the top. Before averaging over the 20 years, we use the highest temporal resolution and compute the integral with the reference depth for each month in order to ensure the robustness of the results.

2.3 Wind forcing dependencies

2.3.1 Wind-driven changes in stratification

As a starting point, we highlight the differences in density stratification in the Atlantic basin between the wind experiments. Afterwards, we relate these differences to the level of no motion η_ψ and the pycnocline scale η_ρ. We normalize the zonal-mean potential density to highlight the differences in density stratification between the wind experiments, $\frac{\rho_0 - \rho}{\rho_0}$, with the reference density $\rho_0 = 1025$ kg m^{-3}. Fig. 3a,b show the time-mean difference in density stratification between the 2XSH and 1X experiment and the 2X and 1X experiment. Fig. 3c illustrates the advective depth scale η_{w} in the Atlantic. Within the range of the advective depth scale η_{w}, isopycnals shoal towards the equator due to equatorial divergence and deepen in the subtropical region towards higher latitudes due to the local forcing that is imposed by the wind stress curl. Deep stratification below η_{w} but within the depth range of the upper, northward flowing branch of the mid-depth cell reveals the same behavior in the southern hemisphere, but isopycnals rise constantly towards the region of North Atlantic deep water formation.

The time-mean differences in density stratification between the wind experiments mirror the experimental set-up of the present study. In general, Fig. 3a,b suggests that the difference in density stratification between the

2XSH experiment and the 1X experiment is driven by the wind stress curl over the Southern Ocean, which has a strong influence in the southern hemisphere, but deep isopycnals change even in the northern hemisphere. The change of the 2X experiment relative to the 1X experiment is driven by the change of the climatology of the wind stress curl in both hemispheres. Local Ekman pumping displaces isopycnals downward also north of the equator with a maximum change in the subtropical region, and this displacement is scaled by η_{w} (Fig. 3c). The influence of the local wind forcing prevails but deep isopycnals are also influenced nonlocally below η_{w}. Both nonlocal and local wind effects change the density field, and their relative influence on stratification depends on location and depth. In the following, we analyze how these changes in density stratification translate into changes in both depth scales η_ψ and η_ρ and maximum overturning ψ. Afterwards, in section 4, we discuss how the changes in wind forcing translate into changes in the level of no motion η_ψ from a generic point of view on the vertical velocity shear of the meridional velocity.

2.3.2 Level of no motion and pycnocline scale

Fig. 4 shows the meridional dependence of the level of no motion η_ψ and the zonal-mean pycnocline scale η_ρ in the wind experiments in order to explore the wind forcing dependencies of the depth scales. Considering the 1X experiment, the spatial variations of η_ψ and η_ρ coincide in the sense that both shoal towards the equator in the southern hemisphere and stay more or less constant or change slightly in the northern hemisphere. Although the general behavior of the level of no motion and the pycnocline scale coincides, the pycnocline scale η_ρ measures how density stratification unfolds over the ocean column. In contrast, the level of no motion is a single layer at a certain depth. By their nature, the level of no motion η_ψ and pycnocline scale η_ρ do not match exactly. Even though we know how density stratification unfolds, it is unclear whether the pycnocline scale represents the differences in stratification as found in the previous section.

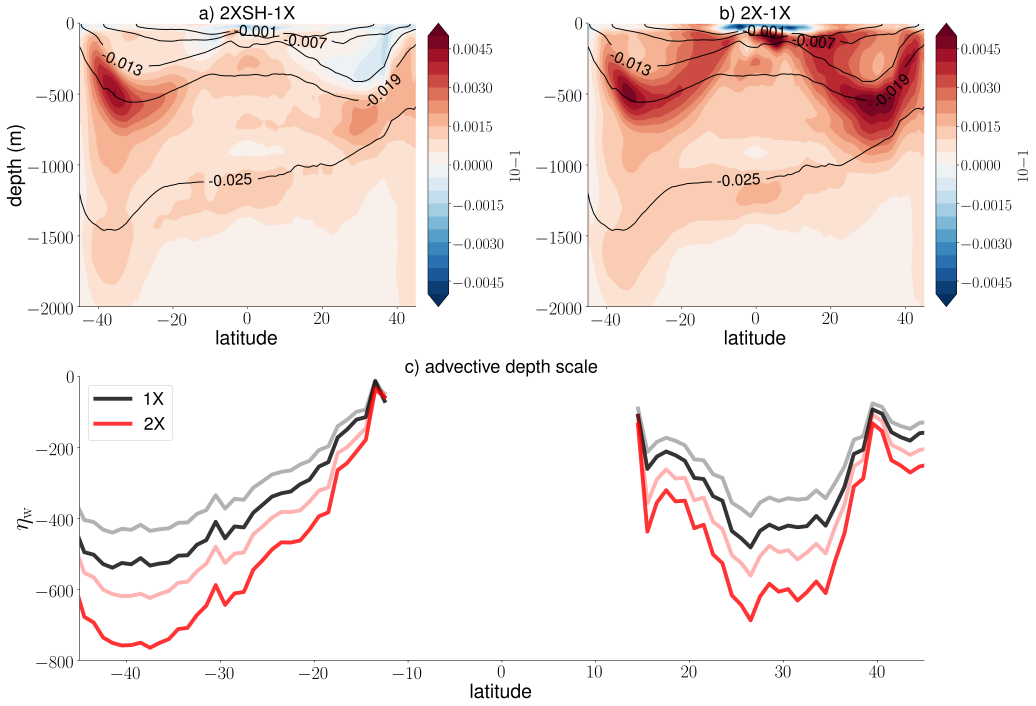

Figure 2.3: Differences in the zonal-mean density stratification averaged over the years 1991-2010: (a) the difference between the 2XSH and 1X experiments and (b) the difference between the 2X and 1X experiment. The black contour lines represent the zonal-mean density stratification (10^{-1}) in the 1X reference experiment. Density stratification is computed by $\frac{\rho_0 - \rho}{\rho_0}$, with the reference density $\rho_0 = 1025$ kg m^{-3}. In (c) we show the advective depth scale η_w in meters depth in the 1X experiment (black) and the 2X experiment (red), with the reduced gravity set to $g' = 0.013$ (opaque) and $g' = 0.02$ m s^{-2} (transparent). The smaller the value for the reduced gravity, the deeper the advective depth scale η_w.

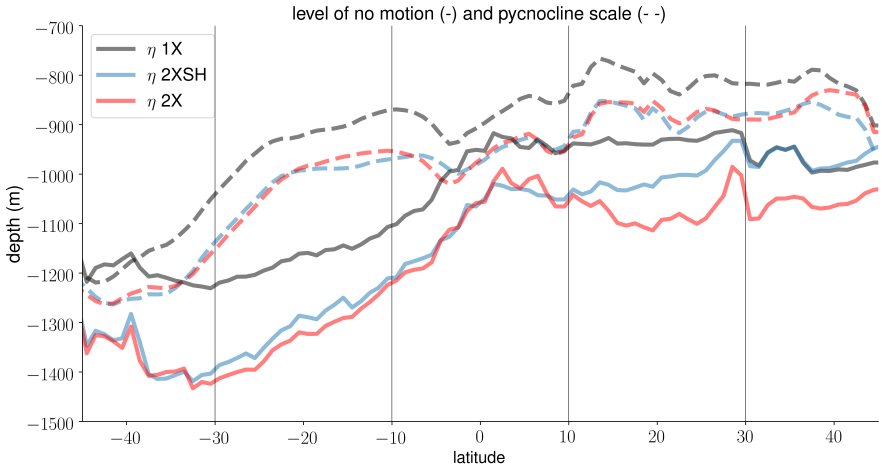

Figure 2.4: The time-mean (1991-2010) wind forcing dependencies of the level of no motion η_ψ (solid) and the pycnocline scale η_ρ (dashed) with respect to the 1X experiment (black), the 2XSH experiment (blue), and the 2X experiment (red).

The wind forcing dependencies of the level of no motion and the pycnocline scale differ. The pycnocline scale η_ρ deepens in the 2XSH and 2X experiments relative to the 1X reference experiments throughout the basin. The pycnocline scales η_ρ in the 2XSH and 2X experiments are congruent, and η_ρ is mainly determined by the wind stress over the Southern Ocean. Local changes in the wind forcing at lower latitudes and in the northern hemisphere do not change η_ρ significantly. In the northern hemisphere, density stratification approximately unfolds at the same scale despite the differences in density stratification at the depth of η_w. In the southern hemisphere, the wind forcing dependence of the level of no motion η_ψ is in line with the wind forcing dependence of pycnocline scale η_ρ. However, we find considerable differences between the wind experiments in the northern hemisphere due to an additional dependence on the local wind forcing. Wind forcing over the Southern Ocean nonlocally deepens the level of no motion η_ψ in the northern hemisphere. Yet, in addition to this nonlocal effect, a local effect acts on the level of no motion η_ψ because we observe differences in the northern hemisphere subtropical region between the 2XSH and 2X experiments. The

findings on the wind forcing dependencies of η_ψ correspond to those findings on the differences in density stratification between the wind experiments. The level of no motion η_ψ is connected to the advective depth scale η_w and Ekman pumping locally.

2.3.3 Maximum overturning and its depth

We now analyze the wind forcing dependence of the northward flowing branch of the mid-depth cell. We compute the total maximum overturning streamfunction ψ_t and the geostrophic maximum overturning streamfunction ψ_g. Conceptually, the differences between ψ_t and ψ_g provide insight on the degree to which the depth scale(s) are proxies for the strength of the AMOC. Computing the geostrophic maximum overturning streamfunction ψ_g, the level of no motion is unchanged, but the clockwise (upper) and counterclockwise (lower) rotating overturning cells are substantially altered. The maximum streamfunction ψ_t includes the surface Ekman flux and the maximum streamfunction ψ_g excludes the surface Ekman flux. However, the surface Ekman fluxes have to be compensated by an interior return flow that changes in relationship between overturning and its depth.

The wind forcing dependencies of the level of no motion and the total maximum overturning streamfunction are equal. By contrast, the wind forcing dependencies of the level of no motion and the geostrophic maximum overturning streamfunction are unequal. As a first step towards understanding, this behavior helps understand whether and why the level of no motion is a proxy for northward flow. Fig. 5 shows the meridional dependence of both the total and geostrophic maximum overturning streamfunction (ψ_t,ψ_g). Considering ψ_t, the southern latitudes of the southern hemisphere are strongly influenced by the surface Ekman flux which scales with the zonal wind stress. Northward of the Southern Ocean (30S-10S), the AMOC becomes increasingly geostrophic. In the southern hemisphere, the strength of the mid-depth cell increases with higher wind forcing, and we find a stronger

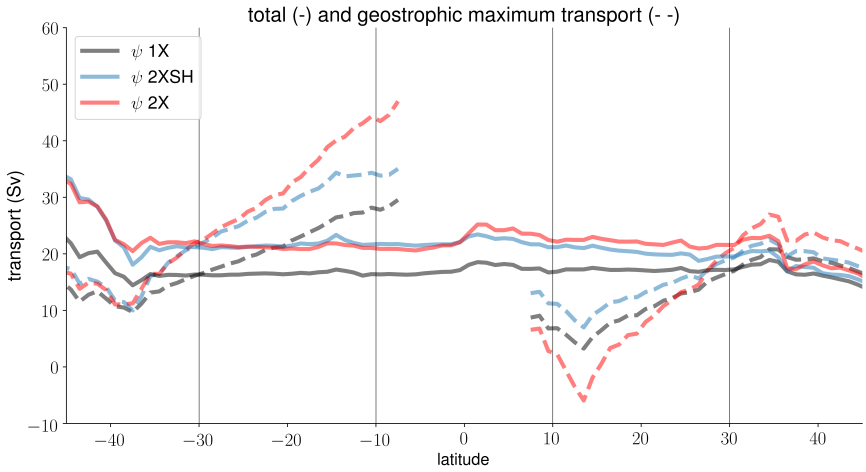

Figure 2.5: The time-mean (1991-2010) wind forcing dependencies of the total maximum overturning streamfunction ψ_{t} (solid) and the geostrophic maximum overturning streamfunction ψ_{g} (dashed) with respect to the 1X experiment (black), the 2XSH experiment (blue), and the 2X experiment (red). Considering ψ_{g}, we exclude the equatorial band where the approximation of the surface Ekman flux breaks down.

transport in the 2XSH and 2X experiment than in the 1X experiment. In this region, the total maximum streamfunctions ψ_{t} of the 2XSH and 2X experiments are approximately equal. However, ψ_{t} intensifies north of the equator. In the subtropical region (10N-30N), ψ_{t} increases with higher wind forcing, and the integrated transport of the 2X experiment is stronger than the integrated transport of the 2XSH experiment.

In contrast to ψ_{t}, the geostrophic maximum overturning streamfunction ψ_{g} is relatively weak near the Southern Ocean but constantly increases towards the equator. North of the Southern Ocean (30S-10S), ψ_{g} is increasingly dependent on the geostrophic return flow that compensates the southward surface Ekman flux locally. As a result of the interior return flow, ψ_{g} becomes stronger with higher wind forcing, with markedly higher values in the 2X experiment compared the 2XSH experiment. At the low and mid-latitudes of the northern hemisphere (10N-30N), the interior return flow of the surface Ekman flux is directed southward and strongest at roughly 15°N. At these

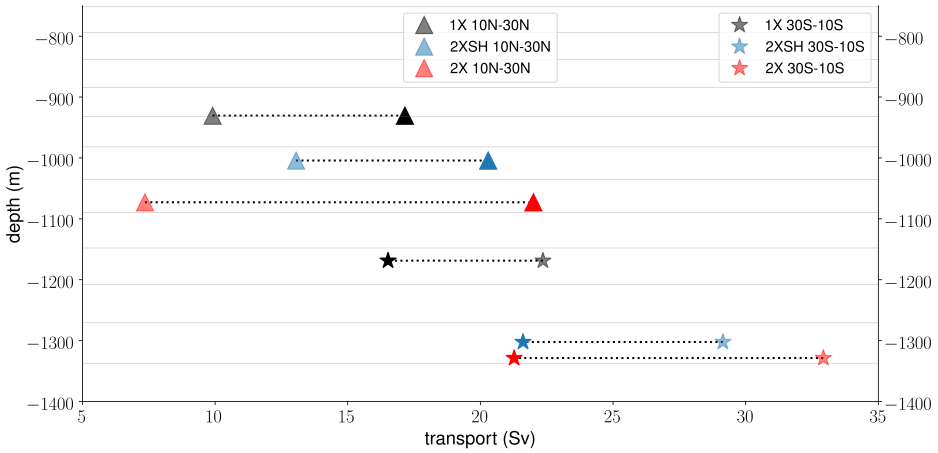

Figure 2.6: The time-mean (1991-2010) relationship between maximum overturning and its depth, the level of no motion, in the southern hemisphere and the northern hemisphere. The markers represent the meridional averages (30S-10S) (stars) and (10N-30N) (triangles). We show both the total maximum overturning streamfunction (ψ_{t}, opaque) and the geostrophic maximum overturning streamfunction (ψ_{g}, transparent). We do not show the pycnocline scale η_ρ because the qualitative behavior is same as the behavior of the level of no motion η_ψ except that the pycnocline scales of the 2XSH and 2X experiment are congruent throughout the basin. The thin grey lines indicate the vertical model grid.

latitudes, ψ_{g} of the 2X experiment is weaker than both the geostrophic transport of the 1X reference experiment and the 2XSH experiment. Comparing ψ_{t} and ψ_{g}, the Ekman cells play a crucial role in setting the relationship between overturning and its depth. We discuss the role of the Ekman cells and the possible explanations for the differences in maximum overturning besides the Ekman return flow later on, in section 4. First, we highlight the relationships between the maximum overturning streamfunctions and the depth scales in order to bring together their spatial dependencies.

Combining our findings from Fig. 4 and 5, we describe the relationship between northward overturning and its depth from a more nonlocal perspective on hemispheric differences. To highlight hemispheric differences in

the inter-hemispheric region, we show the meridional averages (30S-10S) and (10N-30N) (Fig. 6). In the southern hemisphere, the level of no motion η_ψ of the 2XSH and 2X experiment fall into the same model layer, and the associated maximum streamfunctions ψ_t are not notably different. In this region, ψ_g increases with higher wind forcing. South of the equator, the wind forcing dependencies of the level of no motion η_ψ as well as the pycnocline scale η_ρ (not shown) are in line with the wind forcing dependencies of ψ_t, in the sense that a broader depth scale is related to stronger northward overturning. Insights on the northern hemisphere are not as simple as in the southern hemisphere. The level of no motion η_ψ deepens with higher wind forcing due to the downward displacement of isopycnals at mid-depth, whereas η_ρ (not shown) reveals the same wind forcing dependencies as in its southern counterpart. The differences in the depth of the level of no motion η_ψ between the wind experiments are important although they are set by one model layer only, because even a small change in the model layers implies a change in the accumulation of vertical velocity shear, and the pycnocline scale η_ρ does not account for these details. As in the southern counterpart, the differences in the level of no motion η_ψ do not represent the changes in ψ_g, but the changes in ψ_t are consistent with the common assumption that the northward transport of the mid-depth cell becomes stronger with a deeper level of no motion η_ψ.

In general, the differences between ψ_t and ψ_g in the inter-hemispheric region suggest that the interior return flow of the surface Ekman flux is baroclinic and mostly compensated above the level of no motion η_ψ. If so, the level of no motion is a proxy for ψ_t rather than a proxy for ψ_g in the case that the vertical velocity shear stays approximately constant with wind forcing. This raises the questions how well the total and geostrophic maximum overturning streamfunctions represent interior flow despite the surface Ekman flux or its geostrophic return, and how well the level of no motion represents transport at different depths. In order to answer these questions, we analyze meridional velocity profiles ($\frac{\partial\psi}{\partial z}$) and shear ($\frac{\partial^2\psi}{\partial z^2}$).

2.4 The relationship between the depth scales and velocity profiles

The depth scales can be related to vertical velocity profiles ($\frac{\partial \psi}{\partial z}$) and shear ($\frac{\partial^2 \psi}{\partial z^2}$). To discuss changes in the velocity profiles with respect to the level of no motion and the pycnocline scale, we first compute the vertical derivative of the AMOC streamfunction $\frac{\partial \psi}{\partial z}$ (the zonal-mean meridional velocity scaled by the basin width). Neglecting the surface Ekman layer and integrating from the level of no motion η_ψ to the top gives the geostrophic approximation of the maximum overturning streamfunction that approximately represents the geostrophic conditions in the interior. Analyzing $\frac{\partial \psi}{\partial z}$ is a perspective on force balance, and we disentangle different contributions.

Fig. 7 shows the zonal-mean meridional velocities ($\frac{\partial \psi}{\partial z}$) in the wind experiments and the difference in $\frac{\partial \psi}{\partial z}$ between these wind experiments. The differences in $\frac{\partial \psi}{\partial z}$ between the wind experiments are strongest near the equator at the upper levels where the vertical velocity shear changes drastically. Taking the difference between the 2X and 1X experiments, we find an increase in $\frac{\partial \psi}{\partial z}$ south of the equator and a decrease north of the equator. To a substantial extent, these changes can be attributed to the strengthening of the local Ekman cells. The differences in $\frac{\partial \psi}{\partial z}$ at the upper levels between the different experiments demonstrate that the Ekman return flow is baroclinic and occurs mostly above η_ψ. The strong influence of the Ekman cells near the surface suggests that, at these levels, the external wind-driven flow associated with the Ekman cells superposes the internal flow that is associated with the level of no motion. These considerations support the perspective that η_ψ is a proxy for ψ_t rather than a proxy for ψ_g. Small differences in ψ_t emerge in case of weak compensation of the surface Ekman flux below η_ψ.

In Fig. 7 we further find differences in $\frac{\partial \psi}{\partial z}$ at mid-depth that are associated with the nonlocal wind forcing over the Southern Ocean. These changes can be inferred from the difference between the 2XSH and 1X experiments. The difference between these experiments is related to the enhanced inflow

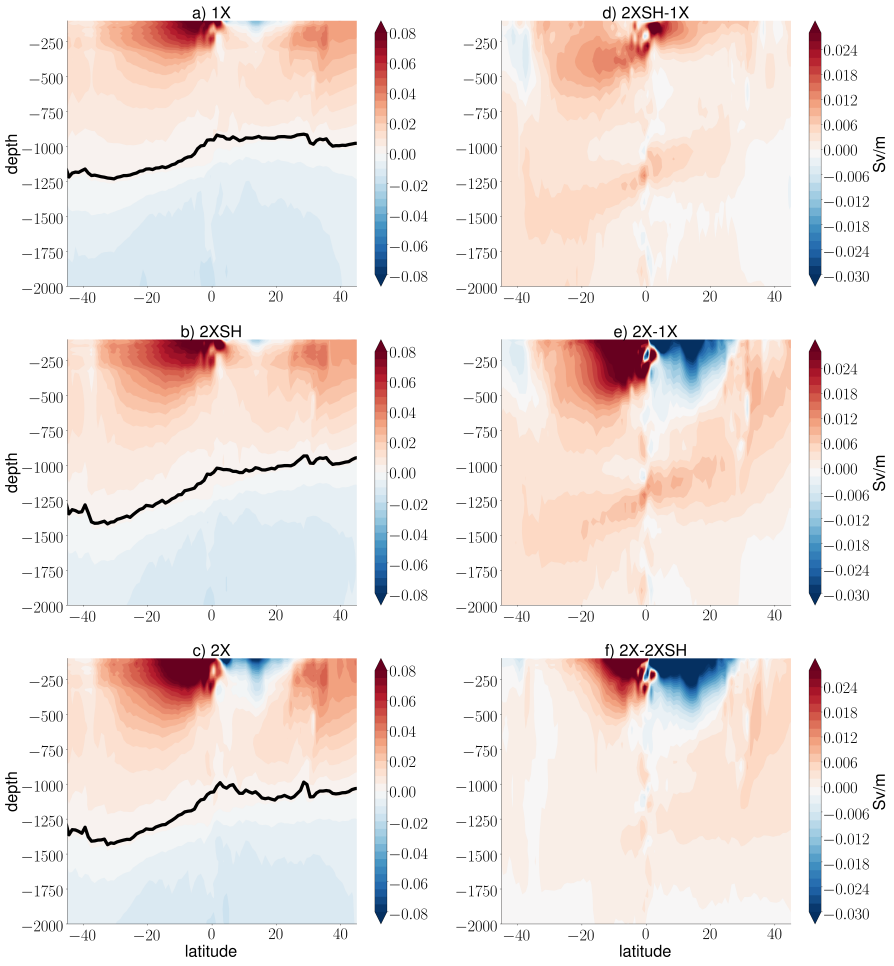

Figure 2.7: The time-mean (1991-2010) vertical derivative of the AMOC streamfunction $\frac{\partial \psi}{\partial z}$ in the (a) 1X experiment, (b) 2XSH experiment, and (c) 2X experiment. We further show the difference in $\frac{\partial \psi}{\partial z}$ between the (d) 2XSH and 1X experiments, (e) the 2X and 1X experiments, and (f) the 2X and 2XSH experiments. The black lines represent the level of no motion η_ψ. We exclude the surface Ekman layer.

from the southern hemisphere into the northern hemisphere, which in turn can be related to the strengthening of the western boundary current with an increase in wind forcing (not shown). In the 2X experiment, however, the perturbation associated with the Ekman cells is stronger than the perturbation associated with the strengthening of the western boundary current. The Ekman cells south and north of the equator further obscure the influence of the local Ekman pumping velocity W_{E} on stratification and transport at the advective depth η_{w}, which can be hardly identified in Fig. 7. The changes in the wind stress curl with changing wind forcing must be translated into the changes of the level of no motion η_ψ, and next we analyze explicitly how different depths of the level of no motion η_ψ result in different velocity profiles.

In this connection, we analyze whether there is a direct relationship between the vertical velocity profiles described by $\frac{\partial \psi}{\partial z}$ and the changes in the level of no motion η_ψ, by computing the meridional averages 30S-10S and 10N-30N (Fig. 8a,b). We analyze how much of the velocity profiles can be predicted by the level of no motion only. For this purpose, we assume vertical velocity shear that is constant under changing wind forcing. As indicated by the vertical bars, deep transport has a substantial contribution in both hemispheres because shear accumulates in the vertical over a wide depth range. In the southern hemisphere, the changes in the level of no motion η_ψ and the pycnocline scale η_ρ correspond to the changes in the actual velocity profiles $\frac{\partial \psi}{\partial z}$ (solid lines) at deeper levels. In the northern hemisphere downwelling region, the pycnocline scale does not change with local changes in wind forcing, whereas the level of no motion deepens locally. To assess to which degree the level of no motion η_ψ represents changes in the velocity profiles, we vertically integrate the time-mean vertical velocity shear $\frac{\partial^2 \psi}{\partial z^2}$ of the 1X reference experiment from the level of no motion η_ψ in the 2XSH and 2X experiments with zero reference velocity (dotted lines). This is not possible in the case of the pycnocline scale η_ρ, because it is a scale height and even a small layer difference in the reference depth results in differences in $\frac{\partial \psi}{\partial z}$. We find that the changes in deep velocity profiles are related to the changes in the level of no motion η_ψ in both hemispheres. To a considerable

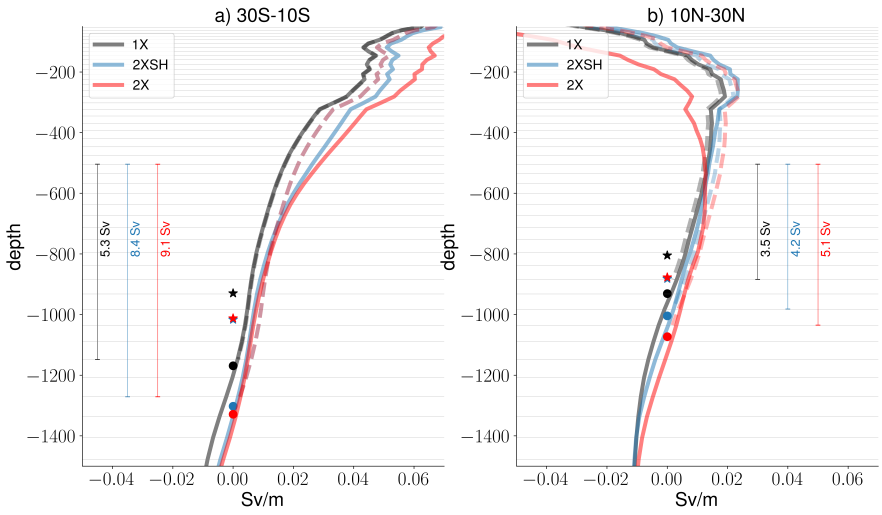

Figure 2.8: The meridional averages in the southern hemisphere (a, 30S-10S) and in the northern hemisphere (b, 10N-30N) of the time-mean (1991-2010) vertical derivative of the AMOC streamfunction $\frac{\partial \psi}{\partial z}$ in the 1X experiment (black), 2XSH experiment (blue), and 2X experiment (red). We exclude the surface Ekman layer. The circles show the meridional averages of the level of no motion η_ψ and the stars show the meridional averages of the pycnocline scale η_ρ. The dashed lines represent the velocity profiles that arise from the displacements of the level of no motion η_ψ while the velocity shear $\frac{\partial^2 \psi}{\partial z^2}$ is held constant (1X). Note that in the Southern hemisphere the blue dashed line and the red dashed line fall on top of one another. We indicate the transport (Sv) at the deeper levels by the annotation at the vertical bars. The thin grey lines indicate the vertical model grid.

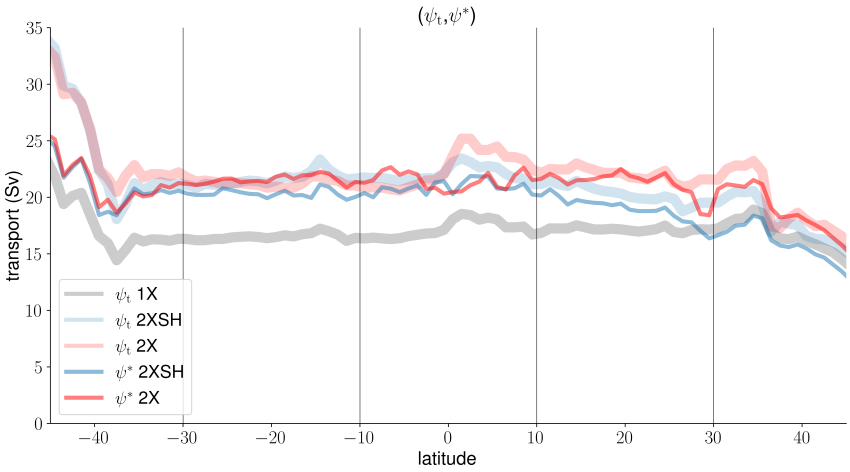

Figure 2.9: The total maximum overturning streamfunction ψ_t and the maximum overturning streamfunction ψ^* in the case that we hold the vertical velocity shear $\frac{\partial^2 \psi}{\partial z^2}$ constant (1X).

extent, even the velocity profile of the 2XSH experiment at the upper levels in both hemispheres is connected to the displacement of the level of no motion η_ψ. In the 2X experiment, however, the signal that arises from the interior return flow of the surface Ekman flux overcomes the signal that arises from the displacement of η_ψ. In the southern hemisphere at the upper levels, the velocities associated with the changes of the level of no motion η_ψ are lower than the actual velocities in this experiment. In the northern hemisphere at the upper levels, the velocities associated with the changes of the level of no motion η_ψ are much higher than the actual velocities. Integrating the velocity profiles vertically, however, the Ekman cells should cancel out such that the level of no motion is a proxy for northward transport.

We therefore show the changes in maximum overturning that are associated with the level of no motion only by analyzing the vertically integrated transport. Fig. 9 shows the total maximum overturning streamfunction ψ_t and the maximum overturning streamfunction ψ^* in the case that we hold the vertical velocity shear constant. We find that the changes in total maximum overturning ψ_t are explained by the changes in the level of no motion

to a very large degree. The maximum overturning streamfunctions ψ_{t} and ψ^* are approximately congruent, and the vertical velocity shear $\frac{\partial^2\psi}{\partial z^2}$ stays approximately constant with wind forcing on the timescale considered here. There is deviation at the equator due to systematic errors that arise from perturbations in equatorial upwelling. Away from the equator, however, the differences between the 2XSH and 2X experiments arise solely from the differences in the level of no motion. The mechanism how the changes in wind forcing translate into changes in the level of no motion η_ψ is thus easy to comprehend from a generic point of view. Small changes in the zonal pressure gradients at the depth range scaled by advective depth scale η_{w} are related to substantial differences in the level of no motion η_ψ, because the internal velocity shear that is not influenced by the external Ekman cells hardly changes between the wind experiments.

2.5 Discussion

In line with the current understanding of the Atlantic circulation, Southern Ocean winds boost the strength of the AMOC and change density stratification throughout the basin (e.g. Vallis, 2000; Klinger et al., 2003, 2004; Klinger and Cruz, 2009). Northern hemisphere winds over the downwelling region additionally influence the meridional flow and density stratification locally, which is commonly ignored in the scientific literature on the AMOC. The present study is based on simulations with an eddy-resolving OGCM on a decadal timescale rather than a fully equilibrated experiment. We find a robust adjustment of the AMOC and density field, which demonstrates the realization of major adjustments due to wave propagation, and the 30-year simulations are long enough to analyze the wind forcing dependencies of the depth scales and northward transport. The wind forcing-dependence of the AMOC is reflected by the wind experiments.

The findings of the present study support the pycnocline model described in Gnanadesikan (1999) in the sense that Southern Ocean wind forcing deepens the pycnocline scale and the level of no motion and strengthens the

AMOC. However, local wind forcing over the northern hemisphere downwelling region additionally influences the level of no motion and northward transport locally. In that respect, the level of no motion is more appropriate to scale northward transport than the pycnocline scale. By artificial modification of density gradients in OGCM experiments, Griesel and Maqueda (2006) and DeBoer et al. (2010) indicate that the pycnocline scale does not scale northward transport at all. By contrast, we provide insight on the scaling behavior of the depth scales from a conceptual point of view, and the pycnocline scale fails to scale northward transport in the northern hemisphere.

Wind stress curl variations at the surface translate into changes in the AMOC. The changes of the AMOC with changing wind forcing in the interhemispheric region are explained by the changes in the level of no motion. The internal velocity shear that is not influenced by the external Ekman cells remains constant on the timescale considered here. In contrast to what is stated in Cabanes et al. (2008) who analyze interannual variability, the forcing imposed by the wind stress curl at the surface does not substantially change the vertical shear but the reference depth of the AMOC shear component. Our findings also deviate from Levermann and Fuerst (2010) who evaluate the pycnocline model using a model of intermediate complexity. They analyze equilibrated experiments which reproduce the response to Southern Ocean wind forcing and focus on meridional density gradients instead of zonal density gradients to represent vertical velocity shear. Using meridional density gradients instead of zonal density gradients is based on the assumption that these gradients are proportional and have the same order of magnitude, and zonal and meridional velocities compare well with one another. According to their findings, both the pycnocline scale and meridional density gradients vary, while according to our study the internal velocity shear remains fixed. We speculate that our high-resolution simulation better simulates velocity shear.

The displacement of the level of no motion in the MPIOM wind exper-

iments approximates the conditions in the interior with the Ekman cells mainly cancelled out. Comparing the wind experiments, the ocean response at the upper levels is much more complex than the response at the deeper levels, which is mostly related to the baroclincity of the interior return flow of the surface Ekman flux. However, integrating vertically, the changes that are associated with the level of no motion give approximately the changes in the total maximum overturning streamfunction with changing wind forcing. As a general contribution and supporting the theoretical considerations made in McCreary and Lu (1994), our findings give baroclinic Ekman compensation which has been demonstrated in an idealized way by Williams and Roussenov (2014). Baroclinic Ekman compensation may depend sensitively on the resolution of an OGCM.

The wind forcing dependence of the AMOC suggests that the temporal adjustment of the AMOC to global warming is not independent of location. Both nonlocal Sothern Ocean wind forcing and local wind forcing in the northern hemisphere downwelling region are likely to influence the adjustment of the level of no motion and northward transport in the inter-hemispheric region.

2.6 Summary and Conclusions

We use wind sensitivity experiments to analyze the wind forcing dependence of depth scales of the inter-hemispheric cell in the Atlantic and their relationship to northward transport. We focus on the inter-hemispheric region in order to analyze the interplay of nonlocal and local wind effects, and our perspective deviates from the common view that the AMOC is a nonlocal phenomenon only. The dynamics of the inter-hemispheric cell can only be understood by analyzing both Southern Ocean wind effects and local wind effects in the northern hemisphere downwelling region which arises from the forcing imposed by the wind stress curl at the surface.

We find different wind forcing dependencies of the pycnocline scale and

the level of no motion. Southern Ocean processes determine the magnitude of the pycnocline scale, whereas northern hemisphere wind stress additionally influences the level of no motion. The pycnocline scale is insensitive to the local wind stress over the northern hemisphere and cannot capture the details of deep velocity profiles and mid-depth stratification. Local wind forcing changes density stratification and displaces isopycnals downward at an advective depth. In that respect, the level of no motion is a better proxy for velocity profiles than the pycnocline scale, because the level of no motion accounts for the changes in the surface winds over the northern hemisphere.

To a large extent, the changes in transport at deeper levels below the surface layers between the wind experiments can be related to the changes of the level of no motion in the case that we hold the vertical velocity shear of the meridional velocity constant. The changes in the level of no motion between the wind experiments explain a large fraction of the changes in the meridional velocities. Near the surface, however, the signal that arises from the interior return flow of the surface Ekman flux overcomes the signal that arises from the displacement of the level of no motion. In this regard, the changes in the meridional flow which are associated with the displacement of the level of no motion and the actual transport can differ considerably at these levels. However, the changes in maximum overturning with changing wind forcing are explained by the changes in the level of no motion only, because the internal velocity shear that is not influenced by the external Ekman cells stays constant.

There is no unique way to describe and quantify interior geostrophic flow that is not directly influenced by the local Ekman cells, and in this sense both the total maximum overturning streamfunction and the geostrophic maximum overturning streamfunction are approximations for the conditions in the interior. Our findings suggest that the differences in the total maximum overturning streamfunction are related to the differences in the level of no motion, since the surface Ekman fluxes are compensated mostly above the level of no motion. Compared to the total maximum overturning stream-

function, the geostrophic approximation makes a scaling more complex, but it is the result of the force balance below the surface Ekman layer. The hemispheric differences in the level of no motion and the associated meridional transport suggest a hemispheric scaling rather than a single depth scale approximation for the entire basin.

The present manuscript relies on experiments that are conducted with a single but horizontally high-resolution model. Low-resolution models may differ significantly from high-resolution models. We put forward the idea that the ability of numerical models to capture the spatial and temporal variations of the level of no motion is crucial to reproduce the mid-depth cell in an appropriate way. Changes in the relationships between the level of no motion and vertical velocity shear change the AMOC both quantitatively and dynamically.

Chapter 3

Outlook

3.1 Introduction

The results of my publication are novel. A disadvantage is that these results are based on a single model study only, which reveals the need for a model intercomparison. To have a firm ground, this model intercomparison should be about the influence of local Ekman pumping on the AMOC and the level of no motion as a proxy for internal transport as defined previously. It is likely that only high-resolution models can simulate this appropriately, since they better simulate the relation between meridional velocities, velocity shear, and the level of no motion. I have also analyzed the time-dependence of the 1980-2010 TP6ML80 wind sensitivity experiments. The time-mean 1991-2010 wind forcing dependence does reflect the quasi-steady wind forcing dependence of the AMOC despite oscillations at low frequency (not shown). As a subsequent topic, I suggest to study the adjustment of the AMOC to global warming. Mainly, I propose to analyze how local Ekman pumping in the northern hemisphere translates into the AMOC perturbation as well as to realize idealized global warming experiments in which wind patterns are prescribed. The latter makes it possible to analyze the relative influence of the Southern Ocean Ekman pumping and northern hemisphere Ekman pumping on the AMOC in abrupt CO_2 experiments with numerical ocean models. To generate a solid basis for further proceedings, in this outlook I

first compare the results inferred from the wind experiments and a 100-year global warming experiment in which the atmospheric CO2 concentration is abruptly quadrupled. Secondly, I develop associated research questions.

Like the different wind experiments, the warming experiment (4XCO2) is conducted with a horizontally high-resolution configuration of MPIOM (Putrasahan et al., 2020). The version is called TP6ML40 and it is coupled to the atmospheric model ECHAM6. The coupled model is described in Gutjahr et al. (2019) and initialized with the state of the control simulation which mimics observed conditions at year 1950. In contrast to TP6ML80, the ocean model has only 40 unevenly spaced levels because we have a 100-year simulation and ease the computational burden. The coupled model is integrated from year 1980 to year 2079. Later on, I compare the high-resolution model output and the abrupt 4XCO2 experiment with the low-resolution climate model MPI-ESM1.2. It is conducted with a horizontally low-resolution configuration of MPIOM. The version is called GR15L40 and has a horizontal resolution of 1.5 degrees and 40 vertical layers. Likewise the high-resolution model configuration, it is coupled to the atmospheric model ECHAM6.

3.2 Global warming

I compare the insights on the wind experiments and the outcome of a warming experiment in which we quadruple the preindustrial CO_2 concentration. First, I characterize the evolution of the zonal-mean density stratification and the pycnocline scale η_ρ (Fig. 3.1a) as well as the evolution of the zonal-mean meridional velocities $\frac{\partial \psi}{\partial z}$ and the level of no motion η_ψ (Fig. 3.1b). Afterwards, I use meridional averages of the first and second vertical derivatives of the AMOC streamfunction $\frac{\partial \psi}{\partial z}$ and $\frac{\partial^2 \psi}{\partial z^2}$ in order to analyze explicitly the relationship between northward transport and its depth (Fig 3.1).

In a similar manner to the wind experiments, I normalize the zonal-mean potential density to highlight the changes in stratification, $\frac{\rho_0 - \rho}{\rho_0}$, with the

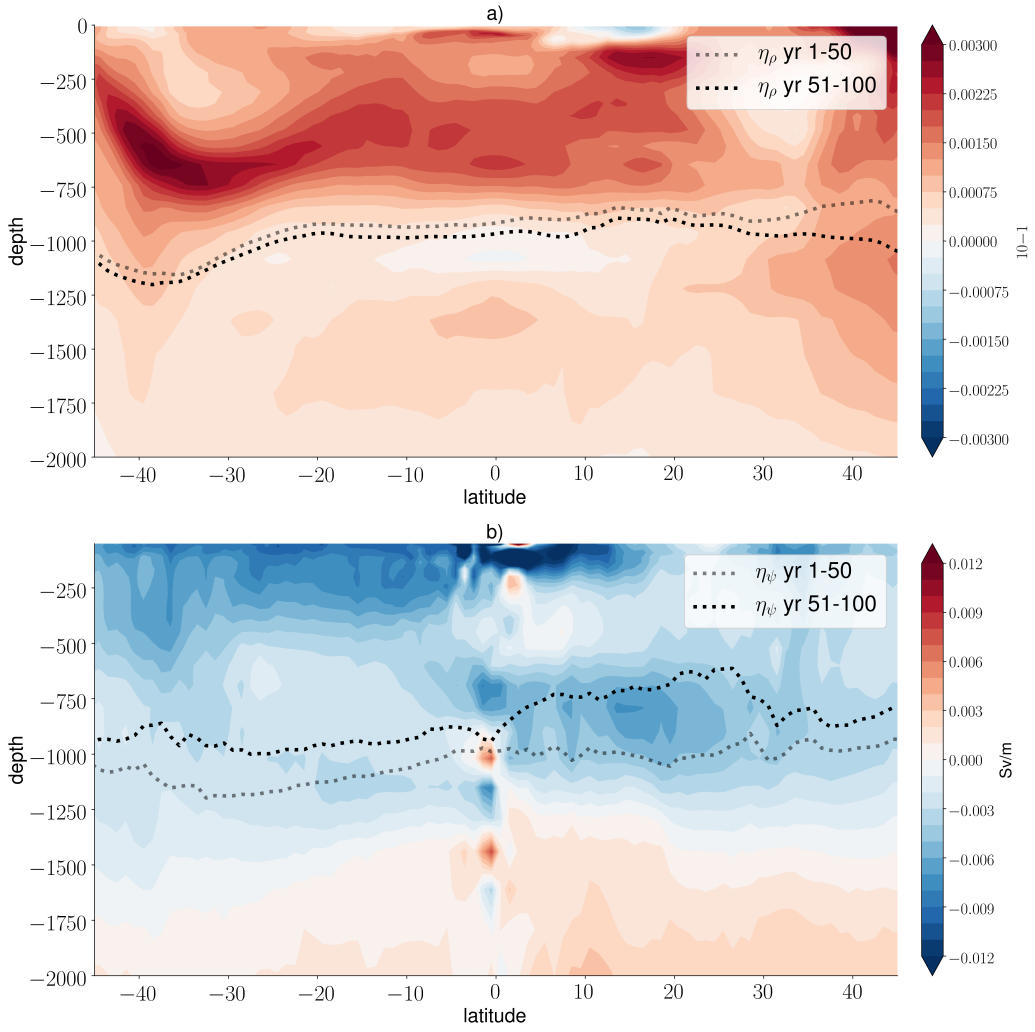

Figure 3.1: The difference in (a) the zonal-mean density stratification and (b) the vertical derivative of the AMOC streamfunction $\frac{\partial \psi}{\partial z}$ between years 51-100 and 1-50 in the 4XCO2 experiment. Density stratification is computed by $\frac{\rho_0 - \rho}{\rho_0}$, with the reference density $\rho_0 = 1025$ kg m^{-3}. The lines in (a) indicate the pycnocline scale η_ρ and the lines in (b) indicate the level of no motion η_ψ.

reference density $\rho_0 = 1025$ kg m^{-3}. We are interested in the changes of the depth scales η_ψ and η_ρ and their relationship to northward transport on a decadal timescale and do not consider the deviations from the model control state. To illustrate the temporal changes in density stratification, we first take the difference between 50-year multi-decadal means that split the 100-year model time series. Fig. 3.1a shows that density stratification changes throughout the mid-depth cell. I find the maximum change in density at an advective depth scale η_w at the southern latitudes of the southern hemisphere, which indicates that wind forcing strongly influences ocean heat uptake in the Atlantic. The spatial distribution of heat uptake compensates for spatial variations of the pycnocline scale η_ρ. Heat diffuses downward even far below the level of no motion and is redistributed by the overturning circulation. As a result, the pycnocline scale η_ρ broadens or deepens. In contrast to the pycnocline scale η_ρ, the level of no motion η_ψ of the mid-depth cell shoals, and the meridional velocities $\frac{\partial \psi}{\partial z}$ of the upper branch of the mid-depth cell decrease (Fig. 3.1b). As in the case of the pycnocline scale, the spatial variations of η_ψ are less strong than the spatial variations in the different wind experiments, but they are still important considering the temporal adjustment. Furthermore, the decline in the magnitude of $\frac{\partial \psi}{\partial z}$ is evenly distributed in the latitude-depth section near or above η_ψ, which suggests that the displacement of the level of no motion changes the region over which vertical shear is accumulated. It is supported by the fact that we find a decrease in the zonal-mean meridional velocities ($\frac{\partial^2 \psi}{\partial z^2}$) even below η_ψ. Moving to deeper layers of the southward flowing branch indicates the adjustment or weakening of the overturning circulation.

In terms of a direct relationship, the pycnocline scale cannot scale northward transport on the decadal timescale considered here, because it deepens after an initial adjustment. By contrast, the pycnocline scale may be a time-dependent predictor for future long-term overturning in response to global warming because it adjusts due to advective-diffusive balance. The global warming experiment shows that changes in the the level of no motion over time represent changes in northward transport in the upper branch of the

mid-depth cell. Although the sign of the changes is equal in both hemispheres, we find hemispheric differences in the shoaling of the level of no motion and transport weakening. Ekman pumping in the northern hemisphere downwelling region may be key, which calls for the development of specific research questions.

3.3 Research questions

The translation of the surface wind forcing into the adjustment of the AMOC to global warming may depend on model resolution. For instance, eddy-resolving models may differ from low-resolution counterparts in the way how they simulate the changes in potential temperature and salinity. Potential temperature and salinity in the inter-hemispheric region depend on Southern Ocean wind forcing. At the same time, local wind forcing over the northern hemisphere downwelling region changes potential temperature and salinity locally. Levang and Schmitt (2019) address the northern hemisphere weakening of the AMOC in global warming simulations and analyze temperature-induced and salinity-induced changes in the shear component of the meridional flow. The anomalies in density cause a weakening of the AMOC because the geostrophic shear component of the AMOC is altered. The anomalies in temperature and salinity are advected from the surface to deeper levels due to the forcing imposed by the wind stress curl at the surface over the downwelling region. In general, their findings are in line with the finding that local Ekman pumping influences the mid-depth cell in a substantial way. However, the interplay of Southern Ocean wind forcing and wind forcing over the northern hemisphere downwelling region may be very specific among OGCMs. For illustration, in Fig. 3.2 we compare the eddy-resolving model configuration and the low-resolution counterpart using a quadrupling of the atmospheric CO_2 concentration. At the range of the advective depth scale in the northern hemisphere downwelling region, zonal-mean potential temperature and salinity are more diffusely distributed in the high-resolution model simulation than in the low-resolution model simulation. How these differences in salinity and wind forcing translate into

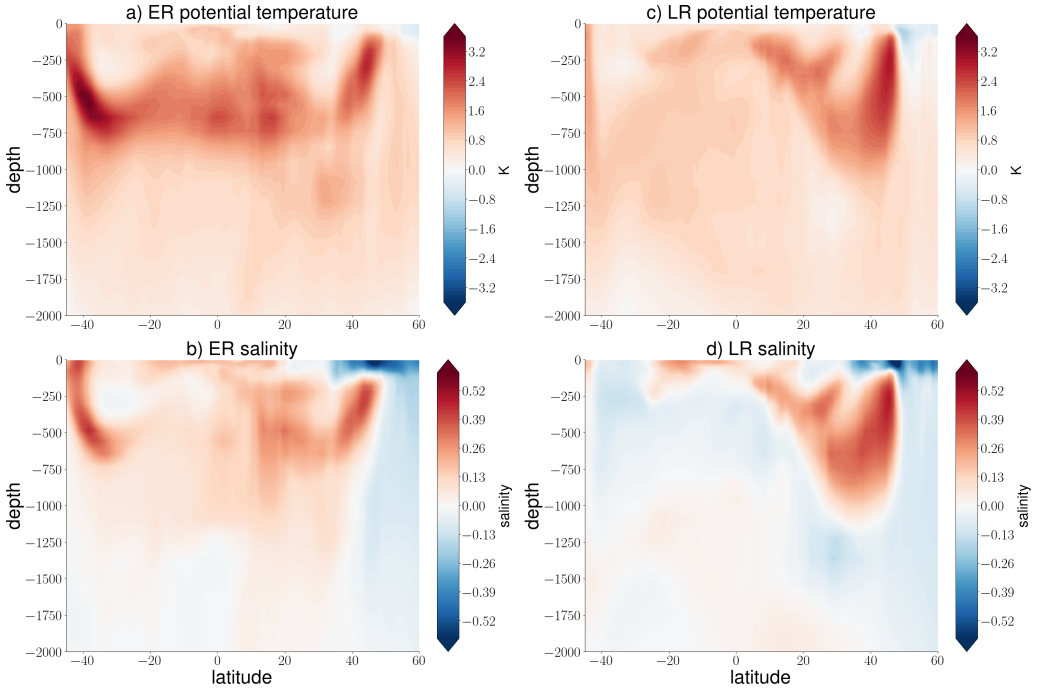

Figure 3.2: The difference in (a,c) zonal-mean potential temperature and (b,d) salinity between years 51-100 and 1-50 in the 4XCO2 experiments with the eddy-resolving model configuration (ER) and the low-resolution model configuration (LR).

the AMOC, or how wind forcing in general translates into the AMOC, is a major source of uncertainty. I speculate that it is not the wind stress curl that gives rise to model spread in the AMOC adjustment to global warming among coupled climate models. As outlined in this section, I presume that it is the translation of the surface wind forcing that gives rise to model spread.

Global warming experiments with changing surface winds are necessary to find out how strong the adjustment of the AMOC to global warming depends on Southern Ocean winds and local Ekman pumping in the northern hemisphere. Considering the influence of these regions, the relative contribution of Southern Ocean winds and local Ekman pumping in the northern hemisphere may depend on the strength on the wind forcing itself. These regions may compete, since Southern Ocean winds push cold and low saline waters

into the inter-hemispheric region while warm and saline waters are advected from the surface to greater depths in the northern hemisphere downwelling region. The effect of Southern Ocean winds may become more important in the case of high-forcing input such as doubling of the surface wind stress. In that case, the effect of local Ekman pumping in the northern hemisphere may not overcome the effect of Southern Ocean winds locally. By contrast, the effect of northern hemisphere winds may be more important under observed boundary conditions. Finally, in such global warming experiments in which winds are artificially modified the timescales of the AMOC adjustment to global warming likely depend in a sensitive way on the forcing which is imposed by the surface winds. Southern Ocean winds and and northern hemisphere winds may change these timescales differently. In general, the AMOC may recover earlier or later in time depending on the strength of the wind forcing.

3.4 Experiment illustration

In the following I would like to illustrate the global warming experiments with altered surface wind stress. These warming experiments are designed to explore the AMOC adjustment to global warming that depends on the strength of the wind forcing or Ekman pumping. I do not present a thorough analysis but a major insight from these experiments. The warming experiments with altered surface wind stress are conducted with MPI-ESM1.2-LR, and they are initialized with control experiments in which the surface wind stress is likewise altered. The global warming experiments have an integration time of 120 years (1850-1969), and the atmospheric CO_2 concentration is quadrupled (4X). After having explored that initialization plays only a minor role, I initialize consistently after 30 years integration time. I have a set of four experiments: the 2X experiment in which the zonal and meridional surface wind stress is doubled throughout the hemispheres; the 2XSH experiment in which the wind stress is doubled over the Southern Ocean only; the 1X experiment which is forced under no changes; and the 0.5X experiment in which the zonal and meridional wind stress is halved. I only change the ocean

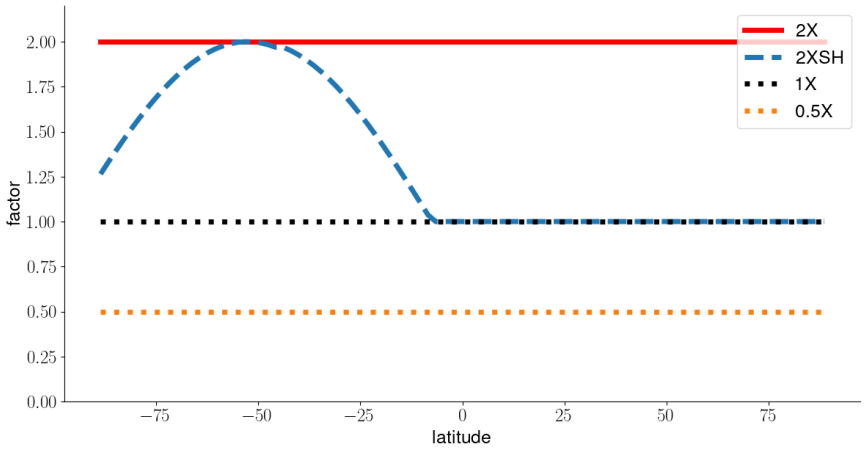

Figure 3.3: The ocean wind stress factor that multiplies the surface wind stress τ in the coupled model that is used for the idealized global warming experiments; $\tau_{\text{om}} = \tau \times factor$

wind stress factor that multiplies the surface wind stress in the coupled model because I am interested in the OGCM dynamics only. Fig. 3.3 shows the ocean wind stress factor of the different experiments. The global warming experiments with altered surface wind stress also confirm the wind forcing dependence of the AMOC as found in the first paper of the dissertation (not shown). As expected, a strongly forced system gives insight into the underlying dynamics. Fig. 3.4 shows the evolution of the vertical derivative of the AMOC streamfunction relative to the initial state. Comparing the different panels, Southern Ocean Ekman pumping and northern hemisphere Ekman pumping compete as forcing in terms of the inter-hemispheric circulation. It becomes evident that the AMOC adjustment to global warming depends on northern hemisphere Ekman pumping in a sensitive way.

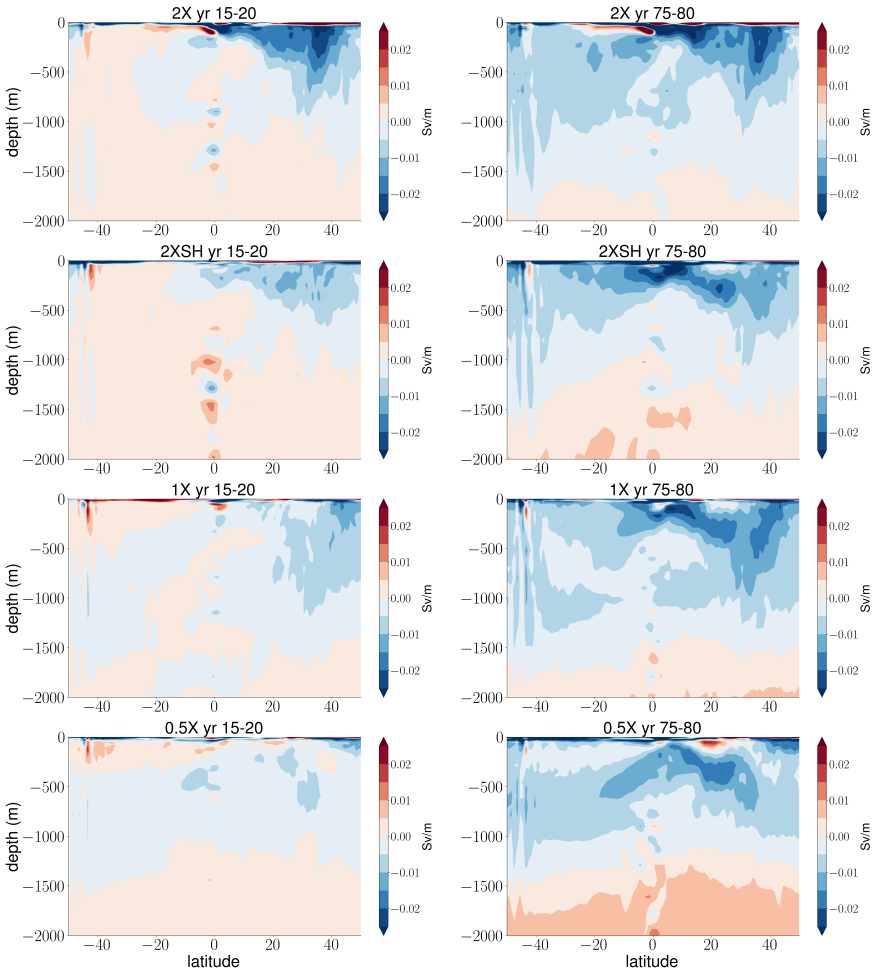

Figure 3.4: The evolution of the vertical derivative of the AMOC streamfunction $\frac{\partial \psi}{\partial z}$ (yr 15-20 and yr 75-80) relative to the initial state (yr 1-5) in the warming idealized experiments.

Part II

A different view on the timing of climate change

Chapter 4

Publication

Bibliographic Information

Rohrschneider, T., Bloch-Johnson, J. and M. Rugenstein (2021): Does feedback temperature dependence influence the slow mode of the climate response? Submitted to Earth System Dynamics.

Author contribution

TR lead the research, developed the coding scripts, and wrote the present manuscript. JBJ and MR reviewed and commented on the manuscript and its content.

Abstract

Atmosphere-Ocean General Circulation models (AOGCMs) are a necessary tool to understand climate dynamics on centennial timescales for which observations are scarce. We explore to which degree the temperature dependence of the climate radiative feedback influences the slow mode of the surface temperature response. We question whether long-term climate change is described by a single e-folding mode with a constant timescale which is commonly assumed to be independent of temperature or forcing and the evolution

of time. To do so, we analyze AOGCM simulations which have an integration time of 1000 years and are forced by atmospheric CO_2 concentrations ranging from 2 times (2X) to 8 times (8X) the preindustrial level. Our findings suggest that feedback temperature dependence strongly influences the equilibrium temperature response and adjustment timescale of the slow mode. The magnitude and timescale of the slow mode is approximately reproduced by a zero-dimensional energy balance model that has a constant effective heat capacity and incorporates a background feedback parameter and a coefficient for feedback temperature dependence. However, the effective heat capacity of the slow mode increases over time, which makes the adjustment timescale also time-dependent. The time-varying adjustment timescale can be approximated by a multiple timescale structure of the slow temperature response, or vice versa, a multiple timescale structure of the slow temperature response is described by a time-dependent timescale. The state-dependence and time-dependence of the adjustment timescale of long-term climate change puts into question common eigenmode decomposition with a fast and a slow timescale in the sense that the slow mode is not well described by a single linear e-folding mode with a constant timescale. We find that such an eigenmode decomposition is valid at a certain forcing level only, and an additional mode or a multiple mode and timescale structure of the slow adjustment is necessary to reproduce the details of AOGCM simulated long-term climate change.

Editing note

Equations and figures are labeled numerically by the indices $i.j$. Following the publication, we refer to these equations and figures by referring to the second index j. Sections are labeled numerically by the indices $i.j.k$. Following the publication, we refer to these sections by referring to the second and third indices $j.k$.

4.1 Introduction

Long-term climate change is determined by the slow mode of the surface temperature response. We analyze the slow mode in light of temperature-dependent radiative feedback and time-varying adjustment timescales using abrupt CO_2 experiments with Atmosphere-Ocean General Circulation models (AOGCMs). The slow mode approximately describes the temporal temperature adjustment in response to radiative forcing on a multi-centennial timescale. In this study feedback temperature dependence describes how the radiative feedback of the climate system depends on the global mean surface temperature change. As a result, higher forcing will cause a greater change in feedback, as it will cause a greater increase in temperature. Our study is motivated scientifically by understanding and predicting long-term climate change beyond year 2100.

Using proxies or complex climate models, studies on paleo climates demonstrate that the climate feedback depends on the climate state (e.g. Kutzbach et al., 2013; Schaffer et al., 2016; Wolf et al., 2018; Farnsworth et al., 2019). Recent research on modern-day boundary conditions demonstrates that feedback temperature dependence of the global feedback becomes important in the case of high forcing (e.g. Roe and Baker, 2007; Roe and Armour, 2011; Meraner et al., 2013; Bloch-Johnson et al., 2015; Rohrschneider et al., 2019). The latter studies are based on Charney-type feedbacks (Charney et al., 1979) and mostly focus on the equilibrium surface temperature change in response to forcing input such as a quadrupling of the atmospheric CO_2 concentration above preindustrial levels. The equilibrium temperature change in response to radiative perturbations can be described by a zero-dimensional energy balance model that incorporates a parameter for temperature-dependent feedback (Zaliapin and Ghil, 2010; Bloch-Johnson et al., 2015). The zero-dimensional model describes the relationship between the global mean radiative forcing input F and global mean equilibrium surface temperature

perturbation $T(\infty)$,

$$-F = (\lambda_\mathrm{b} + aT(\infty))T(\infty), \tag{4.1}$$

where λ_b is the initial or background feedback parameter and a is the coefficient for feedback temperature dependence. According to this framework, the equilibrium temperature response $T(\infty)$ depends nonlinearly on the radiative forcing F. By contrast, it scales linearly with forcing in the case of zero feedback temperature dependence. Furthermore, feedback temperature dependence does not only influence the equilibrium temperature change but also the temporal behavior of the temperature adjustment. The temporal adjustment of this zero-dimensional energy balance model is described by

$$C\frac{\mathrm{d}T}{\mathrm{d}t} = N \text{ or } C\frac{\mathrm{d}T}{\mathrm{d}t} = F + (\lambda_\mathrm{b} + aT)T, \tag{4.2}$$

where N is the net top-of-the-atmosphere (TOA) radiative imbalance compared to steady state, and C is the effective heat capacity of the global system. The latter is an effective quantity because it depends on the ocean circulation and does not directly represent the ocean mass. Integrating analytically the right-hand side of Eq. (2) gives a timescale that depends on the strength of the forcing because the feedback changes with warming. The state-dependence of the temporal adjustment of the climate response has been demonstrated conceptually and with simulations of a single AOGCM (Rohrschneider et al., 2019).

The global mean surface temperature response of the climate system is approximately described by a fast mode that acts on a decadal timescale and a slow mode that acts on a multi-centennial timescale. In general, the two-timescale approach has been found a good approximation for complex model behavior (e.g. Held et al., 2010; Winton et al., 2010; Geoffroy et al., 2013a,b; Rohrschneider et al., 2019). Recent studies suggest that the slow mode is either a function of the Earth's deep ocean component (e.g. Held et al., 2010; Winton et al., 2010; Geoffroy et al., 2013a,b), or associated with

a radiative feedback (e.g. Armour et al., 2013; Proistosescu and Huybers, 2017). Mathematically, these concepts are equivalent (Rohrschneider et al., 2019). Commonly, the concept of a fast mode and a slow mode is based on eigenmode decomposition. Using linear eigenmode decompostion, the temperature evolution $T(t)$ over time is approximated by multiple exponential modes (n),

$$T(t) = \sum T_n(\infty)(1 - e^{-t/\tau_n}), \tag{4.3}$$

with $T_n(\infty)$ the amplitude, and τ_n the e-folding timescale. The question arises whether the two-timescale approach with a slow e-folding mode and a constant timescale is still an appropriate description of long-term climate change. According to theory, feedback temperature dependence makes the adjustment timescale continuous and makes it depend on the forcing. Furthermore, the thermal inertia of the slow mode, mathematically described by the effective heat capacity, can change over time or with climate state such that the influence of feedback temperature dependence on the temporal adjustment is modified. For instance, the ocean circulation may change and the heat flux into the deep ocean may become less efficient (Rugenstein et al., 2016b), which would cause C to increase.

It is important to know the mode and timescale structure of the temperature response in order to make accurate predictions and understand the temporal temperature adjustment at different timescales even without having an underlying physical model. It is debated how many adjustment modes exist and are necessary to reproduce the complex system response (Olivie et al., 2012; Caldeira and Myhrvold, 2013; Knutti and Rugenstein, 2015; Proistosescu and Huybers, 2017). We question whether the slow mode is a single eigenmode with a single constant timescale in the common sense. The timescale is commonly assumed to be independent of temperature or forcing and the evolution of time.

We use abrupt CO_2 experiments with multiple AOGCMs in order to answer this research question. Using multiple AOGCMs with different radiative

responses and atmospheric and oceanic parameterizations allows us to assess whether the influence of feedback temperature dependence on long-term climate change is substantial. The AOGCM experiments used here are the only publicly available experiments to date that have an integration time of at least 1000 years and provide three different forcing levels (Rugenstein et al., 2019). Thus, we can explore the changes in the slow adjustment with forcing and analyze long-term climate change on a multi-centennial timescale. We compare the low-end and high-end forcing range considered in CMIP6 scenarios (O'Neill et al., 2016) to have a large signal; that is, two times (2X) and eight times (8X) the preindustrial CO_2. The CO_2 concentration is held constant throughout the simulation time so that we can explore the underlying dynamics. In mathematical terms, the radiative forcing is a step function input.

Section 2 provides conceptual insights on the slow mode. Section 3 outlines the experimental strategy and characterizes the AOGCM properties in simulating the climate response. In section 4, we analyze the equilibrium response and timescale of the slow mode in light of temperature-dependent feedback. In section 5, we analyze the interplay between state-varying and time-varying adjustment timescales and demonstrate the limits of eigenmode decomposition in terms of the two-timescale approach.

4.2 Conceptual insights

Before exploring the slow mode's behavior in AOGCMs, we provide conceptual insights about the slow mode using simple climate models. These simple models are energy balance models and outlined in detail in Geoffroy et al. (2013a), Geoffroy et al. (2013b), Armour et al. (2013), Rohrschneider et al. (2019), among others. We bring together these existing concepts to lay out the parameter dependencies of the slow mode in order to provide a solid basis and motivation for our experimental analysis.

A way to represent the global mean surface temperature response to forc-

ing is to assume two effective regions, $T = (\chi - 1)T_{\mathrm{F}} + \chi T_{\mathrm{S}}$, where χ is the effective fractional area:

$$C_{\mathrm{F}} \frac{\mathrm{d}T_{\mathrm{F}}}{\mathrm{d}t} = F + (\lambda_{\mathrm{F}} + a_{\mathrm{F}} T_{\mathrm{F}}) T_{\mathrm{F}}. \tag{4.4}$$

and

$$C_{\mathrm{S}} \frac{\mathrm{d}T_{\mathrm{S}}}{\mathrm{d}t} = F + (\lambda_{\mathrm{S}} + a_{\mathrm{S}} T_{\mathrm{S}}) T_{\mathrm{S}}. \tag{4.5}$$

F is the radiative forcing, C is the constant effective heat capacity, λ is the background feedback parameter, a is the coefficient for feedback temperature dependence. Each region behaves similarly to Eq. (2), and according to this framework, the climate response is characterized by a fast mode T_{F} and a slow mode T_{S}. In this paper, we analyze the influence of feedback temperature dependence on the slow mode only. Positive feedback temperature dependence causes the equilibrium response of the slow mode to increase. Furthermore, feedback temperature dependence introduces a timescale that depends on the strength of the forcing. Considering the temporal behavior, the thermal inertia of the slow mode is represented by a single heat capacity which is much higher than the heat capacity of the fast mode ($C_{\mathrm{F}} \ll C_{\mathrm{S}}$). At this point, C_{S} is constant over time and does not change with the climate state. The slow mode of the surface response is thought to be coupled to the state of the deep ocean or being an effective region.

Another conceptual framework with a fast mode T_{F} and a slow mode T_{S} is the two-layer ocean model with ocean heat uptake efficacy and feedback temperature dependence (Held et al., 2010; Winton et al., 2010). This model combines time-dependent feedback due to the evolution of two different state-variables and state-dependent feedback due to temperature-dependent feedback. The model configuration with ocean heat uptake efficacy and feedback temperature dependence is given by

$$C \frac{\mathrm{d}T}{\mathrm{d}t} = F + (\lambda_{\mathrm{b}} + aT)T - \epsilon\eta(T - T_{\mathrm{D}}) \tag{4.6}$$

$$C_{\mathrm{D}}\frac{\mathrm{d}T_{\mathrm{D}}}{\mathrm{d}t} = \eta(T - T_{\mathrm{D}}) \tag{4.7}$$

where $C \ll C_{\mathrm{D}}$ are the heat capacities of the upper- and deep-ocean, λ_{b} is the background feedback parameter and a the coefficient for feedback temperature dependence. The parameter η is the heat transport efficiency and ϵ the efficacy factor for ocean heat uptake. The slow component is approximated by

$$T_{\mathrm{s}}(t) \approx \frac{\sqrt{\Lambda^2 - 4aF} - \sqrt{\Lambda^2 - 4aF - 4a\epsilon\eta T_{\mathrm{D}}(t)}}{2a} \text{ with } \Lambda = \lambda_{\mathrm{b}} - \epsilon\eta \tag{4.8}$$

after the fast contribution from the surface, as derived in (Rohrschneider et al., 2019). Following this conceptual framework, the slow mode is a function of the deep ocean component T_{D} because the slow mode emerges from the heat transport into the deep ocean and the convergence of the state-variables over time towards the same equilibrium temperature perturbation.

Using linear model versions without feedback temperature dependence, the two-region model and the two-layer model are mathematically equivalent. Although no analytical solution of the coupled two-layer model with feedback temperature dependence exists to date, we can approximate the temperature and radiative response associated with the slow mode by a single effective region (Eq. 5), having a single heat capacity. However, the parameters of the two-layer model modify the inertia of the slow mode. For instance, the parameter for the efficiency of ocean heat uptake η is an inertia parameter, and changes in ocean heat uptake cause C_{S} to increase or decrease. Commonly, we assume that the parameters which describe these simple models are constant. In that respect, we emphasize that the slow mode's response is described by

$$C_{\mathrm{S}}\frac{\mathrm{d}T_{\mathrm{S}}}{\mathrm{d}t} = N_{\mathrm{S}} \tag{4.9}$$

where N_{S} is the TOA imbalance associated with the slow mode. After having explored the imprint of feedback temperature dependence on the slow mode, we analyze the interplay of state-varying and time-varying adjustment

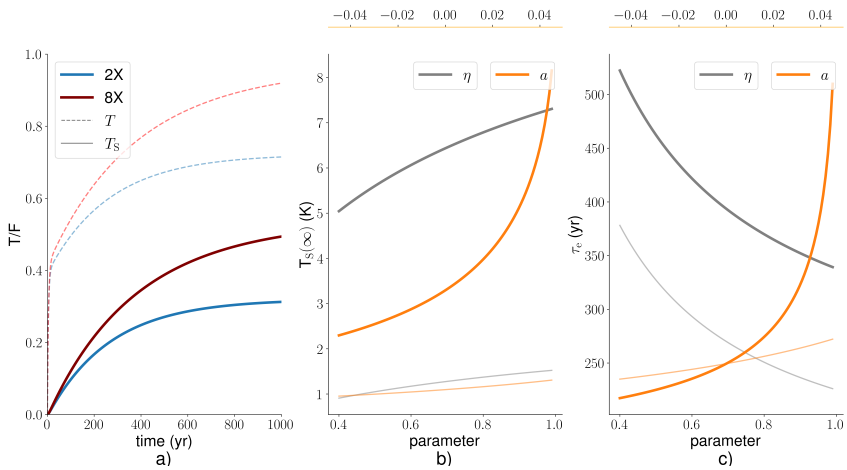

Figure 4.1: a) The slow mode $T_S(t)$ (solid) in the two-layer ocean model normalized by the radiative forcing F in an idealized case. We further show the surface temperature response including the fast mode (dashed). b) The parameter dependencies of the equilibrium temperature response $T_S(\infty)$, and c) the approximated e-folding timescale timescale τ_e (Eq. 10) of the slow mode. As a reference, we use $F = 4$ W m^{-2} (2X) (thin transparent in b) and c)) and $F = 12$ W m^{-2} (8X) (opaque in b) and c)). The reference parameters are $a = 0.04$ W m^{-2} K^{-2}, $\epsilon = 1.5$, $\eta = 0.7$ W m^{-2} K^{-1}, $\lambda_b = 1.5$ W m^{-2} K^{-2}, $C = 10$ W m^{-2} K^{-1} yr , $C_D = 100$ W m^{-2} K^{-1} yr.

timescales. The former arises from the presence of feedback temperature dependence while the latter arises from the inconstancy of C_S according to Eq. (5,9).

As a starting point, we analyze the parameter dependencies of the equilibrium response and timescale of the slow mode T_S (Fig. 1). For illustration only we use the more complicated two-layer ocean model (Eq. 6,7) and focus on the temperature dependence of the global feedback and additionally on the efficiency of ocean heat uptake. The latter allows us to illustrate the changes in the slow temperature adjustment which emerge from the changes in ocean heat uptake. We show the characteristic temperature adjustment of the slow mode T_S assuming positive feedback temperature dependence (Fig. 1a). The temperature response increases relatively to the forcing level in the case of positive feedback temperature dependence and decreases relatively to

the forcing level in the case of negative feedback temperature dependence.

Fig. 1b shows the parameter dependencies of the steady temperature response a of the slow mode. The magnitude of $T_{\mathrm{S}}(\infty)$ increases with more positive feedback temperature dependence a, with higher forcing leading to a more nonlinear response. We further show the parameter dependence of the slow mode T_{S} on the efficiency η. Considering the efficiency of ocean heat uptake η, more efficient heat transport does not change the climate sensitivity $T(\infty)$ but does change the equilibrium response of the slow mode $T_{\mathrm{S}}(\infty)$. The higher η is, the lower is the magnitude of the fast mode $T_{\mathrm{F}}(\infty)$ and the stronger is the magnitude of the slow mode $T_{\mathrm{S}}(\infty)$. We neglect the efficacy factor ϵ in Fig. 1. The efficacy factor ϵ mimics the pattern effect, describing the time-dependence of the radiative feedback on the pattern of surface warming, (Winton et al., 2010; Stevens et al., 2016) and thus represents the differences between regional feedbacks. The higher the efficacy factor for ocean heat uptake ϵ, the less efficient is the radiative response associated with the slow mode and the higher is the equilibrium response of the latter.

Fig. 1c shows the parameter dependencies of the timescale of the slow mode (τ_{e}). For the sake of simplicity, we assume that the evolution of the slow adjustment is approximately described by a single e-folding mode,

$$T_{\mathrm{S}}(t) \approx T_{\mathrm{s}}(\infty)(1 - e^{-t/\tau_{\mathrm{e}}}). \tag{4.10}$$

This makes the strong assumption that the slow mode adjusts on a single timescale that presumably depends on the strength of the forcing. For instance, the analytical solution of the slow mode in the two-region model (Eq. 5) is more complex than this equation (Rohrschneider et al., 2019), and the deviations between these expressions can be interpreted as a time-varying, effective timescale $\tau(t)$. Focusing on the temperature dependence of the global feedback, the timescale of the slow mode τ_{e} increases with more positive feedback temperature dependence, a. As with the equilibrium response $T_{\mathrm{S}}(\infty)$, the timescale of the slow mode increases far more with higher forcing F. By

contrast, more efficient heat transport into the deep ocean (η) decreases the timescale of the slow mode τ_e, so that the equilibrium response is reached at an earlier time.

Using these concepts, we now analyze the outcome of the AOGCM experiments. We focus on the slow mode in light of feedback temperature dependence and the two-region model as the underlying framework. We denote Eq. (5) as the zero-dimensional energy balance model.

4.3 Experimental stratgy

4.3.1 Experimental design

We use four AOGCMs (Table 1) with different qualities that are abruptly forced by 2X, 4X and 8X times the preindustrial CO_2 concentration. Some of the model experiments provide a longer integration time than 1000 years. However, we use only the first 1000 years of simulation time for consistency. The deep ocean adjusts on a multi-millennial timescale but the differences between the extrapolated and actual quasi-equilibrium temperature response at the Earth's surface are small. We analyze the global mean perturbations relative to the control state and use the changes in the surface air temperature $T(t)$ and net TOA imbalance $N(t)$ over time t in order to generate understanding on the slow mode's behavior. The time series are based on annual means.

During the course of the study we use the two-region framework (Eq. 4, 5) to interpret the temperature and radiative response of the slow mode. That is, $T = (1-\chi)T_F + \chi T_S$ and $N = (1-\chi)N_F + \chi N_S$. Having explored the separation of the fast and slow mode in the AOGCMs, we separate them consistently at year 21. At $t = 0$, the radiative forcing F is equal to $N_S(t = 0)$ without applying χ, which is then equivalent to $N(t = 0)$. According to our conceptual framework Eq. (4,5), we assume that the fast mode and the slow

mode are forced by the same global radiative forcing F. Thus, we compute the effective area weighting χ by the ratio between the global mean radiative forcing F and the effective forcing of the slow mode F_{S} which is the y-intercept in the statespace of χT_{S} and χN_{S}.

A preliminary analysis reveals that model 1 and model 2 have positive temperature dependence of the global feedback, model 3 has zero or slightly negative feedback temperature dependence, and model 4 has negative feedback temperature dependence. We solved Eq. (1) for the three different forcing levels; that is, we use the 2X, 4X and 8X AOGCM experiments (i) and solve for $F_i = (\lambda + aT(\infty)_i)T(\infty)_i$. Having six equations, we rearrange first for the background feeedback parameter λ and then, having three equations for each forcing level, for the coefficient for feedback temperature dependence a. Later on, we rearrange for the background feedback parameter of the slow mode λ_{S} and the associated coefficient for feedback temperature dependence a_{S} (Eq. 5). Since our models exhibit a range of both negative and positive temperature dependence, we expect that we can generalize our analysis.

Using the different forcing levels, we use least-square fits of the zero-dimensional energy balance model (Eq. 5) to AOGCM output in order to make predictions and address the deviations of these predictions from the AOGCM response. We expect that the AOCGMs differ in the magnitude and temporal adjustment of the slow mode T_{S}. The characteristic timescale of the slow mode should depend on the climate state while changes in ocean warming may modify the influence of feedback temperature dependence. The ocean response may result in considerable model spread.

4.3.2 Uncertainties

The present study provides arguments which are based on experimental results and does not assess long-term climate change in terms of quantifying forcing and temperature perturbations with great precision. However, during the course of the study we use uncertainties in the radiative forcing F (p^{50},

Table 4.1: the AOGCMs considered in this study

Model	**Reference**
Model 1 (positive feedback temperature dependence*)	MPIESM12 (Mauritsen et al., 2018; Rohrschneider et al., 2019)
Model 2 (positive feedback temperature dependence*)	HadCM3L (Cox et al., 2000; Cao et al., 2016)
Model 3 (zero feedback temperature dependence*)	CCSM3 (Yaeger et al., 2006; Danabasoglu and Gent, 2009)
Model 4 (negative feedback temperature dependence*)	CESM104 (Gent et al., 2011; Rugenstein et al., 2016a)

* In a preliminary analysis we solve Eq. (1) to estimate the feedback temperature dependence of the global feedback. The radiative forcing F is estimated by linearly regressing the relationship between T and N using years 1-10, and the equilibrium temperature response $T(\infty)$ is estimated by linearly extrpolating this relationship using years 100-1000.

p^5 p^{95}) and the slow mode's equilibrium temperature response $T_S(\infty)$ (p^{50}, p^5 p^{95}) in terms of percentiles in order to support our conceptual inferences. We compute the radiative forcing F in the AOGCM experiments by linearly regressing N against T. Using the first year as the lower end, we vary the upper end of the regression time series (after yr 5 to year 20) and apply subsequently bootstrapping by replacement of the forcing estimates in order to generate the details of a continuous probability distribution. There is no unique way to determine the uncertainties in the radiative forcing F, because the estimate of F is based on a sequence with respect to the evolution of T and N. In this connection, the uncertainties themselves are subjective and an indication only. An alternative approach is the application of bootstrapping by replacement before regressing the relationship between N and T. Both approaches are biased, which points out the lack of a sophisticated procedure to determine forcing uncertainties in a more precise way. The disadvantage of our approach is that it overweights the first years of the regression time series as they are steadily involved in the regression. In this sense, we likely overestimate the uncertainty, since the first years of the time series $T(t)$ and $N(t)$ are characterized by rapid adjustments and they are strongly influenced by internal variability. Considering the upper limit of the regression length, our approach neglects these first years because of that influence of major adjustments and internal variability of the climate system at an initial stage. We choose year 20 as the maximum regression length because this timescale approximately describes the equilibration of the fast mode in abrupt CO_2 experiments with AOGCMs.

According to the two-region framework (Eq. 4,5), we estimate the effective area weighting χ in order to scale the responses of the slow mode in relation to the global mean forcing input F. We compute the effective area weighting χ by the ratio between the global mean radiative forcing F and the effective forcing of the slow mode F_{S}. We estimate the latter by linearly regressing the relationship between the slow mode's temperature χT_{S} and energy budget χN_{S}, using the years 21-120 as regression time series to avoid the influence of feedback temperature dependence in the long-term. In general, the signal-to-noise ratio is enhanced after the equilibration of the fast mode and we neglect uncertainties in F_{S}. That is, uncertainties in F are translated into uncertainties in χ only, and in this way the estimates of the background feedback parameter λ_{S} and feedback temperature dependence a_{S} are robust. As with the zero-dimensional energy balance model (Eq. 5), we interpret χ as effective area weighting, although it is not possible to directly prescribe a spatial distribution due to the complex nature of the system's response. Finally, we compute the uncertainties in $T_{\mathrm{S}}(\infty)$ by linearly extrapolating the relationship between the slow mode's temperature response T_{S} and net TOA imbalance N_{S}. Using 10-year intervals, we increase the lower end (from year 100 to year 600) of the regression time-series and use year 1000 as the upper end. Subsequently, we apply bootstrapping by replacement of the temperature estimates only to make sure that the distribution is not biased with respect to extreme outliers. In terms of probabilities, the differences between the original sample and the posterior distribution are marginal.

4.3.3 AOGCM properties

In general, recent AOGCMs agree in that the Southern Ocean and the Eastern Tropical Pacific contribute substantially to the emergence of the slow mode (not shown). These regions are directly coupled to the state of the intermediate and deep ocean. However, nonlinear behavior of the slow mode is likely attributed to both local and nonlocal feedbacks as well as state-dependent changes in the ocean component of the Earth system. In some models, nonlinearities may be highly localized, whereas in other models non-

linear changes with forcing may be evenly distributed over the Earth's surface. We therefore analyze the slow mode's response from a global perspective.

The slow mode emerges from ocean heat uptake but also actuates a different feedback parameter than the fast mode in many climate models, since the fast mode and the slow mode are not only discrete in terms of their temperature perturbation but also in terms of their relationship to the net TOA radiative imbalance. This becomes evident when analyzing the relationship between T and N found in the AOGCM experiments (Fig. 2). As stated above, we interpret the relationship between between T and N as $T = (1-\chi)T_{\mathrm{F}} + \chi T_{\mathrm{S}}$ and $N = (1-\chi)N_{\mathrm{F}} + \chi N_{\mathrm{S}}$. In general, the relationship between T_{F} and N_{F} differs substantially from the relationship between T_{S} and N_{S}. In Fig. 2, we illustrate the magnitude of the fast mode's feedback parameter $\frac{\mathrm{d}N_{\mathrm{F}}}{\mathrm{d}T_{\mathrm{F}}}$ and the slow mode's feedback parameter $\frac{\mathrm{d}N_{\mathrm{S}}}{\mathrm{d}T_{\mathrm{S}}}$ by linear regression. The feedback parameter of the fast mode T_{F} is much stronger than the feedback parameter of the slow mode T_{S}. Focusing on the slow mode, we find considerable changes in $\frac{\mathrm{d}N_{\mathrm{S}}}{\mathrm{d}T_{\mathrm{S}}}$ with forcing, and these changes are in line with the sign of the temperature dependence of the global feedback (Table 1). Comparing the 2X and 8X experiments, we find a decrease in the magnitude of $\frac{\mathrm{d}N_{\mathrm{S}}}{\mathrm{d}T_{\mathrm{S}}}$ with forcing in model 1 and model 2. The feedback parameter $\frac{\mathrm{d}N_{\mathrm{S}}}{\mathrm{d}T_{\mathrm{S}}}$ stays approximately constant or increases slightly with forcing in model 3, and it increases with forcing in model 4. The nature of the relationship between N and T and the separation of the fast and slow mode makes it possible to apply the zero-dimensional energy balance model (Eq. 5) and analyze the temporal temperature adjustment of the slow mode in terms of parameters.

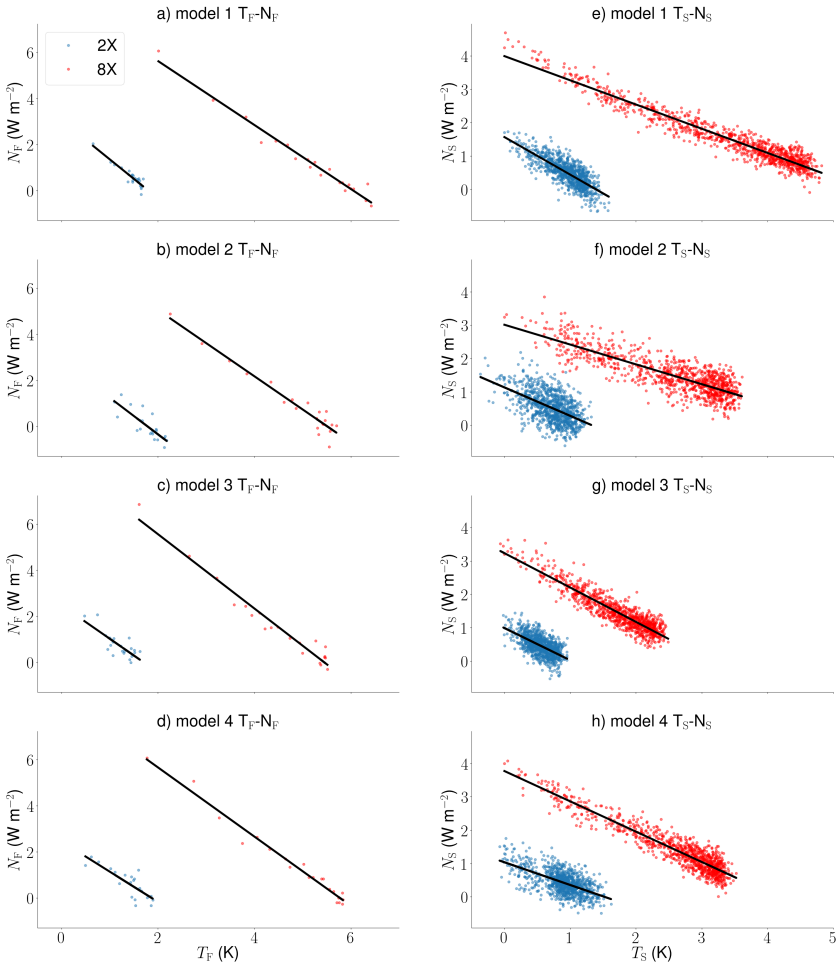

Figure 4.2: On the left (a,b,c,d), the relationship between the temperature perturbation $(1-\chi)T_{\mathrm{F}}$ and net TOA imbalance $(1-\chi)N_{\mathrm{F}}$ of the fast mode in the 2X (blue) and 8X (red) experiments. On the right (e,f,g,h), the relationship between the temperature perturbation χT_{S} and net TOA imbalance χN_{S} of the slow mode in the 2X (blue) and 8X (red) experiments. We further show the linear regression of the relationship between these variables in order to indicate the fast mode's feedback parameters $\frac{\mathrm{d}N_{\mathrm{F}}}{\mathrm{d}T_{\mathrm{F}}}$ and the slow mode's feedback parameter $\frac{\mathrm{d}N_{\mathrm{S}}}{\mathrm{d}T_{\mathrm{S}}}$ over the years 21-1000.

4.4 The influence of feedback temperature dependence

4.4.1 The slow mode in AOGCM experiments

We now analyze the slow mode's behavior by analyzing the temporal evolution of the global mean surface air temperature T. Fig. 3 (a,b,c,d) shows the evolution of the slow mode T_S at the Earth's surface in the different AOGCMs. In model 1 and model 2, the slow mode increases nonlinearly with each doubling of the atmospheric CO_2 concentration, in the sense that the relative temperature change between the CO_2 levels increases. By contrast, the relative temperature change between the different CO_2 levels stays approximately constant in model 3 and decreases in model 4. These changes correspond to the temperature dependence of the global feedback in the AOGCMs (Table 1). Next, we normalize the temperature adjustment of the slow mode T_S by the radiative forcing F. Fig. 3 (e,f,g,h) shows the normalized evolution of the slow mode at the Earth's surface to demonstrate that the nonlinear behavior is mostly related to feedback temperature dependence. We use the the 2X and 8X abrupt CO_2 experiment only in order to have a large signal. The nonlinear behavior of the slow mode T_S in model 1 and model 2 does not arise from the changes in the radiative forcing F. The slow mode in model 3 behaves in a linear way and the lines for the temperature evolution are approximately congruent. Model 4 has negative feedback temperature dependence, and the normalized temperature response T_S in the 2X experiment is higher than the normalized temperature response in the 8X experiment. In the following, we analyze the changes in the steady and temporal behavior of the slow mode in more detail. Therefore, we characterize both the equilibrium response and timescale of the slow mode T_S as represented in the AOGCMs.

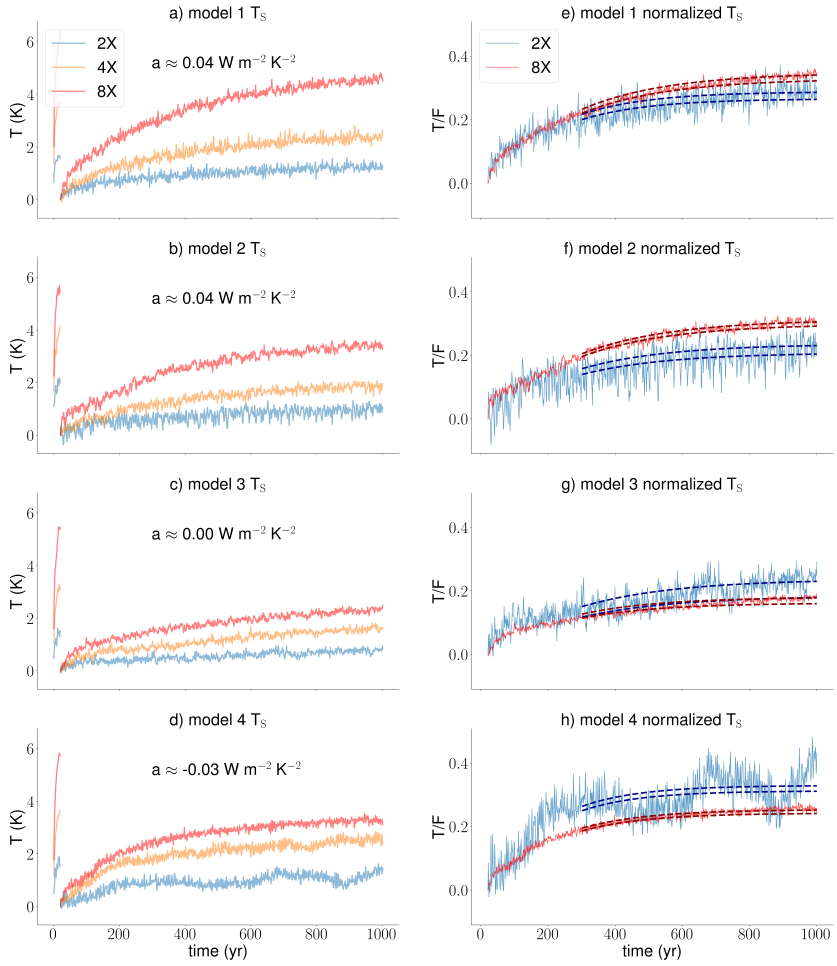

Figure 4.3: The slow mode $\chi T_S(t)$ of the climate response in the AOGCMs experiments. On the left (a,b,c,d), we show the slow mode in the 2X (blue), 4X (orange) and 8X (red) abrupt CO_2 experiments. We also indicate the fast mode. On the right (e,f,g,h), we normalize the slow mode of the 2X (blue) and 8X (red) experiments by the forcing F (p^{50}), and we further show the uncertainties (p^5,p^{95}) (darkblue and darkred) in the normalization.

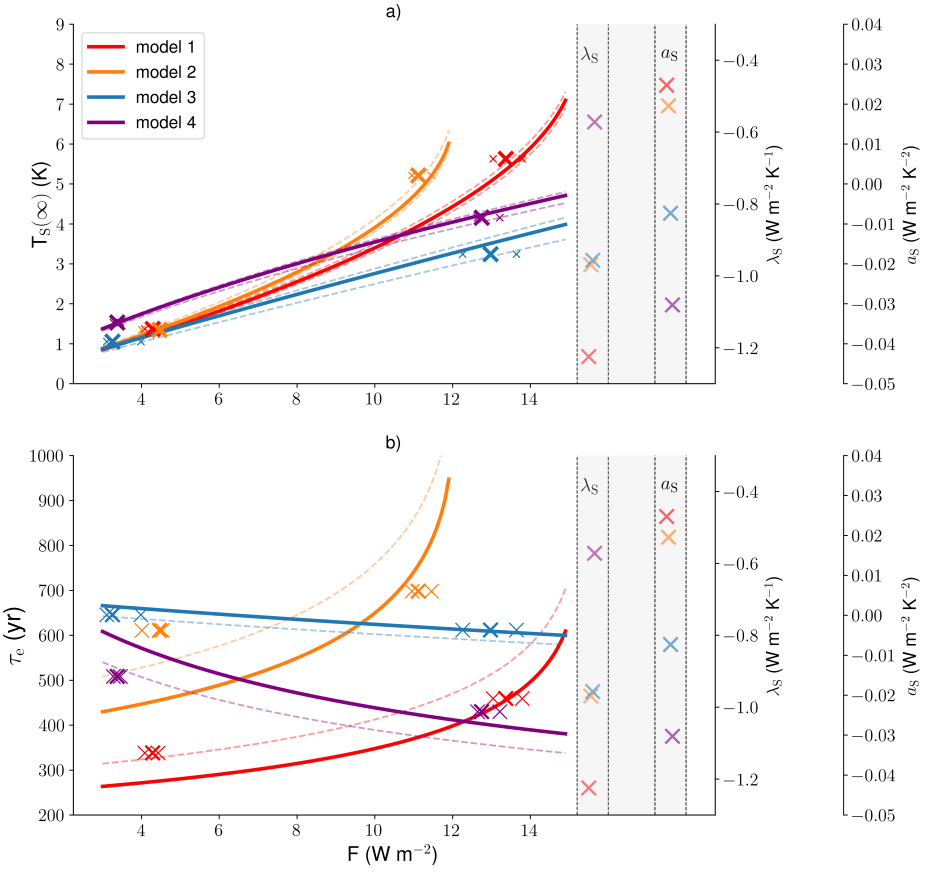

Figure 4.4: a) The equilibrium temperature response $\chi T_S(\infty)$ (p^{50}), and b) the approximated single mode e-folding timescale τ_e (Eq. 10) associated with the slow mode as a function of forcing. The x-markers represent the AOGCM output (2X,8X) and are based on the estimated forcing input F (p^{50}, p^5,p^{95}). The lines are the predictions by the zero-dimensional energy balance model (Eq. 5) using $F(p^{50})$ and $T_S(\infty)(p^{50})$. In (a), we use the effective area weighting χ associated with the global mean forcing F (p^{50}, solid) and F ($p^5$and p^{95}, dashed), computing the average over the three experiments. In (b), we fit the temperature evolution of the zero-dimensional energy balance model (Eq. 5) to the AOGCM experiments (2X,8X, solid) and (2X,4X,8X, dashed) in order to determine the effective heat capacity C_S. The background feedback parameters λ_S and the feedback temperature dependencies a_S are shown on the right.

4.4.2 The equilibrium response and timescale

We use the 2X, 4X and 8X AOGCM experiments (i) and solve for $F_i = (\lambda_S + a_S T_S(\infty)_i) T_S(\infty)_i$ in order to first compute the slow mode's background feedback parameter λ_S and then the coefficient for feedback temperature dependence a_S. In this way, the response of the slow mode T_S can be described as a continuous function of the global mean radiative forcing F (Fig. 4). The uncertainties in F are translated into uncertainties in χ while the uncertainties in λ_S and a_S are marginal. In general, the background feedback parameter of the slow mode is less strong than the feedback of the fast mode and the net global feedback, which can be inferred from the relationship between N and T (Fig. 2). That is, the feedback temperature dependence a_S associated with the slow mode is also less strong than the feedback temperature dependence of the global feedback. Fig. 4a shows the equilibrium response of the slow mode $T_S(\infty)$ as a function of the radiative forcing F. We find that the equilibrium response $T_S(\infty)$ in the AOGCMs is well described by the zero-dimensional model with feedback temperature dependence. The equilibrium response $T_S(\infty)$ changes exponentially with an increase in forcing in the case of positive feedback temperature dependence. In the case of negative feedback temperature dependence, the response $T_S(\infty)$ is saturated with increasing F.

As with the simple models, we describe the changes in the temporal adjustment of the slow mode with forcing by the changes in the fitted single mode e-folding timescale (Eq. 10) (Fig. 4b). To do so, we determine a single heat capacity by fitting the temperature evolution of the zero-dimensional energy balance model (Eq. 5) to the temperature evolution of the slow mode in the 2X and 8X AOGCM experiments (year 21-1000). That is, we determine the heat capacity C_S. In general, the sign of the changes in the timescale τ_e with forcing in the AOGCMs coincide with the predicted changes by the simple model. The timescales are forcing-dependent because the feedback of the slow mode depends on temperature, and the timescales change exponentially with higher forcing in the case of positive feedback temperature

dependence. The timescales τ_e slightly decrease with higher forcing in the case of negative feedback temperature dependence. Focusing on model 1 and model 2, the changes in the timescales τ_e with higher forcing F are important and of O(100) with respect to the low-end (2X) and high-end (8X) forcing range. In general, it is more difficult to predict the timescales of the slow mode than the equilibrium response $T_S(\infty)$. In this connection, including an additional experiment such as a quadrupling of the atmospheric CO_2 concentration (4X) changes the absolute values significantly (dashed line). This shows that the predictions of the effective timescale are not robust, and the temperature evolution of the slow mode may not exactly follow the relationship described by Eq. (9) considering that the ocean's response influences the temporal evolution of the slow mode. To a large extent, these changes explain the major deviations from the theoretical predictions by the zero-dimensional energy balance model (Eq. 5), and we can interpret them as changes in the effective heat capacity C_S. In the next section, we explore to which degree the temporal adjustment of the slow mode T_S depends on the strength of the forcing.

4.4.3 Imprint of feedback temperature dependence

We quantify the differences in the timing of the long-term warming in the AOGCMs between the low-end (2X) and the high-end forcing range (8X). We prescribe the slow mode's temporal adjustment of the 2X experiments to the 8X experiments by using the equilibrium response $T_S(\infty)$ of the 8X experiments and the effective timescale of the 2X experiments. Assuming a linear e-folding mode, we quantify the effective timescale by rearranging Eq. (10);

$$\tau(t) = -t/log(\frac{T_S(\infty) - T_S(t)}{T_S.(\infty)}). \tag{4.11}$$

Fig. 5 shows that the temporal adjustment of the slow mode $T_S(t)$ between the 2X and 8X experiment is substantially altered. The computation is influenced by temporal changes of the effective timescale $\tau(t)$ in the 2X experiment such as changes in the ocean circulation. However, we use uncertain-

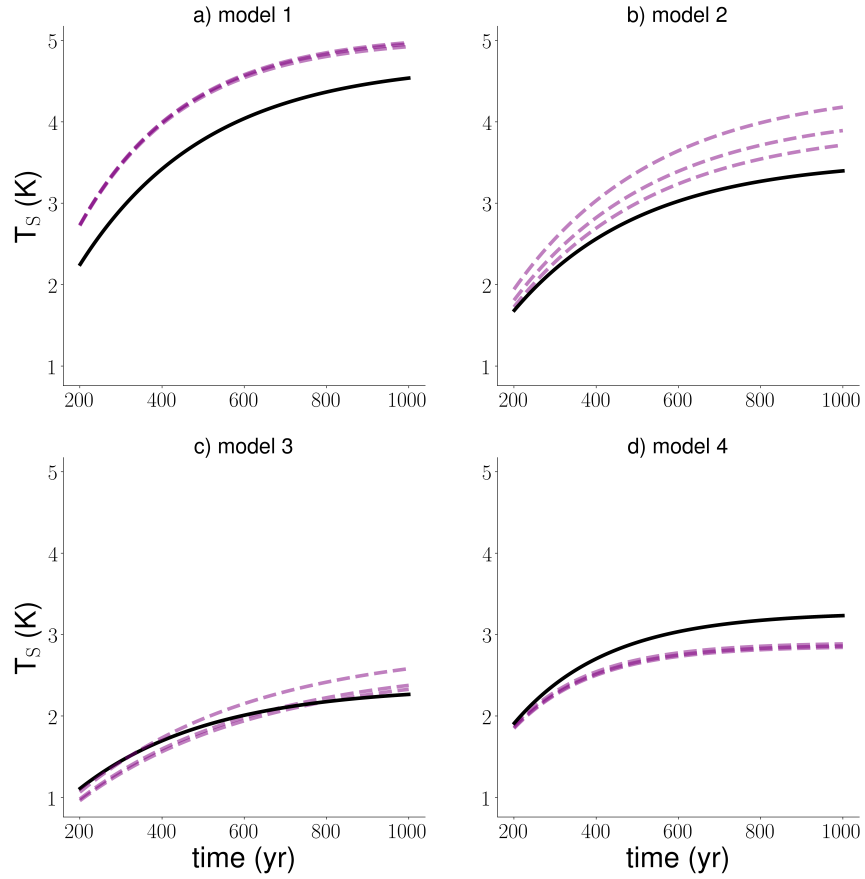

Figure 4.5: The slow mode $\chi T_{\mathrm{S}}(t)$ in the 8X AOGCM experiments (black) and the inferred slow mode $\chi T_{\mathrm{S}}(t)$ of the 8X experiments (purple) from the effective timescale $\tau(t)$ of the 2X experiment. We use the uncertainties that arise from the uncertainties $T_{\mathrm{S}}(\infty)$ (p^{50},p^{5}, p^{95}). Using Eq. (11), we prescribe the temporal adjustment of the 2X experiment while using the equilibrium temperature response $T_{\mathrm{S}}(\infty)$ in the 8X simulations. In order to avoid internal variability, we fit an arbitrary e-folding mode, neglecting the initial adjustment and focussing on the temperature response on a centennial timescale.

ties in $T_S(\infty)$ in order to support our inferences. The marked uncertainties support the perspective that the timescales change considerably due to the presence of feedback temperature dependence. Prescribing the temporal adjustment of the 2X experiment, we overestimate the temperature evolution on a multi-centennial timescale with higher forcing in the case of positive feedback temperature dependence (model 1 and model 2). We find only small changes in the case of approximately zero feedback temperature dependence (model 3), and we underestimate the temperature evolution on a multi-centennial timescale with higher forcing in the case of negative feedback temperature dependence (model 4). In general, the influence of negative feedback temperature dependence is less strong than the influence of positive feedback temperature dependence. Our findings on the temporal adjustment of the slow mode in the AOGCMs indicate the importance of feedback temperature dependence for committed warming on a multi-centennial to millennial timescale in case of high forcing input. Linear models cannot capture long-term climate change in an appropriate way in the presence of feedback temperature dependence, since they suggest that the effective timescale does not depend on the climate state, and the temporal adjustment of the slow mode would be independent of the degree of warming as found in model 3.

4.5 Varying timescale(s)

In this section we analyze the presence of both temperature or forcing-dependent and time-varying adjustment timescales $\tau(t)$. We further highlight the implications of the time-variation variation of $\tau(t)$ for eigenmode decomposition.

4.5.1 The effective time scale

We compare the effective timescale $\tau(t)$ (Eq. 11) of the slow mode found in the AOGCM experiments and the effective timescale $\tau(t)$ predicted by the zero-dimensional energy balance model (Eq. 5) (Fig. 6). The effective timescale describes the temporal temperature adjustment at any point of

time. By its nature, $\tau(t)$ depends sensitively on the equilibrium response $T_S(\infty)$ in the sense that Eq. (11) is not an independent measure of the temporal behavior. However, it describes how temperature unfolds and therefore the fractions of the equilibrium response that are reached at different times. We likely underestimate $T_S(\infty)$ in the case of positive feedback temperature dependence and overestimate $T_S(\infty)$ in the case of negative feedback temperature dependence.

As can be seen from Fig. 6, for both AOGCMs and the zero-dimensional energy balance model, the effective timescale $\tau(t)$ of the AOGCM experiments differs between the forcing levels, and these differences are in line with the feedback temperature dependence of the slow mode T_S. The effective timescale $\tau(t)$ increases with higher forcing in the case of positive feedback temperature dependence (model 1 and model 2), stays approximately constant or decreases slightly in the case of model 3, and decreases in the case of negative feedback temperature dependence (model 4). The predicted timescale $\tau(t)$ of the zero-dimensional energy balance model (Eq. 5) shows an increase with time in the case of positive feedback temperature dependence and high forcing input. In mathematical terms, this increase in $\tau(t)$ with time is attributed to the more complicated analytical solution of the energy balance model than Eq. (10) as discussed in section 2. In the case of negative feedback temperature dependence, the effective timescale $\tau(t)$ decreases slightly with time in the simple model.

By contrast, the AOGCM experiments reveal that the effective timescale $\tau(t)$ increases with time regardless of positive or negative feedback temperature dependence or low and high forcing input F. The time-variation of $\tau(t)$ of the slow mode in the complex climate models is stronger than the time-variation predicted by the zero-dimensional energy balance model (Eq. 5). The uncertainties in the equilibrium response $T_S(\infty)$ support common model behavior, and even lower values than the estimated equilibrium response $T_S(\infty)$ would cause $\tau(t)$ to vary over time. In general, the temperature of the slow mode adjusts on longer timescales as time increases. The

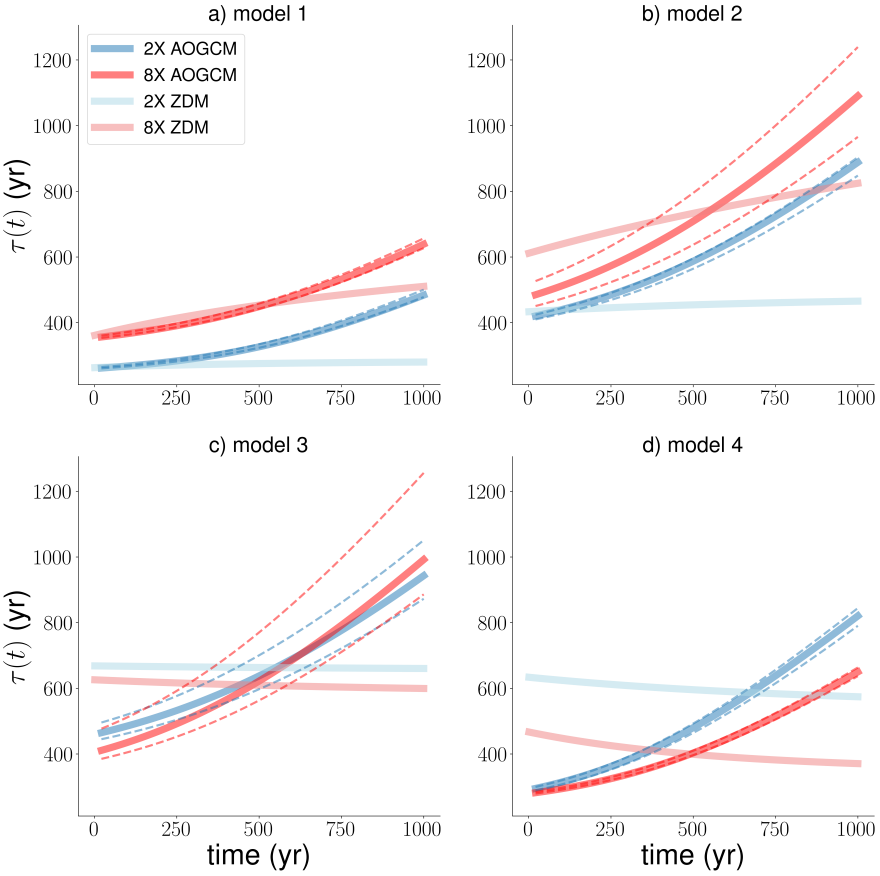

Figure 4.6: The effective timescale $\tau(t)$ (Eq. 11) of the slow mode $T_{\mathrm{S}}(t)$ in the 2X (blue) and 8X (red) AOGCM experiments. We further show the predictions by a zero-dimensional energy balance model (ZDM) fit to the 2X experiments (orange) and 8X experiments (purple). Using the AOGCM output, we fit an arbitrary e-folding mode to exclude internal variability. Using $F(p^{50})$ and $T_{\mathrm{S}}(\infty)(p^{50})$, the temperature evolution of the zero-dimensional energy balance model (Eq. 5) is fitted to the 2X and 8X AOGCM experiments in order to determine the effective heat capacity C_{S}. We recalculate the effective timescale $\tau(t)$ in the AOGCM experiments using the uncertainties that arise from the uncertainties $T_{\mathrm{S}}(\infty)$ (p^{50},p^{5}, p^{95}).

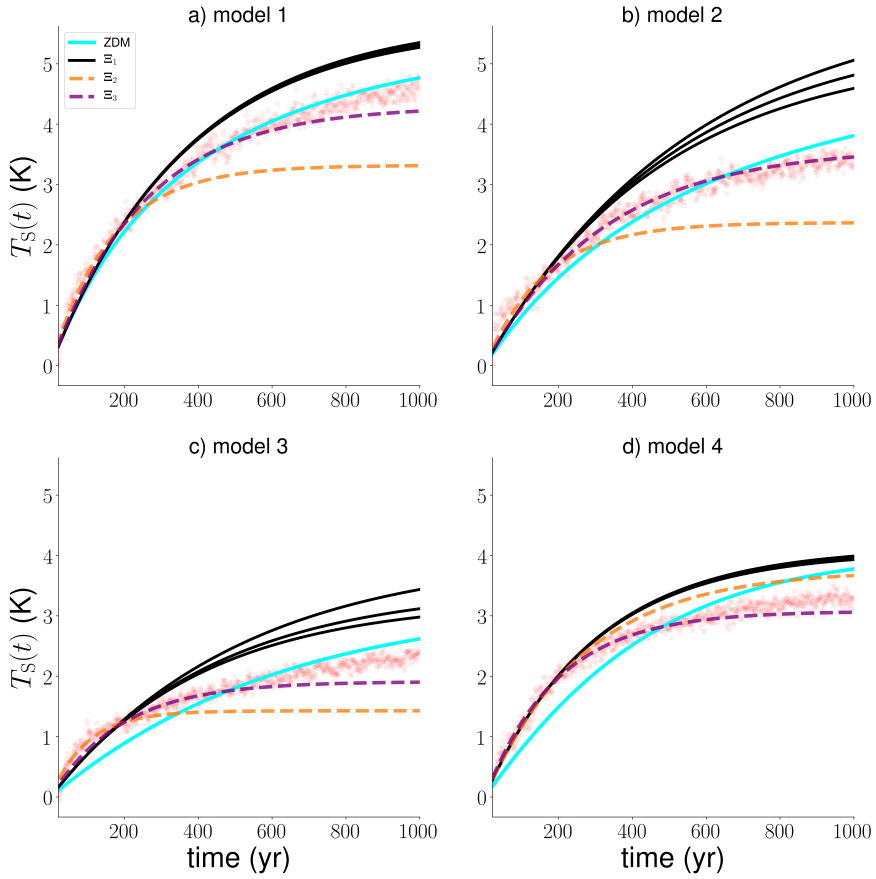

Figure 4.7: The temporal adjustment of the slow mode $\chi T_S(t)$ in terms of modes in the 8X AOGCM experiments (red). We show a single linear eigenmode (e-folding mode) with a constant timescale approaching the equilibrium response $T_S(\infty)$ (p^{50},p^5, p^{95}), using the temporal average of years 20-200 of the effective timescale to compute τ at an initial stage (Ξ_1, black lines). We further show the analytical computation of the eigenmode (e-folding mode) using the time interval $t_1 = 100$ and $t_2 = 200$ (Ξ_2, dashed orange lines) and the time interval $t_1 = 200$ and $t_2 = 400$ (Ξ_3, dashed purple lines). For Ξ_2 and Ξ_3, the time series $\chi T_S(t)$ has been smoothed by a 100-year running mean. Finally, we show the temperature evolution of the zero-dimensional energy balance model (ZDM) (Eq. 5) fitted to the 8X AOGCM experiments ($F(p^{50})$ and $T_S(\infty)(p^{50})$) only in order to compute the effective heat capacity C_S (cyan lines).

findings on $\tau(t)$ in the AOGCMs suggest a time-dependent component of the Earth system that changes the inertia in the long-term such as changes in the ocean circulation. Thus, the temperature response of the slow mode does not exactly satisfy $C_{\mathrm{S}}\frac{\mathrm{d}T_{\mathrm{S}}}{\mathrm{d}t}$ (Eq. 5,9) in the sense that the effective heat capacity is no longer constant over time according to this framework, or suggesting a multiple mode structure. The time-varying adjustment timescale can be approximated by a multiple timescale structure of the slow temperature response, or vice versa, a multiple timescale structure of the slow temperature response is described by a time-varying timescale. The signal that arises from feedback temperature dependence gives a state-dependent adjustment timescale and is robust, but the long-term temperature adjustment is related to multiple modes or a continuously-varying timescale. There is the possibility that the separation of the fast mode and slow mode at a specific year is inappropriate, but we expect that the errors are small and we could not explain the deviations from the simple model predictions.

4.5.2 Limits of the two-timescale approach

We illustrate the influence of the time-variation of $\tau(t)$ by focusing on the 8X experiments in order to explore the details of the slow mode's temperature adjustment in light of feedback temperature dependence a_{S} and inconstant inertia C_{S} (Fig. 7). We use a single forcing level only to highlight the limits of having a single exponential mode with a constant e-folding timescale and the zero-dimensional energy balance model also.

As a starting point, we assume a constant timescale τ which prescribes the temporal adjustment of a single e-folding mode with respect to the equilibrium response $T_{\mathrm{S}}(\infty)$ (Eq. 10). The constant timescale τ represents the timescale $\tau(t)$ of the AOGCM experiments at an initial stage, using years 20-200. The temperature adjustment of the slow mode on multi-centennial timescale is considerably overestimated (Ξ_1), because the temperature adjustment of this exponential mode occurs on much shorter timescales than the actual timescales. Next, we compute analytically the exponential eigen-

mode by assuming that this eigenmode reproduces the temperature response in the time-interval t_1 and t_2. Using Eq. (10) we solve for a certain time-interval which gives the e-folding mode amplitude

$$T_{\Xi}(\infty) = \frac{T_{\mathrm{S}}(t_1)^2}{2T_{\mathrm{S}}(t_1) - T_{\mathrm{S}}(t_2)} \tag{4.12}$$

as long as $t_2/t_1 = 2$. We then solve Eq. (10) to compute the associated timescale τ_{Ξ}. Considering the adjustment at an initial stage ($t_1 = 100$ and $t_2 = 200$), the temperature evolution of the eigenmode deviates strongly from the temperature evolution in the 8X experiments in terms of amplitude and temporal adjustment (Ξ_2). The AOGCM temperature response and the eigenmode converge when using a time-interval on a multi-centennial timescale ($t_1 = 200$ and $t_2 = 400$), with a more accurate prediction with longer time-intervals (Ξ_3). Using longer time-intervals on a multi-centennial timescale is a circumvention to keep a single e-folding mode as a description for the slow mode's behavior. In doing so, errors are weighted to the long-term response while deviations are small on a multi-decadal and centennial timescale. For instance, choosing the time-interval $t_1 = 500$ and $t_2 = 1000$ minimizes the errors considering the 1000-year temperature time series but the amplitude of these eigenmodes are substantially lower than the extrapolated equilibrium responses $T_{\mathrm{S}}(\infty)$ in the AOGCMs (not shown), using the relationship between N and T.

Finally, the temperature evolution of the zero-dimensional energy balance model (Eq. 5) with feedback temperature dependence is fitted to the temperature evolution in the 8X AOGCM experiments only. We underestimate the temperature response on a multi-decadal and centennial timescale and overestimate the temperature response on a multi-centennial timescale. The differences are small in the case of model 1 because the time-variation of $\tau(t)$ in model 1 is relatively low compared to model 2, model 3, and model 4. However, according to the zero-dimensional energy balance model (Eq. 5,9), C_S increases over time, with much higher values on a multi-centennial timescale.

4.6 Discussion

Several studies use linear eigenmode decomposition and realize fitting (Eq. 3) in order to approximate the temperature evolution in response to radiative forcing (Olivie et al., 2012; Caldeira and Myhrvold, 2013; Proistosescu and Huybers, 2017). These studies are based on AOGCM simulations which have an integration time no longer than 300 years and thus do not capture properly the timescales of long-term climate change. In line with theory, Olivie et al. (2012) find that the temperature evolution is described by a fast e-folding mode and slow e-folding mode. Caldeira and Myhrvold (2013) show that fitting two exponential modes with different timescales does equivalently reproduce the temperature response in AOGCMs as a one-dimensional slab diffusion ocean model does. In this connection, fitting two exponential modes does not necessarily imply two or more underlying and discrete processes, but it is ultimately based on a physical conceptual model. They further demonstrate that the difference between fitting two exponential modes and fitting three exponential modes is small on the timescale considered in their analysis. From their perspective, fitting three exponential modes lacks an underlying physical theory. Finally, Proistosescu and Huybers (2017) find that three e-folding modes approximate the temperature evolution found in AOGCMs in more detail. According to their analysis, a fast and intermediate exponential mode project primarily onto continental regions, whereas the slow mode on a centennial timescale is associated with the ocean adjustment. We consider the slow mode only and demonstrate that the timescale of the slow mode is forcing-dependent. We find that the temperature response at different forcing levels cannot be described by an exponential eigenmode with a constant e-folding timescale. At the same time, however, a forcing-dependent timescale does not fully account for the time-variation of the effective timescale found in the AOGCMs considered here. Using linear eigenmode decomposition, at least one additional mode or a multiple mode and timescale structure of the slow adjustment is necessary to reproduce the details of long-term climate change in an appropriate way. Keeping a single mode, computing the eigenmode for the long-term response of the slow mode on a multi-centennial

timescales circumvents a multiple mode and timescale structure at the expense of a detailed representation of the temperature adjustment on a multi-decadal and centennial timescale and the actual equilibrium temperature response. Either way, such an eigenmode decomposition is valid for a certain forcing level only.

4.7 Summary and Conclusion

Feedback temperature dependence influences the slow mode of the climate response in a substantial way by changing both the equilibrium response and timescale of long-term climate change which is thereby state-dependent. At the same time, the thermal inertia of the slow mode is not constant over time. Applying eigenmode decomposition, the two-timescale approach with constant timescales cannot capture the details of long-term climate change according to the experimental findings of the present study. The specific estimate of the timescale depends sensitively on the estimate of the equilibrium temperature response, but the finding that it changes with forcing and time is robust.

The equilibrium response of the slow mode is well described by a zero-dimensional energy balance model that incorporates a background feedback parameter and a coefficient for feedback temperature dependence and a constant heat capacity. This model can be interpreted as an effective region which has much more inertia than the effective region that is associated with the fast mode. The zero-dimensional model captures major changes in the slow mode's adjustment timescale with forcing, and the AOGCM experiments show that the temporal adjustment of the slow mode depends on the climate state in the case of non-zero feedback temperature dependence. However, the adjustment timescales predicted by the zero-dimensional model and the adjustment timescales found in the AOGCM experiments differ considerably. There is a stronger time-variation of the effective timescale of the slow mode in the AOGCM experiments than predicted by theory. The effective timescale of the slow mode in the AOGCM experiments increases with time

regardless of positive or negative feedback temperature dependence. Thus, the time-variation of the effective timescale cannot be explained by feedback temperature dependence only and the details of the slow, long-term temperature evolution are not well captured by the zero-dimensional energy balance model. Accordingly, the inconstancy of the thermal inertia can be approximated by a continuously varying timescale or a multiple timescale structure.

We find substantial model spread in how the AOGCMs reproduce long-term climate change, and state-dependent changes in the ocean's response may change the timing of the long-term temperature adjustment considerably. Our results depend on the outcome of a limited number of AOGCM experiments which are the only publicly experiments which have an integration time of 1000 years. The present study makes clear the importance of long-term climate change experiments simulated beyond year 2100 in order to predict and constraint the slow mode's behavior and future warming. However, both conceptual models and the AOGCMs considered here imply that feedback temperature dependence plays a large role in determining the extent and timing of long-term global warming. Research has to be done on why the adjustment timescale of long-term global warming is not constant over time.

Chapter 5

Outlook

5.1 Introduction

As the second paper of the thesis finishes, the question arises why there is the time-variation of the adjustment timescale of the slow mode or a multiple timescale structure. There are mainly two explanations which should be investigated in future. First, changes in the ocean circulation or ocean heat uptake cause time-variation of the adjustment timescale of the slow mode, in the sense that the effective heat capacity is not constant over time. Secondly, there is a geographic timescale pattern that causes time-variation of the adjustment timescale of the slow mode in the sense that the effective heat capacity is not uniform. I describe more extensively the first approach as it is not a matter of concern in the current literature. By contrast, the pattern effect is well studied and understood (Armour et al., 2013; Stevens et al., 2016; Rohrschneider et al., 2019). Both approaches can represent the same outcome because the time-variation of the global heat capacity can be associated with a geographic pattern of regional effective heat capacities. At the same time they are separate approaches, since the first approach is a global perspective and the latter approach can only be analyzed geographically. Finally, the global approach does account for changes in the ocean circulation, whereas the latter approach is more static by its nature except that we allow the geographic timescale pattern to vary with time.

5.2 Efficiency of ocean warming

The pace of surface warming in response to external radiative forcing is strongly related to the efficiency of ocean heat uptake, which is commonly defined as the ratio between the global mean ocean heat uptake perturbation (H) and global mean surface temperature perturbation (T) (Raper et al., 2002),

$$\kappa = \frac{H}{T}. \tag{5.1}$$

Actually, the deep ocean response is linked to an effective thermal inertia that is not infinite. In this regard, the efficiency of ocean heat uptake can also be defined as the global mean perturbation heat flux into the deep ocean H divided by the temperature difference between the surface (T) and the deep ocean (T_{D}) global mean temperature perturbation (Held et al., 2010; Winton et al., 2010),

$$\eta = \frac{H}{T - T_{\mathrm{D}}}. \tag{5.2}$$

The latter can be interpreted as the efficiency of ocean warming because the heat flux into the deep ocean is proportional to the ocean warming rate. In the following I provide an example for the time-variation of η in the abrupt CO2 experiments with the MPI-ESM1.2 coupled climate model. I use annual-mean ocean potential temperatures $\theta(z,t)$ at depth z which are temperature parcels brought adiabatically to the surface. In this connection, I analyze the efficiency $\eta(t)$ of ocean warming $T_{\mathrm{D}}(t)$ (Eq. 5.2). The upper levels of the global mean ocean temperatures are roughly characterized by a fast response on a decadal timescale and a slow response after the decadal adjustment. At deeper levels, the response after the initial adjustment on a decadal timescale and the actual response of the deep ocean component are approximately equal, because the slow mode is a function of the deep ocean component. I use the depth range between the surface and 2000 meters depth, which roughly scales the height of the upper branch of the meridional overturning circulation and advective ocean heat uptake in the Southern Ocean. The efficiency considered here is connected to the warming of the deep ocean component which is in disequilibrium and a function of depth but influences

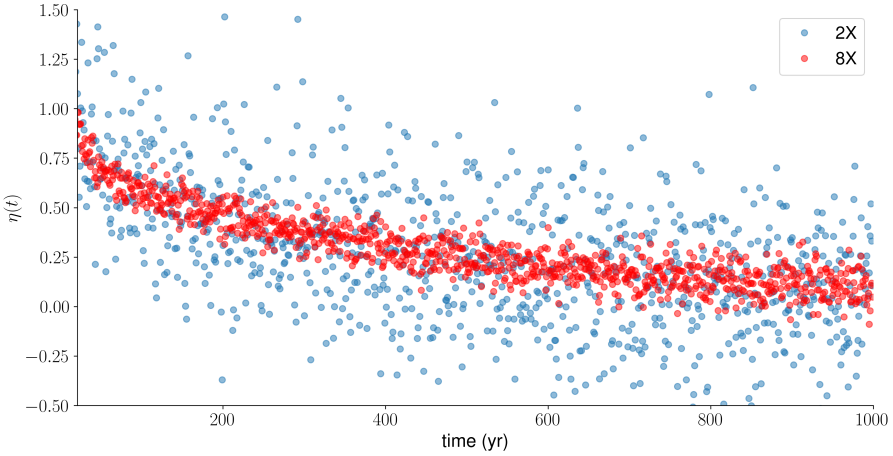

Figure 5.1: The efficiency of ocean warming $\eta(t)$ in the abrupt CO_2 MPI-ESM.1.2 experiments.

the long-term temperature adjustment at the Earth's surface. In that respect, the efficiency of ocean warming is different from the heat transport efficiency in the two-layer ocean model (Eq. 4.6,4.7), but it indicates how the effective thermal inertia of the long-term surface temperature changes over time or with climate state. It cannot be implemented in the two-layer ocean model because in the simple model the temperatures converge to the same equilibrium temperature response. The heat flux associated with the deep ocean component is $c_p \rho_\mathrm{r} D \frac{\mathrm{d}T_\mathrm{D}}{\mathrm{d}t}$ with c_p the specific heat, and ρ_r (1025 kg m^{-3}) is the reference density.

In part, the time-variation of the effective timescale $\tau(t)$ can be associated with the ocean adjustment. It is difficult to understand the time-variation of the effective timescale using Eq. (5.1) which is the ratio between total ocean heat uptake (H) and surface temperature change (T). The presence of multiple state-variables such as a surface and deep ocean temperature cause the efficiency κ to vary over time. The efficiency κ should decrease towards equilibrium because the surface and ocean temperatures converge. The state-dependence of the surface temperature adjustment and ocean heat uptake make an interpretation more complex. In Eq. (5.2), the heat flux into

the deep ocean scales linearly with the temperature difference between the surface T and the deep ocean T_{D}. Normalizing the temperature difference $T - T_{\mathrm{D}}$ by the radiative forcing F, this difference should increase with higher forcing levels in the case of positive feedback temperature dependence, stay approximately constant in the case of zero feedback temperature dependence, and decrease in the case of negative feedback temperature dependence (not shown). The slow mode is commonly thought to be a function of the deep ocean component T_{D} according to the two-layer ocean model, and ocean heat uptake H of the deep ocean component T_{D} mainly sets the effective inertia of the slow, long-term surface temperature adjustment. The higher the efficiency, the more rapid the adjustment of the slow mode T_{S}. However, current theories do not provide any insights on the influence of transient changes of $\eta(t)$ on long-term climate change. We find that $\eta(t)$ has a time-dependent component (Fig. 5.1). This time-dependence does not change the state-dependence of the adjustment timescales $\tau(t)$ because these adjustment timescales still depend on the strength of the forcing F. Applying Eq. (5.2), however, the decrease of the efficiency $\eta(t)$ over time increases the thermal inertia of the system C_{S} in an effective way, leading to a long-term increase in $\tau(t)$. The time-dependence of $\eta(t)$ is explained by different timescales of ocean heat uptake and the adjustment of the ocean circulation, and the strength of the effect of $\eta(t)$ on the slow surface temperature adjustment is model-specific (not shown) though we expect common model behavior in the sense that the efficiency decreases over time. The nature of state-dependent changes in the efficiency η may be transient. State-dependent changes in $\eta(t)$ could be related to misleading interpretations of feedback temperature dependence associated with the fast and slow mode, and they change the adjustment timescales. In general, the time-variation of the efficiency of ocean warming can be associated with a geographic pattern of effective ocean heat capacities, which may additionally vary with time. However, the geographic pattern of effective ocean heat capacities emerges from the ocean circulation.

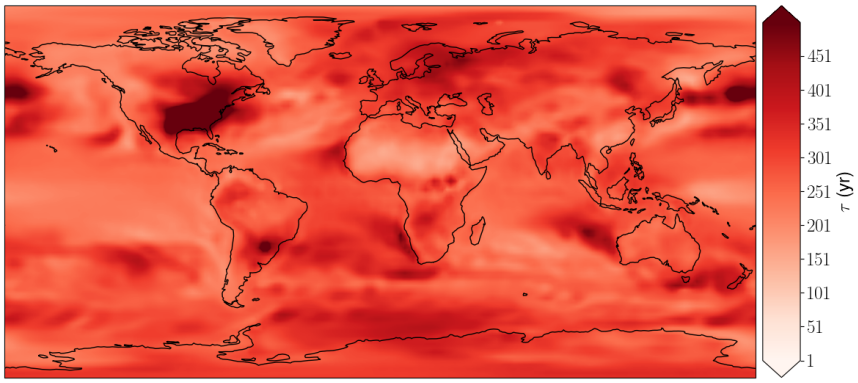

Figure 5.2: The geographic timescale pattern in the MPIESM1.2 8XCO2 experiment. I assume that temperature unfolds on a single e-folding mode as in Eq. (4.10). For simplicity, I approximate the equilibrium temperature $T(\infty)$ by using the end of the model time series which is the temporal mean of the years 990-1000.

5.3 Timscale pattern

Finally, another, more explicit approach that explains the time-variation of the slow mode is a geographic timescale pattern. The pattern effect may arise from the pattern of radiative feedbacks as well as regional dynamics in ocean heat uptake that changes the temporal temperature adjustment. The latter makes a distinction between the two explanations presented here more complex, since the efficiency of ocean warming can be associated with a pattern of effective ocean heat capacities. The possibility of spatial patterns of regional feedbacks further obscure the direct influence of the time-variation $\eta(t)$ on the slow mode, since they cause a multiple mode structure in the long-term. In Fig. 5.2 I show the geographic timescale pattern of the slow mode in the MPI-ESM1.2 8XCO2 experiment. In the case of MPI-ESM1.2, the pattern is weak. Other models with more time-variation of $\tau(t)$ may have a stronger timescale pattern.

Part III

References

Bibliography

L. C. Allison, H. L. Johnson, and D. P. Marshall. Spin-up and adjustment of the antarctic circumpolar current and global pycnocline. *Journal of Marine Resaerch*, 69:167–189, 2011. doi: 10.1357/002224011798765330.

T. Andrews, J. Gregory, P. Forster, and M. J. Webb. Cloud adjustment and its role in CO_2 radiative forcing and climate sensitivity: A review. *Surveys in Geophysics*, 33:619–635, 2012. doi: 10.1007/s1071201191520.

K. C. Armour, C. M. Bits, and G. H. Roe. Time-varying climate sensitivity from regional feedbacks. *Journal of Climate*, 26:4518–4534, 2013. doi: 10.1175/JCLI-D-12-00544.1.

J. Baehr, J. Hirschi, J. O. Beismann, and J. Marotzke. Monitoring the meridional overturning circulation in the north atlantic: a model-based array design study. *Journal of Marine Research*, 62:283–312, 2004. doi: 10.1357/0022240041446191.

J. Baehr, A. Stroup, and J. Marotzke. Testing concepts for continuous monitoring of the meridional overturning circulation in the south atlantic. *Ocean Modelling*, 29:147–153, 2009. doi: 10.1016/j.ocemod.2009.03.005.

S. P. Bishop et al. Southern ocean overturning compensation in an eddy-resolving climate simulation. *Journal of Physical Oceanography*, 46:1575–1592, 2016. doi: 10.1175/JPO-D-15-0177.1.

J. Bloch-Johnson, R. T. Pierrehumbert, and D. S. Abbot. Feedback temperature dependence determines the risk of high warming. *Geophysical Research Letters*, 42:4973–4980, 2015. doi: 10.1002/2015GL064240.

J. Bloch-Johnson, M. Rugenstein, M. B. Stolpe, T. Rohrschneider, Y. Zheng, and J. M. Gregory. Climate sensitivity increases under higher co2 levels due to feedback temperature dependence. *Geophysical Research Letters*, 48, 2020. doi: 10.1029/2020GL089074.

F. Bryan. Parameter sensitivity of primitive-equation ocean general circulation models. *Journal of Physical Oceanography*, 17:970–985, 1987.

M. Budyko. The effect of solar radiation variations on the climate of the earth. *Tellus*, 21:611–619, 1969. doi: 10.3402/tellusa.v21i5.10109.

C. Cabanes, T. Lee, and L.-L. Fu. Mechanims of interannual variations of the meridional overturning circulation of the north atlantic ocean. *Journal of Physical Oceanography*, 38:467–480, 2008. doi: 10.1175/2007JPO3726.1.

K. Caldeira and N. P. Myhrvold. Projections of the pace of warming following an abrupt increase in atmospheric carbon dioxide concentration. *Environmental Research Letters*, 8, 2013. doi: 10.1088/1748-9326/8/3/034039.

L. Cao, L. Duan, G. Bala, and K. Calderia. Simulated long-term climate response to idealized solar geoengineering. *Geophysical Research Letters*, 43:2209–2217, 2016. doi: 10.1002/2016GL068079.

P. Cessi. The effect of northern hemisphere winds on the meridional overturning circulation and stratification. *Journal of Physical Oceanography*, 48:2495–2506, 2018. doi: 10.1175/JPO-D-18-0085.1.

J. G. Charney, Arakawa, D. J. Baker, B. Bolin, R. E. Dickinson, R. M. Goody, and C. I. Wunsch. Carbon dioxide and climate: A scientific assessment. *National Academy of Sciences*, 1979.

R. Colman and B. McAvaney. Climate feedbacks under a very broad range of forcing. *Geophysical Research Letters*, 36, 2009. doi: 10.1029/2008GL036268.

P. M. Cox, R. A. Betts, C. D. Jones, S. A. Spall, and I. J. Totterdell. Acceleration of global warming due to carbon-cycle feedbacks in a coupled climate model. *Nature*, 408:184–187, 2000. doi: 10.1038/35041539.

S. A. Cunningham et al. Temporal variability of the atlantic meridional overturning circulation at 26.5n. *Science*, 317:935–938, 2007. doi: 10.1126/science.1141304.

G. Danabasoglu and P. R. Gent. Equilibrium climate sensitivity: Is it accurate to use a slab ocean model? *Journal of Climate*, 22:2494–2499, 2009. doi: 10.1175/2008JCLI2596.1.

A. M. DeBoer, A. Gnanadesikan, N. L. Edwards, and A. J. Watson. Meridional density gradients do not control the atlantic overturning circulation. *Journal of Oceanography*, 40:368–380, 2010. doi: 10.1175/2009JPO4200.1.

R. E. Dickinson and K. J. Schaudt. Analysis of timescales of response of a simple climate model. *Journal of Climate*, 11:97–106, 1993. doi: 10.2307/26242911.

A. Farnsworth et al. Climate sensitivity on geological timescales controlled by nonlinear feedbacks and ocean circulation. *Geophysical Research Letters*, 46:9880–9889, 2019. doi: 10.1029/2019GL083574.

B. Fox-Kemper et al. Challenges and prospects in ocean circulation models. *Frontier of Marince Science*, 6:65, 2019. doi: 10.3389/fmars.2019.00065.

E. Frajka-Williams et al. Atlantic meridional overturning circulation: Observed transport and variability. *Frontiers in Marine Science*, 6, 2019. doi: 10.3389/fmars.2019.00260.

P. R. Gent, J. Willebrand, T. J. McDougall, and J. C. McWilliams. Parameterizing eddy-induced tracer transports in ocean circulation models. *Journal of Physical Oceanography*, 25:463–474, 1995. doi: 10.1175/1520-0485(1995)025⟨0463:PEITTI⟩2.0.CO;2.

P. R. Gent et al. The community climate system model version 4. *Journal of Climate*, 24:4973–4991, 2011. doi: 10.1175/2011JCLI4083.1.

O. Geoffroy, D. Saint-Martin, D. Olivie, A. Voldoire, G. Bellon, and S. Tyteca. Transient climate response in a two-layer energy-balance

model. Part I: Analytical solution and parameter calibration using CMIP5 AOGCM experiments. *Journal of Climate*, 26:1841–1856, 2013a. doi: 10.1175/JCLI-D-12-00195.1.

O. Geoffroy, D. Saint-Martin, D. Olivie, A. Voldoire, G. Bellon, and S. Tyteca. Transient climate response in a two-layer energy-balance model. Part 2: Representation of the efficacy of deep-ocean heat uptake and validation for cmip5 aogcms. *Journal of Climate*, 26:1859–1875, 2013b. doi: 10.1002/2013GL058118.

A. Gnanadesikan. A simple predictive model for the structure of the oceanic pycnocline. *Science*, 283:2077–2079, 1999. doi: 10.1126/science.283.5410.2077.

A. Gnanadesikan, A. M. DeBoer, and B. K. Mignone. A simple theory of the pycnocline and overturning revisited. *Ocean Circulation: Mechanisms and Impacts (Geophysical Monograph Series)*, 173, 2007. doi: 10.1029/173GM04.

P. Good, J. M. Gregory, J. A. Lowe, and T. Andrews. Abrupt co2 experiments as tools for predicting and understanding cmip5 representative concentration pathway projections. *Climate Dynamics*, 40:1042–1053, 2013. doi: 10.1007/s00382-012-1410-4.

J. M. Gregory, W. J. Ingram, M. A. Palmer, G. S. Jones, P. A. Stott, R. B. Thorpe, J. A. Lowe, T. C. Johns, and K. D. Williams. A new method for diagnosing radiative forcing and climate sensitivity. *Geophys Res Lett*, 31, 2004. doi: 10.1029/2003GL018747.

A. Griesel and M. A. M. Maqueda. The relation of meridional pressure gradients to north atlantic deep water volume transport in an ocean general circulation model. *Climate Dynamics*, 26:781–799, 2006. doi: 10.1007/s00382-006-0122-z.

O. Gutjahr, D. Putrasahan1, K. Lohmann, J. H. Jungclaus, J.-S. von Storch, N. Brüggemann, H. Haak, and A. Stössel. The max planck institute earth

system model (mpi-esm1.2) for the high-resolution model intercomparison project (highresmip). *Geoscientific Model Development*, 12:3241–3281, 2019. doi: 10.5194/gmd-12-3241-2019.

J. Hansen, G. Russel, A. Lacis, I. Fung, D. Rind, and P. Stone. Climate response-times: dependence on climate sensitivity and ocean mixing. *Science*, 229:857–859, 1985. doi: 10.1126/science.229.4716.857.

J. Hansen et al. Climate sensitivity: Analysis of feedback mechanisms. In J and T. Takahashi, editors, *Climate Processes and Climate Sensitivity.*, pages 130–163. AGU Geophysical Monograph 29, 1984.

K. Hasselmann et al. On the cold start problem in transient simulations with coupled atmosphere-ocean models. *Climate Dynamics*, 9:53–61, 1993. doi: 10.1007/BF00210008.

I. M. Held, M. Winton, K. Takahashi, T. Delworth, F. Zeng, and G. K. Vallis. Probing the fast and slow components of global warming by returning abruptly to preindustrial forcing. *Jurnal of Climate*, 23:2418–2427, 2010. doi: 10.1175/2009JCLI3466.1.

J. Hirschi and J. Marotzke. Reconstructing the meridionaloverturning circulation from boundary densities and the zonal wind stress. *Journal of Physical Oceanography*, 47:743–763, 2007. doi: 10.1175/JPO3019.1.

J. Hirschi, J. Baehr, J. Marotzke, J. Stark, S. Cunningham, and J. O. Beismann. A monitoring design for the atlantic meridional overturning circulation. *Geophysical Research Letters*, 30, 2003. doi: 10.1029/2002GL016776.

T. Ito and J. Marshall. Control of lower-limb overturning circulation in the southern ocean by diapycnal mixing and mesoscale eddy transfer. *Journal of Physical Oceanography*, 38:2832–2845, 2008. doi: 10.1175/2008JPO3878.1.

S. R. Jayne and J. Marotzke. The dynamics of ocean heat transport variability. *Reviews of Geophysics*, 39:385–411, 2001. doi: 10.1029/2000RG000084.

H. L. Johnson, D. P. Marshall, and D. A. J. Sproson. Reconciling theories of a mechanically driven meridional overturning circulation with thermohaline forcing and multiple equilibria. *Climate Dynamics*, 29:821–836, 2007. doi: 10.1007/s00382-007-0262-9.

H. L. Johnson, P. Cessi, D. P. Marshall, F. Schloesser, and M. A. Spall. Recent contributions of theory to our understanding of the atlantic meridional overturning circulation. *Journal of Geophysical Research*, 124:5376–539, 2019. doi: 10.1029/2019JC015330.

E. Kalnay et al. The ncep/ncar 40-year reanalysis project. *Bulletin of the American Meteorological Society*, 77:347–471, 2018. doi: 10.1175/1520-0477(1996)077⟨0437:TNYRP⟩2.0.CO;2.

B. A. Klinger and C. Cruz. Decadal response of global circulation to southern ocean zonal wind stress perturbation. *Journal of Physical Oceanography*, 39:1888–1904, 2009. doi: 10.1175/2009JPO4070.1.

B. A. Klinger, S. Drijfhout, J. Marotzke, and J. R. Scott. Sensitivity of basinwide meridional overturning to diapycnal diffusion and remote wind forcing in an idealized atlantic–southern ocean geometry. *Journal of Physical Oceanography*, 33:249–266, 2003. doi: 10.1175/1520-0485(2003)033⟨0249:SOBMOT⟩2.0.CO;2.

B. A. Klinger, S. Drijfhout, J. Marotzke, and J. R. Scott. Remote wind-driven overturning in the absence of the drake passage effect. *Journal of Physical Oceanography*, 34:1036–1049, 2004. doi: 10.1175/1520-0485(2004)034⟨1036:RWOITA⟩2.0.CO;2.

R. Knutti and M. Rugenstein. Feedbacks, climate sensitivity and the limits of linear models. *Philosophical Transactions*, 373, 2015. doi: 10.1098/rsta.2015.0146.

T. Kuhlbrodt, A. Griesel, M. Montoy, A. Levermann, Hofmann, and S. Rahmstorf. On the driving processes of the atlantic meridional overturning circulation. *Reviews of Geophysics*, 45, 2007. doi: 10.1029/2004RG000166.

J. E. Kutzbach, F. He, S. J. Vavrus, and W. F. Ruddiman. The dependence of equilibrium climate sensitivity on climate state: Applications to studies of climates colder than present. *Geophysical Research Letters*, 40:3721–3726, 2013. doi: 10.1002/grl.50724.

S. J. Levang and R. W. Schmitt. What causes the amoc to weaken in cmip5? *Journal of Climate*, 33:1535–1545, 2019. doi: 10.1175/JCLI-D-19-0547.1.

A. Levermann and J. J. Fuerst. Atlantic pycnocline theory scrutinized using a coupled climate model. *Geophysical Research Letters*, 37, 2010. doi: 10.1029/2010GL044180.

J. R. Luyten, J. Pedlosky, and H. Stommel. The ventilated thermocline. *Journal of Physical Oceanography*, 13:292–309, 1983. doi: 10.1175/1520-0485(1983)013⟨0292:TVT⟩2.0.CO;2.

V. Lüschow, J.-S. von Storch, and J. Marotzke. Overturning response to a doubling of the surface wind stress in an eddying and a non-eddying ocean. *Journal of Physical Oceanography*, 51:1007–1020, 2021. doi: 10.1175/JPO-D-20-0176.1.

J. Marotzke. Boundary mixing and the dynamics of three-dimensional thermohaline circulations. *Journal of Physical Oceanography*, 27:1713–1728, 1997. doi: 10.1175/1520-0485(1997)027⟨1713:BMATDO⟩2.0.CO;2.

J. Marotzke and B. A. Klinger. The dynamics of equatorially asymmetric thermohaline circulations. *Journal of Physical Oceanography*, 30:955–968, 2000. doi: 10.1175/1520-0485(2000)030⟨0955:TDOEAT⟩2.0.CO;2.

D. P. Marshall and H. L. Johnson. Relative strength of the antarctic circumpolar current and atlantic meridional overturning circulation. *Tellus A: Dynamic Meteorology and Oceanography*, 69, 2017. doi: 10.1080/16000870.2017.1338884.

D. P. Marshall and L. Zaana. A conceptual model of ocean heat uptake under climate change. *Journal of Climate*, 27:8444–8465, 2014. doi: 10.1175/JCLI-D-13-00344.1.

J. Marshall and K. Speer. Closure of the meridional overturning circulation through southern ocean upwelling. *Nature Geoscience*, 5:171–180, 2012. doi: 10.1038/ngeo1391.

T. Mauritsen et al. Developments in the MPI-M Earth System Model version 1.2 (MPI-ESM1.2) and its response to increasing CO_2. *manuscript submitted, JAMES*, 2018.

J. P. McCreary and P. Lu. Interaction between the subtropical and equatorial ocean circulations: The subtropical cell. *Journal of Physical Oceanography*, 24:466–497, 1994. doi: 10.1175/1520-0485(1994)024⟨0466:IBTSAE⟩2.0.CO;2.

K. Meraner, T. Mauritsen, and A. Voigt. Robust increase in equilibrium climate sensitivity under global warming. *Geophysical Research Letters*, 40:5944–5948, 2013. doi: 10.1002/2013GL058118.

E. Moreno-Chamarro, P. Ortega, F. Gonzalez-Rouco, and M. Montoya. Assessing reconstruction techniques of the atlantic ocean circulation variability during the last millennium. *Climate dynamics*, 2016. doi: 10.1007/s00382-016-3111-x.

W. Munk and C. Wunsch. Abyssal recipes ii: energetics of tidal and wind mixing. *Deep Sea Research Part I: Oceanogrpahic Research Papers*, 45: 1977–2010, 1998. doi: 10.1016/S0967-0637(98)00070-3.

M. Nikurashin and G. Vallis. A theory of interhemispheric meridional overturning circulation as associated stratification. *Journal of Physical Oceanography*, 42:1652–1667, 2012.

D. J. L. Olivie, G. P. Peters, and D. Saint-Martin. Atmosphere response time scales estimated from aogcm experiments. *Journal of Climate*, 25: 7956–7972, 2012. doi: 10.1175/JCLI-D-11-00475.1.

B. C. O'Neill, , C. Tebaldi, D. P. vanVuuren, V. Eyring, P. Friedlingstein, G. Hurtt, R. Knutti, E. Kriegler, J.-F. Lamarque, J. Lowe, G. A. Meehl,

R. Moss, K. Riahi, and B. M. Sanderson. The scenario model intercomparison project (scenariomip) for cmip6. *Geoscientific Model Development*, 9: 3461–3482, 2016. doi: 10.5194/gmd-9-3461-2016.

W. Parker. Climate science. *The Stanford Encyclopedia of Philosophy*, 2018.

C. Proistosescu and P. J. Huybers. Slow climate mode reconciles historical and model-based estimates of climate sensitivity. *Science Advances*, 3, 2017. doi: 10.1126/sciadv.1602821.

D. A. Putrasahan, J. S. von Storch, O. Gutjahr, H. Haakk, K. Lohmann, M. Roberts, and J. Jungclaus. Effect of resolving ocean eddies on the transient response of global mean surface temperature to abrupt 4xco2 forcing. *Geophysical Research Letters, submitted*, 2020.

S. C. B. Raper, J. M. Gregory, and R. J. Stouffer. The role of climate sensitivity and ocean heat uptake on aogcm transient temperature response. *Journal of Climate*, 15:124–130, 2002.

M. H. Redi. Oceanic isopycnal mixing by coordinate rotation. *Journal of Physical Oceanography*, 12:1154–1158, 1982. doi: 10.3389/fmars.2019.00065.

A. Robinson and H. Stommel. The oceanic thermocline and the associated thermohaline circulation. *Tellus*, 1959. doi: 10.1111/j.2153-3490.1959.tb00035.x.

G. H. Roe and K. C. Armour. How sensitive is climate sensitivity? *Geophysical Research Letters*, 38, 2011. doi: 10.1029/2011GL047913.

G. H. Roe and M. B. Baker. Why is climate sensitivity so unpredictable. *Science*, 318:629–632, 2007. doi: 10.1126/science.1144735.

T. Rohrschneider, B. Stevens, and T. Mauritsen. On simple representations of the climate response to external radiative forcing. *Climate Dynamics*, 53:3131–3145, 2019. doi: 10.1007/s00382-019-04686-4.

M. A. A. Rugenstein, K. Caldeira, , and R. Knutti. Dependence of global radiative feedbacks on evolving patterns of surface heat fluxes. *Geophysical Research Letters*, 43, 2016a. doi: 10.1002/2016GL070907.

M. A. A. Rugenstein, J. Sedlacek, and R. Knutti. Nonlinearities in patterns of long-term ocean warming. *Geohysical Research Letters*, 43:3380–3388, 2016b. doi: 10.1002/2016GL068041.

M. A. A. Rugenstein et al. Longrunmip: Motivation and design for a large collection of millennial-length aogcm simulations. *Bulletin of the American Meteorological Society*, 2019. doi: 10.1175/BAMS-D-19-0068.1.

G. Schaffer, M. Huber, R. Rondanelli, and J. O. P. Pedersen. Deep time evidence for climate sensitivity increase with warming. *Geophysical Research Letters*, 43:6538–6545, 2016. doi: 10.1002/2016GL069243.

J. R. Scott. The roles of mixing, geothermal heating, and surface buoyancy forcing in ocean meridional overturning dynamics. *PhD thesis, Massachusetts Institute of Technology*, 2000.

C. A. Senior and J. F. B. Mitchell. The time-dependence of climate sensitivity. *Geophys Res Lett*, 27(17):2685–2688, 2000. doi: 10.1029/2000GL011373.

C. J. Shakespeare and A. M. Hogg. An analytical model of the response of the meridional overturning circulation to changes in wind and buoyancy forcing. *Journal of Physical Oceanography*, 42:1270–1287, 2012. doi: 10.1175/JPO-D-11-0198.1.

B. J. Soden and I. M. Held. An assessment of climate feedbacks in coupled ocean-atmosphere models. *Journal of Climate*, 19:3354–3360, 2006. doi: 10.1175/JCLI3799.1.

B. Stevens, S. C. Sherwood, S. Bony, and M. J. Webb. Prospects for narrowing earth's equilibrium climate sensitivity. *Earths future*, 4:512–522, 2016. doi: 10.1002/2016EF000376.

J. R. Toggweiler and B. Samuels. Effect of drake passage on the global thermohaline circulation. *Deep Sea Research Part I: Oceanogrpahic Research Papers*, 42:477–500, 1995. doi: 10.1016/0967-0637(95)00012-U.

K. Treneberth. *Climate System Modelling*. C¿ambridge University Press, 1992.

H. Tsujino and N. Suginohara. Thermohaline circulation enhanced by wind forcing. *Journal of Physical Oceanography*, 29:1506–1516, 1998. doi: 10.1175/1520-0485(2003)033⟨0249:SOBMOT⟩2.0.CO;2.

G. K. Vallis. Large-scale circulation and production of stratification: Effects of wind, geometry, and diffusion. *Journal of Physical Oceanography*, 30:933–953, 2000. doi: 10.1175/1520-0485(1997)027⟨1713:BMATDO⟩2.0.CO;2.

J.-S. von Storch, C. Eden, I. Fast, H. Haak, D. Deckers, E. Maier-Reimer, J. Marotzke, and D. Stammer. An estimate of the lorenz energy cycle for the world ocean based on the 1/10 storm/ncep simulation. *Journal of Physical Oceanography*, 42:2185–2205, 2012. doi: 10.1175/JPO-D-12-079.1.

P. Welander. An advective model of the ocean thermocline. *Tellus*, 1959. doi: 10.1111/j.2153-3490.1959.tb00036.x.

T. M. L. Wigley and M. E. Schlesinger. Analytical solution for the effect of increasing co2 on global mean temperature. *Nature*, 315:649–652, 1985. doi: 10.1038/315649a0.

R. G. Williams and V. Roussenov. Decadal evolution of ocean thermal anomalies in the north atlantic: The effects of ekman, overturning, and horizontal transport. *Journal of Climate*, 27:698–719, 2014. doi: 10.1175/JCLI-D-12-00234.1.

M. Winton, K. Takahashi, and I. M. Held. Importance of ocean heat uptake efficacy to transient climate change. *Journal of Climate*, 23:2333–2344, 2010. doi: 10.1175/2009JCLI3139.1.

E. T. Wolf, J. HaqqMisrea, and O. B. Toon. Evaluating climate sensitivity to co2 across earth's history. *Journal of Geophyscial Research: Atmospheres*, 123, 2018. doi: 10.1029/2018JD029262.

C. L. Wolfe and P. Cessi. The adiabatic pole-to-pole overturning circulation. *Journal of Physical Oceanography*, 41:1705–1810, 2011. doi: 10.1175/2011JPO4570.1.

S. G. Yaeger, C. A. Shields, W. G. Large, and J. J. Hack. The low-resolution ccsm3. *Journal of Climate*, 19:2545–2566, 2006. doi: 10.1175/JCLI3744.1.

I. Zaliapin and M. Ghil. Another look at climate sensitivity. *Nonlinear Processes in Geophysics*, 17:113–122, 2010. doi: 10.5194/npg-17-113-2010.

Eidesstattliche Versicherung / *Declaration on oath*

Hiermit erkläre ich an Eides Statt, dass ich die vorliegende Dissertationsschrift selbst verfasst und keine anderen als die angegebenen Quellen und Hilfsmittel benutzt habe.

I hereby declare, on oath, that I have written the present dissertation by my own and have not used other than the acknowledged resources and aids.

Hamburg _____ Unterschrift / Signature _____

(Datum / Date)

Hinweis / Reference

Die gesamten Veröffentlichungen in der Publikationsreihe des MPI-M
„Berichte zur Erdsystemforschung / Reports on Earth System Science“,
ISSN 1614-1199

sind über die Internetseiten des Max-Planck-Instituts für Meteorologie erhältlich:
http://www.mpimet.mpg.de/wissenschaft/publikationen.html

All the publications in the series of the MPI -M
„Berichte zur Erdsystemforschung / Reports on Earth System Science“,
ISSN 1614-1199

are available on the website of the Max Planck Institute for Meteorology:
http://www.mpimet.mpg.de/wissenschaft/publikationen.html